

Aus dem Institut für Pathophysiologie
der Universitätsmedizin der Johannes Gutenberg-Universität Mainz

Optimizing functional calcium imaging analysis enables the discovery of cortical microcircuit dysfunction in mice exposed to anti-NMDA receptor antibodies

Optimierung der funktionellen Kalziumbildgebungsanalyse ermöglicht die Entdeckung von Dysfunktionen kortikaler Netzwerkprozesse in Mäuse nach Exposition gegenüber NMDA-Antikörpern

Inauguraldissertation
zur Erlangung des Doktorgrades der
Medizin
der Universitätsmedizin
der Johannes Gutenberg-Universität Mainz

Vorgelegt von

Saleh Altahini
aus Der Alzour, Syrien

Mainz, 2023

Tag der Promotion:

07. Feb 2021

*“Science isn't about why. It's about why not.”
- Cave Johnson*

Table of Contents

List of Abbreviations	I
List of Figures	III
1. Motivation	1
2. Zusammenfassung	2
3. Introduction	5
3.1. The intricate interplay between the immune system and the brain	5
3.1.1. Blood-brain barrier.....	5
3.1.2. The role of immune cells in the brain	6
3.1.3. Antibodies in the adult and fetal brain	7
3.2. Autoimmune encephalitis	7
3.2.1. Classical paraneoplastic AE	8
3.2.2. Facultative paraneoplastic AE.....	8
3.3. Anti-NMDA receptor encephalitis	8
3.3.1. Epidemiology	8
3.3.2. Pathophysiology	9
3.3.3. Symptoms.....	9
3.3.4. Diagnostics	10
3.3.5. Therapy	11
3.3.6. Prognosis.....	11
3.4. NMDA Receptors	11
3.5. Basics of functional calcium imaging	13
3.5.1. Calcium ions in neurons	13
3.5.2. Calcium indicators	14
3.5.3. Two-photon microscopy	14
3.6. Analysis of functional calcium imaging data	16
3.6.1. Motion Correction	16
3.6.2. Segmentation	17
3.6.3. Trace Extraction	18
3.6.4. Further analysis	18
4. Material and Methods	21
4.1. Animals and disease model	21
4.2. Virus injection and surgery	21
4.3. Two-photon calcium imaging	22
4.4. Visual stimulation	23
4.5. Two-photon data analysis	23
4.6. Analysis of visually evoked activity	26
4.7. Statistical tests	26
4.8. Benchmarking the analysis pipeline	27
4.9. Software development	27
5. Results	29
5.1. Improvements in data analysis and new software developments	29
5.1.1. Data analysis pipeline and quality control measures	30

5.1.2. StaAv Tool: a new plugin for improved intensity projections.....	30
5.1.3. Faster, integrated, and multithreaded analysis in Python for ViNe-Seg	34
5.1.4. Mask RCNN can detect both cells and vessels in single frames of functional calcium recordings.....	37
5.2. Examining microcircuit changes in Anti-NMDA receptor encephalitis	41
5.2.1. Awake two-photon calcium imaging of excitatory microcircuits in layers II/III of mouse primary visual cortex.....	41
5.2.2. NMDAR antibody exposure leads to a decrease in spontaneous firing rates and to a bursty firing profile of V1 neurons.....	41
5.2.3. Local microcircuit connectivity remains unchanged after antibody exposure.	43
5.2.4. V1 excitatory neurons of NMDAR-Ab exposed animals exhibit a higher orientation tuning and a narrowing of their receptive fields.	44
5.2.5. Microcircuits of NMDAR-Ab exposed mice maintain a bias towards cardinal orientations.	45
5.2.6. Local cortical networks in NMDAR-Ab exposed animals are characterized by a dissociation between spontaneous and visually evoked activity.....	49
6. Discussion	50
6.1. functional state changes caused by NMDAR-Ab exposure.....	50
6.1.1. Distinct functional microarchitecture characterized by low-active, bursty neurons.....	51
6.1.2. Altered yet efficient encoding of visual representations	51
6.1.3. Early, in utero, exposure leads to a long-term (mal)adaptive network state	52
6.1.4. Subtle long-term effects of <i>in utero</i> antibody exposure, a representation of a network one hit away from total breakdown?.....	52
6.1.5. Dissociation of the neuronal representation of ongoing – spontaneous – and visually evoked activity – a generalizable mechanism underlying psychosis?	53
6.2. Improved data analysis pipeline	53
6.2.1. Powerful calcium analysis pipeline to detect subtle network changes.....	53
6.2.2. Fast and accurate machine learning assisted analysis.....	54
6.2.3. Towards real-time closed-loop experiments	55
7. Summary and Conclusion	56
8. References.....	58
9. Acknowledgments.....	68
10. Publications.....	69
11. Curriculum vitae.....	70

List of Abbreviations

Abbreviation	Meaning
°C	Celsius
2D	Two-Dimensional
AE	Autoimmune Encephalitis
AMPA	α -amino-3-hydroxy-5-methyl-4-isoxazolepropionic acid
API	Application Programming Interface
ASD	Autism Spectrum Disorders
BBB	Blood-Brain-Barrier
BCFB	Blood-Cerebral-Fluid-Barrier
BOLD	Blood-Oxygen-Level-Dependent
Ca ²⁺	Calcium
CaM	Calmodulin
cm	Centimeter
CNS	Central Nervous System
cpGFP	Circularly Permuted Green Fluorescent Protein
CSF	Cerebral Spinal Fluid
CV	Circular Variance
DDR3	Double Data Rate 3
DSI	Direction Selectivity Index
E/I-balance	Excitatory / Inhibitory Balance
EEG	Electroencephalogram
ER	Endoplasmic Reticulum
fMRI	Functional Magnetic Resonance Imaging
FOV	Field of View
GABA	Gamma-Aminobutyric Acid
GB	Gigabyte
GECI	Genetically Encoded Calcium Indicators
GFP	Green Fluorescent Protein
GHz	Gigahertz
Glu	Glutamate
GUI	Graphical User Interface
H ⁺	Hydrogen Ion
HDD	Hard Disk Drive
Hz	Hertz
I/O	Input/Output
ICU	Intensive Care Unit
IEI	Inter-Event Interval
IFN	Interferon
IgG	Immunoglobulin G
iGluR	Ionotropic Glutamate Receptors
IgM	Immunoglobulin M
K ⁺	Potassium
LTP	Long-Term Potentiation
Mg ²⁺	Magnesium
mm	Millimeter
MRI	Magnetic Resonance Imaging

Na ⁺	Sodium
nAChR	Nicotinic Acetylcholine Receptors
NCX	Na ⁺ /Ca ²⁺ Exchanger
NEOS	Anti-NMDAR Encephalitis One-Year Functional Status
nL	Nanoliter
nM	Nanomolar
nm	Nanometer
NMDAR	N-Methyl-D-Aspartate Receptors
NMDAR-Ab	Anti-NMDA Antibodies
NMDARE	Anti-NMDA Receptor Encephalitis
NVMe	Non-Volatile Memory Express
OE	Oblique Effect
OGB-1	Oregon Green Bapta-1
OSI	Orientation Selectivity Index
PET	Positron Emission Tomography
PMCA	Plasma-Membrane Ca ²⁺ -Atpase
PMT	Photomultiplier Tube
RAM	Random Access Memory
RCNN	Region-Based Convolutional Neural Network
RGB	Red, Green, and Blue
ROI	Region Of Interest
s	Seconds
SATA	Serial Advanced Technology Attachment
SD	Standard Deviation
SEM	Standard Error of The Mean
SERCA	Sarcoendoplasmic Reticulum Ca ²⁺ -Atpase
SNR	Signal-To-Noise Ratio
SSD	Solid State Drive
TB	Terabyte
TFT	Thin-Film Transistor
Ti:Sa	Titanium-Sapphire
TRP	Transient Receptor Potential
TTL	Transistor–Transistor Logic
USB	Universal Serial Bus
UV	Ultraviolet
V1	Primary Visual Cortex
VGCC	Voltage Gated Ca ²⁺ Channels
WT	Wildtype
μg	Microgram
μL	Microliter
μm	Micrometer (Micron)

List of Figures

Figure 1: Clinical presentation of NMDARE at various stages.....	9
Figure 2: NMDA receptors' gating and their role in long-term potentiation.....	12
Figure 3: Changes in GCaMP indicator conformation and comparison of microscopy techniques.	15
Figure 4: Loss of information in calcium recordings due to motion artefacts.	16
Figure 5: Manual segmentation of cell bodies into regions of interest.	18
Figure 6: Simultaneous calcium imaging with GCaMP6f and electrophysiology.	19
Figure 7: Micro-surgery with craniectomy and head holder implantation.	22
Figure 8: Overview of the imaging setup.	23
Figure 9: An exemplary average intensity projection.	24
Figure 10: An exemplary manual segmentation of neuronal somata.	24
Figure 11: $\Delta f/f$ fluorescence traces extracted from calcium imaging.....	25
Figure 12: Schematic illustration of the analysis pipeline for this study.	26
Figure 13: Proposed quality control steps for an efficient calcium imaging analysis pipeline.....	29
Figure 14: StaAv Tool for enhancing cells' visibility in average intensity projections.....	31
Figure 15: Settings dialog box of StaAv Tool.	32
Figure 16: Multithreading can reduce trace extraction time.....	35
Figure 17: Model Manager in ViNe-Seg for intuitive overview and management of available segmentation models.....	37
Figure 18: Mask RCNN can detect both neurons and vessels in low SNR single frames.	38
Figure 19: Timelapse mode UI for inspecting multiple aspects of the analysis at once.....	39
Figure 20: Live mode UI gives an indication of the quality of the recording in real-time.	40
Figure 21: Study design and methodological approach.....	42
Figure 22: Reduced Spontaneous activity and bursty firing profile in NMDAR-Ab animals.	43
Figure 23: No significant changes in local functional connectivity due to NMDAR-Ab exposure.....	44
Figure 24: Higher orientation tuning in NMDAR-Ab animals.....	46
Figure 25: Constriction of V1 neurons receptive fields after NMDAR-Ab exposure.	47
Figure 26: Preserved bias towards cardinal orientations after NMDARE-Ab exposure.	48
Figure 27: Dissociation of neuronal population recruited by spontaneous activity and visual stimulation in NMDAR-Ab exposed animals.	49
Figure 28: Exposure to anti-NMDAR antibodies leads to functional defects of cortical microcircuits.....	50
Figure 29: Semantic vs instance segmentation.	55

1. Motivation

Anti-NMDA receptor encephalitis (NMDARE) is an autoimmune brain inflammation caused by IgG antibodies that specifically bind to the N-methyl-D-aspartate receptors (NMDAR) (Dalmau et al., 2019). While NMDARE is considered as a rare disease, it's worth noting that human anti-NMDAR antibodies (NMDAR-Ab) were detected in up to 1% of healthy individuals (Dahm et al., 2014, Lang and Pruss, 2017). This prevalence raises a potential concern: a considerable subgroup of pregnant women could be carrying NMDA-Ab and then transfer them to the fetus during pregnancy. NMDARs play a key role in long-term potentiation (LTP) and thus in modulating synaptic plasticity and in controlling memory functions (Luscher and Malenka, 2012, Li and Tsien, 2009). In humans, alterations in NMDAR have been linked to dementia and neurodegeneration (Wang and Reddy, 2017, Choi et al., 1988, Zhou et al., 2013) as well as psychotic experiences (Sterzer et al., 2018, Coyle, 2012). It has been well established that antibodies against NMDAR cause an internalization of the receptor and a disruption of their signaling (Masdeu et al., 2016, Kreye et al., 2016). Until today, the effect of the antibodies has been examined in cell culture and behavioral animal experiments. To our knowledge, no *in-vivo* electrophysiology or functional recordings have been conducted. The effect of the NMDAR-Ab on neural networks and cell communication in the brain is still unclear.

Here, we ask whether NMDAR-Ab exposure due to maternofetal transfer leads to a persistent change in functional cortical networks. We used the murine model of in utero exposure to human recombinant anti-NMDAR antibodies (Jurek et al., 2019). We employed two-photon calcium imaging in the awake mouse in adulthood (P51), corresponding to early adulthood in humans. Specifically, we chose the primary visual cortex, as this permitted the recording of both spontaneous, task-free activity, which might represent the functional microarchitecture of a given network, as well as sensory evoked activity, indicating the precision of sensory processing.

Although the field of calcium imaging and two-photon microscopy has existed since the 1990s, the analysis methods are still unstandardized, and datasets are frequently under-analyzed. Particularly, functional calcium imaging is a very powerful method that allows the capture of local circuit dynamics of hundreds of neurons simultaneously, yet with single-cell resolution. Therefore, it might be sensitive to capture also subtle network state changes (Arnoux et al., 2018, Ellwardt et al., 2018, Rosales Jubal et al., 2021). To extract the most information out of calcium imaging datasets, a powerful and detailed analysis routine is paramount. While performing this study, we also focused our attention on currently available and popular calcium imaging analysis tools.

Within the scope of this work, we also introduce new tools for calcium imaging analysis and quality control, allowing better and faster results and enabling the detection of subtle network changes. We also introduce near real-time analysis methods, paving the road towards closed loop interventions.

2. Zusammenfassung

In dieser Arbeit haben wir die Langzeitauswirkungen von anti-NMDA-Rezeptor-Antikörpern (NMDAR-Ab) auf die neuronalen Aktivitätsmuster untersucht. Diese IgG-Antikörper binden an die N-Methyl-D-Aspartat Rezeptoren (NMDAR) und stören deren Funktion. Wenn sie im Liquor lokalisiert sind, können sie bei jungen Erwachsenen eine Entzündung des Hirngewebes verursachen und schwere neuropsychiatrische Symptome auslösen. NMDAR-Ab wurden bei bis zu 1 % von gesunden Personen nachgewiesen. Da sie die Blut-Plazentaschranke passieren können, ist ein bislang noch nicht erfasstes Risiko für den Fetus anzunehmen. Um die Auswirkungen der Antikörper zu untersuchen, haben wir ein Mausmodell mit maternofetal übertragenen humanen NMDAR-Ab verwendet. 51 Tage nach Geburt, was beim Menschen dem frühen Erwachsenenalter entspricht, haben wir *in-vivo* Zwei-Photonen Kalziumbildgebung bei wachen Mäusen durchgeführt. Um die geringsten Veränderungen in der Netzwerkdynamik mit Hilfe der Kalziumbildgebung erkennen zu können, mussten wir zuerst eine leistungsfähige und fein abgestimmte Analyse-Pipeline entwickeln.

Zunächst haben wir uns die derzeit verwendeten Analyseroutinen angesehen. Unter den möglichen Analysemethoden haben wir uns für einen halbautomatischen Ansatz entschieden, der für gute Präzision bekannt ist. Um zu verhindern, dass potenzielles Rauschen die Ergebnisse beeinträchtigt, haben wir unsere Analyse auf die Binarisierung von Kalziumtransienten gestützt. Zur Gewährleistung der Genauigkeit haben wir jeden Aspekt der Analysepipeline genau überprüft und Qualitätskontrollpunkte eingerichtet. Selbst kleinste Unzulänglichkeiten in der Analyseroutine können erhebliche Auswirkungen auf die Integrität der Ergebnisse haben. Zudem haben wir drei neue Tools für die Analyse von Kalziumbildungsdaten eingeführt. Zunächst haben wir StaAv Tool entwickelt, ein java-basiertes ImageJ-Plugin zur Verbesserung der Sichtbarkeit von Zellen in Intensitätsprojektionen. Dieses Plugin und sein Quellcode sind auf unserem GitHub öffentlich zugänglich. Zweitens haben wir zu der Entwicklung der Deep-Learning-gestützten Segmentierungssoftware ViNe-Seg beigetragen. ViNe-Seg ist ebenfalls öffentlich auf GitHub verfügbar. Letztens haben wir Mask RCNN verwendet, um eine Echtzeit-, Frame-by-Frame-Analyse zu testen. Um die Nutzung dieser Software zu vereinfachen, haben wir eine intuitive Benutzeroberfläche entwickelt, die darauf ausgelegt ist, die Benutzerfreundlichkeit zu verbessern. Unsere Implementierung des Modells erwies sich als sehr leistungsfähig und war in der Lage, sowohl Gefäße als auch Neuronen selbst in Einzelbildern mit niedrigem Signal zu erkennen.

Um auf den neurophysiologischen Aspekt dieser Arbeit zurückzukommen, hat unsere Analyse gezeigt, dass die vorübergehende *in utero* Exposition zu NMDAR-Ab auch mehr als 7 Wochen nach der Geburt noch einen erheblichen Einfluss auf das Netzwerk haben kann. Bei den exponierten Tieren sind die untersuchten kortikalen Netzwerke durch mehrere subtile Defizite und Abweichungen vom normalen, gesunden Netzwerk gekennzeichnet. Diese Veränderungen können in drei Hauptpunkte eingeteilt werden:

- I. **Die homogenen Auswirkungen von NMDAR-Ab auf spontane Aktivität.** Die exponierten Netzwerke zeigten eine reduzierte Spontanaktivität und ein „bursty“ Aktivitätsmuster. Die Auswirkungen der Antikörper sind jedoch eher homogen und betreffen alle erregenden Neuronen gleichermaßen. Dies steht im Gegensatz zu vielen anderen neurologischen Erkrankungen, wie

z.B. der Alzheimer-Krankheit oder der Multiplen Sklerose, bei denen nur eine Teilpopulation der Neuronen Unterschiede aufweist. Die Homogenität der Auswirkungen erklärt auch, warum die funktionelle Konnektivität der exponierten Netzwerke scheinbar unverändert ist. Konnektivitätsanalysen, wie diese, die in dieser Studie verwendet wurde, hängen von den relativen Maßen der Aktivitätskorrelation ab. Wenn die Auswirkung im gesamten Netzwerk gleichmäßig ist, sind Veränderungen in der funktionellen Konnektivität möglicherweise nicht nachweisbar.

- II. **Veränderte Verarbeitung von visuellen Afferenzen.** Die Exposition zu NMDAR-Ab führte nicht nur zu einer höheren Orientierungsselektivität der einzelnen Neuronen, sondern beeinflusste auch, wie das Netzwerk visuelle Afferenzen codiert. Da das visuelle Stimulationsschema in dieser Studie 11 zufällige Versuche umfasste, ermöglichte die Durchschnittsbildung der hervorgerufenen Aktivitätsmuster die Beurteilung der Ähnlichkeit der Reaktionen auf verschiedene Stimuli. Dies zeigte eine Reduktion der rezeptiven Felder der Neuronen, wobei ein signifikanter Prozentsatz des Netzwerks nur auf eine einzige Orientierung reagierte. Daher wiesen die exponierten Netzwerke im Gegensatz zum gesunden eine reduzierte Ähnlichkeit in den hervorgerufenen Aktivitätsmustern auf. Dennoch konnten diese Veränderungen in der visuellen Verarbeitung immer noch eine effiziente Codierung widerspiegeln. Die exponierten Netzwerke zeigten immer noch eine Neigung zu kardinalen Orientierungen. Dies ist ein Effekt, von dem angenommen wird, dass er den visuellen Netzwerken hilft, eine effiziente Kodierung der visuellen Afferenzen aufrechtzuerhalten.
- III. **Dissoziation von neuronalen Populationen.** Die spontane Aktivität kortikaler Netzwerke wird als sehr wichtig angesehen, da sie sowohl eine Wiederholung früherer Erlebnisse als auch eine Antizipation oder Vorhersage neuer Eingaben umfasst. In gesunden Netzwerken sind die meisten Zellen sowohl an spontanen Aktivitätsmustern als auch an der Verarbeitung visueller Afferenzen beteiligt. In NMDAR-Ab-exponierten Netzwerken trennen sich diese beiden Populationen dagegen. Die spontan aktiven Zellen tragen zu keiner visuellen Verarbeitung bei, und diejenigen, die dies tun, sind nicht spontan aktiv. Diese Trennung kann dazu führen, dass das Netzwerk bekannte Erfahrungen als neu und aufmerksamkeitsbedürftig markiert, was sehr überwältigend sein kann.

Einige dieser Ergebnisse deuten auf eine zugrundeliegende Verschiebung des E/I-Gleichgewichts in Richtung erhöhter Hemmung hin. Da die inhibitorischen Teile des Netzwerks auch eine wichtige Rolle bei der Modulation des Aktivitätsprofils der exzitatorischen Zellen und ihrer Orientierungseinstellung spielen, sollten zukünftige Studien die gleichzeitige Kalziumbildung sowohl der inhibitorischen als auch der exzitatorischen Zellen umfassen. Unsere Daten zeigen, dass die Effekte der Antikörper-Exposition offenbar auch bei erwachsenen Tieren noch nachweisbar sind. Dennoch zeigen vergleichbare Studien, dass sich Verhaltensveränderungen im Erwachsenenalter auflösen könnten. Dies deutet darauf hin, dass die Exposition im Mutterleib möglicherweise als erster Schlag wirkt, der zu einem anfälligen Netzwerk führt, das leicht in einen totalen Zusammenbruch gedrängt werden kann. Daher könnte es sinnvoll sein, Verhaltenstests und mögliche zweite Umwelteinflüsse in zukünftige Studien einzubeziehen. Am wichtigsten ist es jedoch, dass die Dissoziation von spontaner und visuell evozierter Aktivität in der prädiktiven Kodierungstheorie, einem wichtigen theoretischen Rahmen der Psychose, eine Rolle spielt. Die

Erforschung dieses Effekts der Antikörperexposition kann dazu beitragen, unser Wissen über die Entstehung psychotischer Symptome nicht nur bei durch NMDAR-Ab verursachten Störungen wie NMDARE zu verbessern, sondern auch bei vielen anderen Erkrankungen.

Zusammenfassend stellt diese Arbeit einen wesentlichen ersten Schritt dar, um die Auswirkungen der NMDAR-Ab-Exposition zu verstehen. Die Fokussierung auf den zugrundeliegenden Übergang zu maladapten Netzwerkzuständen und Veränderungen in der Verarbeitung sensorischer Reize kann zur Entwicklung einer netzwerkbasierter Theorie neuropsychiatrischer Störungen beitragen. Dies könnte schließlich zu besseren und effektiveren Behandlungen und netzwerkbasierter Interventionen führen.

3. Introduction

3.1. The intricate interplay between the immune system and the brain

Both the central nervous system (CNS) and the immune system are very complex systems that can have an influence on each other. For instance, the CNS can directly influence the selectivity of T-regulatory cells via catecholamines such as dopamine (Kipnis et al., 2004). One very relatable example illustrating the profound impact of the immune system on the CNS is the phenomenon of sickness behavior (Filiano et al., 2015). During acute infections, the cytokines secreted by immune cells interact with the brain and modify behavior, promoting adaptive responses that might help in combating the infection (Dantzer et al., 2008). These responses may encompass reduced water and food consumption, decreased physical activity, and a diminished inclination towards social interaction. Despite years of research, the full extent of the interactions between the brain and the immune system is still not fully known.

Historically, the brain was regarded as an immune-privileged organ, shielded from the systemic immune response by the blood-brain barrier (BBB) (Carson et al., 2006, Muldoon et al., 2013, Erickson and Banks, 2018). In recent years, a myriad of new studies points to the fact that the influence of the immune system on brain functions and cognition is greatly understated. A nation-wide study of 3.56 million individuals in Denmark showed that a prior hospitalization for an autoimmune disorder or an infection increased the risk for subsequent mood disorder diagnosis by 45% and 62% respectively (Benros et al., 2013). For some neurological disorders with a relatively high prevalence such as major depressive disorder and schizophrenia, among others, there is a flood of epidemiological and clinical studies linking them to an activation of the immune system (Carvalho et al., 2013, Muller, 2018, Cullen et al., 2019, Konsman, 2019, Miller et al., 2021). Some patients diagnosed with schizophrenia were found to test positive for anti-NMDAR antibodies, at least during the first episode (Dalmau et al., 2019, Teixeira et al., 2017). Some studies show strong benefit of immunomodulation therapies and a lack of efficacy of antidepressants or antipsychotics in some cases (Carvalho et al., 2013, Muller, 2018, Konsman, 2019, Kohler-Forsberg et al., 2019, Kappelmann et al., 2018, Balu, 2016). Therefore, a few studies argue that some antipsychotic medications are in-part beneficial because of their immunosuppressive effect. In a recent study, researchers were able to predict an autism spectrum disorders (ASD) diagnosis with an accuracy of 90% by analyzing the blood levels of biomarkers for cuproptosis, a form of programmed cell death involving excess intracellular copper (Zhou and Gao, 2022). It has been long believed that ASD could underlie a form of immunological disorder. In this case, it is possible that gene mutations in cuproptosis are the cause of immunoactivity. Taken together, it is not surprising that some hard to manage neurological disorders could have some immunological factors in play.

3.1.1. Blood-brain barrier

Unlike all other organs, the blood supply of the brain is unique in two aspects (Trepel et al., 2015): **I)** Most organs like the liver, lungs, and kidney have a hilus, which is a depression or an opening, through which blood vessels and nerves enter the organ. The brain, on the other hand, has a large network of arteries that run along its surface in the sulci and other grooves and then enter it from all directions. **II)** While various tissues in the human body, including heart, lungs, skeletal muscles, and fat tissues all possess continuous capillaries, the brain's capillaries stand out for their unique

characteristics. They feature tightly woven endothelial cells with highly pronounced tight junctions (a multiprotein complex that tightly anchors cells together), creating a robust seal between them. In the human body, there are primarily three types of capillaries that have evolved to efficiently regulate the transport of molecules from the bloodstream to the parenchyma of organs. These include continuous capillaries, where endothelial cells are interconnected through adhesion proteins; fenestrated capillaries, which share similarities with continuous capillaries but are distinguished by small pores or "fenestra" in their membranes; and discontinuous capillaries, characterized by substantial gaps within their walls. Typically, the intercellular spaces between endothelial cells in continuous capillaries are loosely sealed by tight junctions. This allows for the passive passage of water, glucose, and other small, lipophobic molecules. However, the brain's capillaries differ significantly due to their high density of tight junctions, which effectively seals the intercellular spaces, preventing the passage of most molecules. This unique feature plays a crucial role as a part of the blood-brain barrier (BBB).

The tightly packed endothelial cells, their basement membrane and the astrocytes end-feet that wrap around the capillary and closely cover it, form the three layers of the BBB (Trepel et al., 2015). The BBB with its selective permeability controls the influx of many molecules, antibodies, and immune cells, maintaining the unique microenvironment of the brain. Only very small lipophilic molecules, such as oxygen and carbon dioxide, can still diffuse freely across the BBB - all other molecules require carrier proteins for passage. The astrocytes have immunological functions, discussed in the next section, in addition to their role in the BBB structure. With the help of some key protein complexes and transporters, astrocytes act as a link between blood vessels and brain parenchyma. They can, for example, regulate the water and ion homeostasis by Aquaporin-4 (Mader and Brimberg, 2019). Astrocytes can also affect the contraction and dilation of capillaries and arterioles, thereby regulating blood flow, based on the activity of nearby neurons (MacVicar and Newman, 2015). This change in blood flow, in addition to the change in blood oxygenation level, underlies the detection of neuronal activity through blood-oxygen-level-dependent (BOLD) imaging in functional magnetic resonance imaging (fMRI) (Glover, 2011).

3.1.2. The role of immune cells in the brain

The BBB imposes a challenge for immune cells to conventionally wander into brain tissue and monitor for pathogens. Instead, a diverse array of specialized immune cells is found within the CNS, including microglia, astrocytes, and perivascular macrophages. Microglia are a type of macrophages that account for about 10-15% of cells in the CNS. They constantly survey for pathogens and act as the first line of defense in the brain. Microglia are very sensitive to the presence of anything that might affect neurons, such as plaques, synaptic proteins and infections antigens. During their surveillance they also clean up any remains from damaged neurons and synapses, therefore they are known as the "housekeepers" of the CNS. Once they become activated by the detection of harmful substances, they can secrete IFN- γ and alert nearby microglia, converting them to antigen presenting cells. They produce an array of cytokines and chemotactic substances that recruit other immune cells and enables them to cross the BBB. IFN- γ can lead to the decrease in tight junctions in endothelial cells and increase the permeability of the BBB (Bonney et al., 2019). Microglia have a dual effect on the permeability of the BBB. They can either express the tight junction protein Claudin-5 and make contact with vessels to maintain an intact BBB, or they can phagocytose astrocytes' end-feet to increase permeability. Damage in

the BBB can also lead to the release of cytokines and chemotactic substances that attract immune cells to the CNS.

3.1.3. Antibodies in the adult and fetal brain

Antibodies are primarily produced by differentiated B-cells (plasma cells) in the bone marrow, lymph nodes, spleen and other lymphatic tissues, and then circulate in the blood (Boothby et al., 2022, Slifka et al., 1995, Morris, 2021). Under normal circumstances, antibodies can't cross the BBB and reach the brain. During neuroinflammatory diseases, however, the BBB can be opened in a controlled manner for the passage of antibodies. Microglia can regulate the permeability of the BBB as mentioned previously. Immune cells such as CD4+ T-lymphocytes can also increase the permeability of the BBB by the secretion of IFN- γ (Iwasaki, 2017). Injury or damage to the BBB can allow circulating antibodies to reach brain parenchyma as well. The exact mechanism, in which anti-neuronal antibodies can cross the BBB in autoimmune encephalitis, is not yet discovered. However, there are some theoretical alternative routes in which antibodies can reach brain parenchyma (Platt et al., 2017). One of those routes might be the Blood–Cerebrospinal Fluid Barrier (BCFB). This barrier is similar to the BBB, but less tightly regulated than the latter. In experimental autoimmune encephalitis, T_H-17 lymphocytes are able to cross the BCFB days before they can cross the BBB. Therefore, it is suggested that antibodies might also be able to cross the BCFB easily and faster and reach brain parenchyma.

During development, the embryo and fetus don't have a fully functional immune system, which is able to produce antibodies to fight potential pathogens (Hussain et al., 2022). Instead, the developing organism relies on the immunity of the mother and the maternofetal (or placental) transfer of IgG antibodies. Some studies suggest that fetus can start to produce antibodies in the last stages of pregnancy (Hayward, 1983). But most of the produced antibodies are against maternal antigens and are from the IgM type, which is a "rough draft" of antibodies that have low affinity to their target. The placental transfer of antibodies starts approximately in the 13th gestational week in humans (Pierzynowska et al., 2020, Palmeira et al., 2012) or around the 15th gestational day in mice (E15) (Appleby and Catty, 1983). The development of the BBB seems to depend on many factors and seems to start as early as at the 8th gestational week in humans. The BBB only becomes fully functional in later stages of pregnancy, i.e. in the third trimester in humans and at a similar stage in mice (Haddad-Tóvolli et al., 2017). This suggests that during the early stages of pregnancy, maternal antibodies might still be able to cross the not yet fully developed BBB and reach brain parenchyma. Hence, anti-neuronal antibodies, such as NMDAR-Ab, could have an effect on the developing brain.

3.2. Autoimmune encephalitis

Autoimmune encephalitis, often abbreviated as AE, are a group of brain inflammation disorders that are caused by the production of antibodies that target neuronal or synapse-specific proteins (Heine et al., 2023, Prüss, 2021). The clinical presentation of AE can be polymorphic, depending on the specific antibodies and subtype of AE, often mimicking psychiatric, neurological, and infectious conditions at the same time, which could lead to misdiagnoses and delayed intervention (Graus et al., 2016). Usually, they can be managed with immunomodulation and supportive care. These conditions can currently be classified into two subgroups (AMBOSS GmbH, 2023): classical paraneoplastic and facultative paraneoplastic AE.

3.2.1. Classical paraneoplastic AE

Classical paraneoplastic AE are almost always tumor associated, usually with aggressive tumors such as small-cell lung cancer, breast carcinoma, Hodgkin-Lymphoma, etc., and rarely occur without one (Heine et al., 2023, Brackowski et al., 2023). They usually start with the tumor cells producing and presenting antigens similar to neuronal structures. Then, as a part of the immune reaction against the tumor cells, some antibodies produced against those tumor antigens can also target and affect neurons. In some cases, the tumor cells themselves produce antibodies that target neuronal structures, like in macroglobulinemia (Baehring et al., 2008). In both cases, the binding of antibodies to neuronal structures leads to an activation of cytotoxic T-cell response and brain inflammation. Those antibodies tend to target intercellular structures in neurons and there is already a handful of well-characterized antibodies (Anti-Hu, Anti-Yo, etc.) and another few of rarer and less characterized ones (Anti-ANNA-3, Anti-PCA-2, etc.) identified.

3.2.2. Facultative paraneoplastic AE

Facultative paraneoplastic AE, on the other hand, can occur without any clear link to tumors (AMBOSS GmbH, 2023). In fact, some of these conditions occur more idiopathically rather than as paraneoplastic syndrome (Titulaer et al., 2013, Xu et al., 2020b, Gong et al., 2021), and, therefore, could be considered more of a true autoimmune disorder. Interestingly, unlike classical paraneoplastic AE, the targets of the immunoactivity are surface structures. The most prevalent form is the anti-NMDA receptor encephalitis (NMDARE), with antibodies that target NMDA receptors. In some other forms, the target could be AMPA receptors, GABA receptors or voltage-gated ion channels.

3.3. Anti-NMDA receptor encephalitis

NMDARE was first described in 2007 in a case report of 12 female patients with ovarian teratoma (Dalmau et al., 2007). This condition arises when antibodies mistakenly target NMDARs in the brain, resulting in a wide range of neurological and psychiatric symptoms. Although NMDARE is a rare disorder, it is the most prevalent form of AE. Epidemiological studies showed that NMDARE can occur in individuals without underlying tumors. The condition predominantly affects females in adolescence and young adulthood, making early diagnosis and intervention crucial for effective treatment.

3.3.1. Epidemiology

Due to the recent discovery of the disease, no definitive epidemiological data exist yet. The increased awareness of NMDARE has led to an increase in the number of diagnosed patients in recent years. A multicentric study from 2011 by Dalmau et al. (2011) was able to identify over 400 patients in 3 years. Another study from a single medical center in Taiwan identified 24 patients retrospectively from 2009 to 2017 (Kong et al., 2019). NMDARE is apparently more prevalent in children and young adults. Almost 80% of identified patients are females (Dalmau et al., 2019). The exact percentage of tumor associations seems to differ from one center to the other and depends on the age of the patient. Therefore, it is advised to screen for teratomas in young female patients.

3.3.2. Pathophysiology

The effect of the antibodies isolated from NMDARE patients has been examined in cell culture and mouse model (Dalmau et al., 2019). Studies showed that NMDAR-Abs bind to the GluN1 subunit of the receptors and crosslink them (Kreye et al., 2016, Masdeu et al., 2016). This leads to altered surface dynamics of NMDARs and disrupted interaction with other synaptic proteins. One such protein is the Ephrin type-B receptor 2 (EPHB2R), which plays a very important role in the clustering of NMDA receptors and synaptic organization (Liu et al., 2008). Eventually, the crosslinked NMDARs get internalized, leading to a decrease of NMDARs' synaptic density (Masdeu et al., 2016, Kreye et al., 2016). On the network level, the effects of the antibodies have been shown to potentially affect the structural development of the network, as they can reduce dendritic branching and impair dendritic maturation (Okamoto et al., 2022).

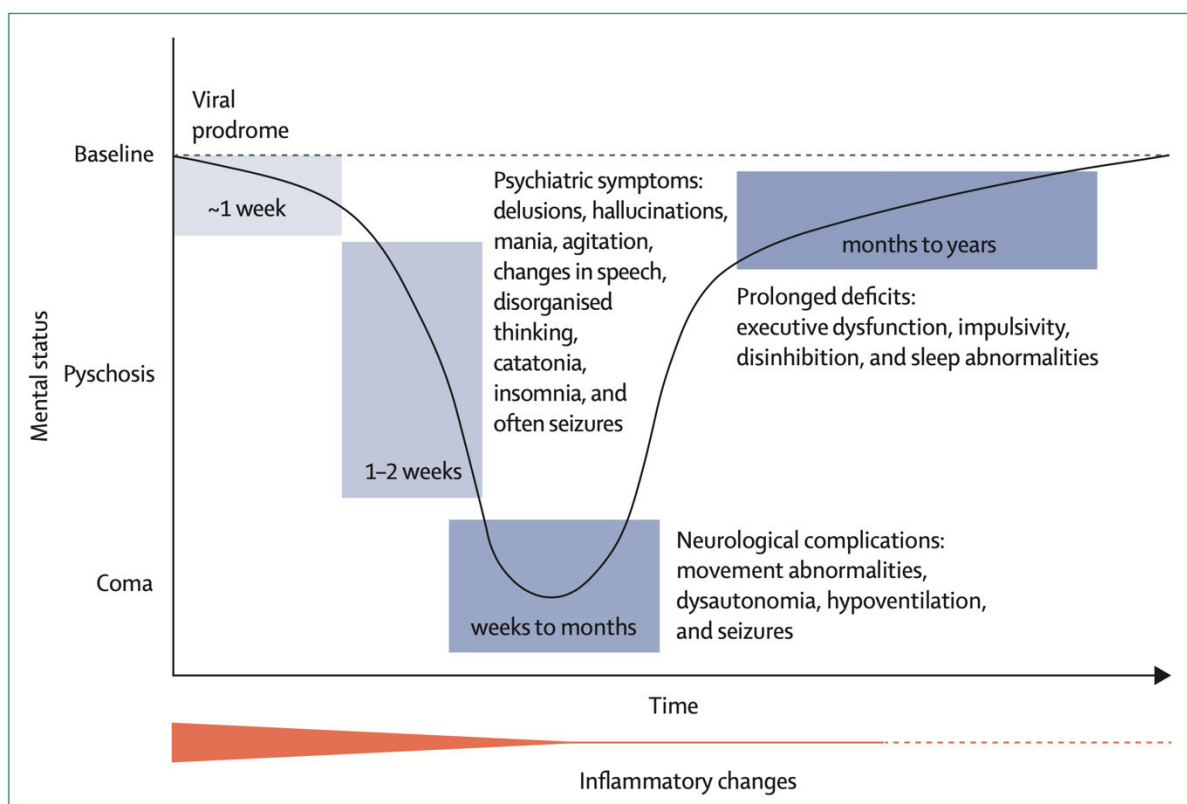


Figure 1: Clinical presentation of NMDARE at various stages.

The disease typically starts in a prodromal phase of about one week with viral-infection-like symptoms. In the following days, patients' condition worsens, and they can develop psychiatric symptoms. Some patients show neurological and autonomic symptoms and may even go into a coma. At the final stage, patients can start to gradually recover with a significant portion of them having prolonged deficits that can last for years or never improve. Adapted from (Dalmau et al., 2019) with permission.

3.3.3. Symptoms

The course of the disease is divided into 4 or 5 phases (Figure 1), depending on the literature being followed, although an atypical course is not uncommon. Approximately 70% of patients initially develop viral-infection-like symptoms (prodromal phase) that can last up to 2 weeks. After that, it rapidly changes to a schizophrenia-like psychosis that could be accompanied by seizures (psychotic and/or seizure phase). Some patients could even develop memory loss. Yet, due to such patients also developing

speech difficulties, memory loss can remain unnoticed. At the next phase (autonomic dysfunction phase), patients can start showing autonomic dysfunction and may require life-support. After some time, the patients start to gradually recover from the disease, but some symptoms may not clear up completely and a relapse into a new episode is not uncommon. Many patients exhibit prolonged neurological and psychiatric symptoms even after immunomodulatory treatment, with long-term cognitive deficits affecting up to two thirds of all patients (Heine et al., 2021).

3.3.4. Diagnostics

NMDARE is generally diagnosed by testing for a high level of anti-NMDAR antibodies in blood and liquor samples, while screening for tumors and excluding other causes of the symptoms. A clear consensus on diagnostic criteria (**Panel 1**) was first established in 2016 (Graus et al., 2016). Unfortunately, MRI and PET scans showed an insufficient sensitivity for NMDARE, so the diagnosis still heavily relies on screening for anti-NMDAR antibodies. On the other hand, electroencephalogram (EEG) can show abnormalities in up to more than 90% of patients and is therefore included in the diagnostic criteria.

Probable anti-NMDA receptor encephalitis:

Diagnosis can also be made in the presence of three of the groups below of symptoms accompanied by a systemic teratoma

1. Rapid onset (less than 3 months) of at least four of the six following major groups of symptoms:
 - Abnormal (psychiatric) behavior or cognitive dysfunction
 - Speech dysfunction (pressured speech, verbal reduction, mutism)
 - Seizures
 - Movement disorder, dyskinesias, or rigidity/abnormal postures
 - Decreased level of consciousness
 - Autonomic dysfunction or central hypoventilation
2. At least one of the following laboratory study results:
 - Abnormal EEG (focal or diffuse slow or disorganized activity, epileptic activity, or extreme delta brush)
 - CSF with pleocytosis or oligoclonal bands
3. Reasonable exclusion of other disorders

Definite anti-NMDA receptor encephalitis

Diagnosis can be made in the presence of one or more of the six major groups of symptoms and IgG anti-GluN1 antibodies, after reasonable exclusion of other disorders.

Panel 1: Criteria for diagnosing NMDARE.

The diagnosis of NMDARE can be classified as probable or definite depending on the number of met criteria. Testing for antibodies should always include testing of cerebral spinal fluid (CSF), since the presence of antibodies in the serum is less conclusive. GluN1 is the glycine-binding subunit of NMDAR. Adapted from Graus et al. (2016) with permission.

3.3.5. Therapy

The best treatment for tumor associated NMDARE is the removal of the tumor. Currently, the first line of therapy is immunomodulation and is recommended for all patients. This includes high-dose steroids, intravenous immunoglobulin, or plasmapheresis. In the case of a weak or absent response to the first-line treatment, targeted B-cell therapy with Rituximab is recommended. In five very severe cases, one center tried eliminating the source of the antibodies, i.e., short- and long-lived plasma cells, with Bortezomib and noticed an improvement in the patients after a couple of treatment cycles. Depending on the symptoms of the patient, other supportive therapies could also be indicated. These could include antipsychotic therapy for patients with psychiatric symptoms, antiepileptic therapy in the presence of seizures, or life-support and intensive monitoring in the case of bad autonomic dysregulation and/or loss of consciousness.

3.3.6. Prognosis

The long-term effect of the disease is not yet fully clear. Recovery may be gradual, and some patients don not recover completely, exhibiting prolonged neurological disabilities. Furthermore, a relapse into a new episode of NMDARE is possible. Early diagnosis and prompt initiation of appropriate treatment can significantly improve the prognosis. In many cases, especially those diagnosed and treated early, patients can experience substantial recovery and return to normal or near-normal functional state. In 2019, Balu and colleagues introduced a score system to predict the outcome of the disease after 1 year of symptoms onset (Balu et al., 2019). This model uses a 5 points system and is called the anti-NMDAR Encephalitis One-Year Functional Status (NEOS) score. In this system, a point is awarded to each of the following criteria:

- Requirement for ICU admission.
- Delayed treatment of 4 weeks after symptom onset.
- Absence of improvement within the first 4 weeks treatment.
- Abnormal brain MRI.
- Elevated white blood cell count in CSF (>20 cells/ml).

The score can range from 0 to 5, with a score of 5 correlating with the worst 1-year functional outcome. Although the NEOS was developed from analyzing the outcomes of adult patients, it could also be reliable for children with NMDARE, according to later independent studies (Loerinc et al., 2021, Nikolaus et al., 2023).

3.4. NMDA Receptors

NMDARs are one of the 3 types of ionotropic glutamate receptors (Brandes et al., 2019). The naming of the receptors comes from the agonist N-methyl-D-aspartate. NMDA binds selectively to those, distinguishing them from the two other glutamate receptors, AMPA and Kainate receptors. NMDARs are postsynaptic receptors that can be found throughout the CNS, most notably in the cortex and hippocampus. Their structure is typically a heterotetramer composed of two glycine-binding (GluN1) and two glutamate-binding (GluN2) subunits (Yamamoto et al., 2015, Salussolia et al., 2011). Therefore, both glutamate (Glu) and glycine act as agonists for the receptors. When activated, NMDARs allow an outflux of K^+ and an influx of Na^+ and Ca^{2+} ions.

Under resting membrane potential, Mg^{2+} ions can bind to the NMDAR and block it (Brandes et al., 2019). Only after a high depolarization, Mg^{2+} unblock the receptors and allow the influx of Ca^{2+} (Figure 2). This makes NMDA receptors play a very

important role in long-term potentiation (LTP) and thus a key role in modulating synaptic plasticity and controlling learning and memory functions. LTP is a complex process that leads to the strengthening of synaptic connections between neurons (Cooke and Bliss, 2006). The influx of Ca^{2+} by NMDAR triggers an internal cascade of proteins and processes that lead to an increment of neuroreceptors at the postsynaptic membrane (Figure 2). These changes in receptor density increase the sensitivity of the postsynaptic cell and make transmission of signals between neurons more efficient. Consequently, the neural circuit can respond similarly to identical stimuli in the future, facilitating the encoding of information and the formation of memories.

NMDARs have been found to be involved in many neurological disorders. Their dysfunction has been linked to dementia and neurodegeneration due to hyperactivity (excitotoxicity). NMDAR dysfunction and a shift towards increased excitation is implicated in ASD (Lee et al., 2015, Canitano and Palumbi, 2021). Most notably in schizophrenia, it is widely believed that disruption of NMDAR signaling plays a role in the pathophysiology (Steullet et al., 2016, Teixeira et al., 2017).

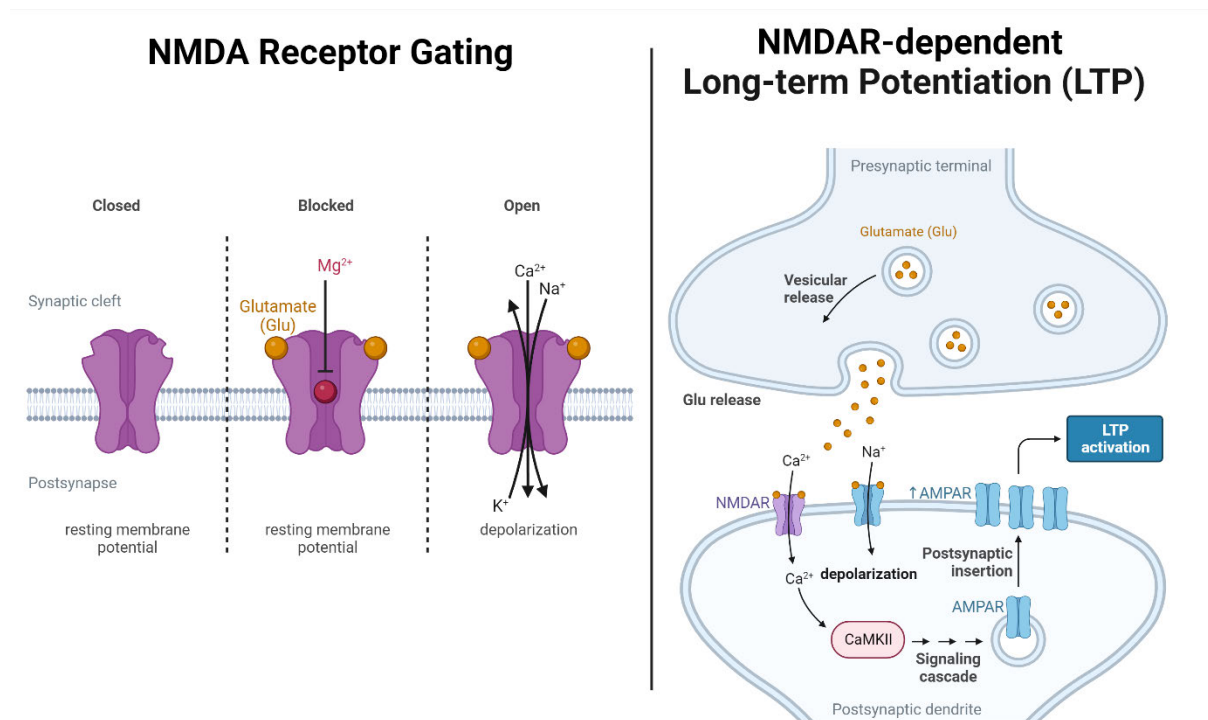


Figure 2: NMDA receptors' gating and their role in long-term potentiation.

The gating of NMDARs depends heavily on the membrane potential of the cell (left). Under resting membrane potential and lack of neurotransmitter (Glu or glycine), the receptors are closed. When bound to by neurotransmitter, they change conformation and open, allowing Mg^{2+} to reach an internal binding site. The receptors are thus blocked by Mg^{2+} and don't allow the passage of ions. Only when the cell is depolarized, Mg^{2+} leaves the internal site and allows the influx of Ca^{2+} and Na^+ and the outflux of K^+ . The influx of Ca^{2+} can then play a role in LTP (right). During this process, the presynaptic neuron releases glutamate into the synaptic cleft. Glutamate binds to AMPA and NMDA receptors on the postsynaptic neuron, leading to depolarization and influx of Ca^{2+} . This triggers a cascade of molecular events, including the activation of protein kinases and the insertion of additional receptors on the postsynaptic membrane. Figure created with BioRender.com.

3.5. Basics of functional calcium imaging

Over the years, the field of neuroscientific research has evolved to recognize the role of single neuron interactions in the network instead of the idea that large parts of the brain are solely responsible for a specific function (Altahini et al., 2023, Zatzka-Haas et al., 2021, Steinmetz et al., 2019, Singer, 2009). This recognition comes from the advancements in the tools used for studying complex interactions within neural networks. At the top of the list of such transformative tools are functional calcium imaging and two-photon microscopy. Calcium imaging is a microscopy technique to measure the calcium concentration of cells. It was first used to study the activity of neurons in the 1980s (Grienberger and Konnerth, 2012). Almost 10 years later, the development of two-photon microscopy allowed for imaging in highly diffracting tissues, like the brain. The two techniques were first combined in 2015 to examine the activity of astrocytes during seizures *in vivo* (Russell, 2011, Tian et al., 2005). With the advancements in the field of multi-photon microscopy and calcium indicators, calcium imaging is the state of the art when it comes to *in vivo* multi-neuronal imaging. Compared to other methods for examining a large number of neurons simultaneously, such as electrophysiology recordings using probes, calcium imaging is less invasive and offers a single cell resolution.

3.5.1. Calcium ions in neurons

Calcium imaging can measure the relative change of Ca^{2+} over time. Neurons typically have around 100 nM Ca^{2+} that can rise up to 100x during activity (Gleichmann and Mattson, 2011, Grienberger and Konnerth, 2012). Ca^{2+} ions are involved in many processes like the release of neurotransmitters and the modulation of synaptic plasticity as mentioned above. Most importantly, they serve as a second messenger, conveying the change in membrane potential to intracellular machinery (Gleichmann and Mattson, 2011). This key aspect allows the use of the rapid, yet transient increment of free cytosolic Ca^{2+} concentration as a proxy for action potentials and neuronal firing.

The low intracellular concentration of Ca^{2+} in activity free phases is maintained by active pumps that transport calcium ions out of the cell, namely by the Plasma-Membrane Ca^{2+} -ATPase (PMCA) and the $\text{Na}^+/\text{Ca}^{2+}$ Exchanger (NCX) (Berridge et al., 2003). In addition, Ca^{2+} is stored in the endoplasmic reticulum (ER) and mitochondria and is actively transported into them by the Sarcoendoplasmic Reticulum Ca^{2+} -ATPase (SERCA) and the Mitochondrial Uniporter, respectively. Each of those pumps has a different transport rate and affinity, which enables the cell to react efficiently to a wide range of Ca^{2+} concentrations. Stored Ca^{2+} is then slowly released from the mitochondria by the NCX to be stored in the ER or exported outside of the cell. The rapid rise of Ca^{2+} concentration, on the other hand, can result from the influx by the opening of voltage gated Ca^{2+} channels (VGCC), which react to the depolarization of the cell (Catterall, 2011). Similarly, ryanodine receptors can be activated by the excitation of the cell and release stored Ca^{2+} from the ER. The influx of Ca^{2+} can also directly result from the activation of Ca^{2+} permeable receptors like ionotropic glutamate (iGluR) receptors, nicotinic acetylcholine receptors (nAChR) or transient receptor potential (TRP) channels (Berridge et al., 2003, Shen and Yakel, 2009). While iGluR and nAChR are activated by neurotransmitters, TRP channels can be activated by many chemical, mechanical or thermal stimuli (Zheng, 2013).

3.5.2. Calcium indicators

Calcium indicators are molecules that increase in fluorescence when they bind to Ca^{2+} , therefore transforming changes in the ions' concentration into measurable light signals (Grienberger and Konnerth, 2012). As mentioned above, the activation of neurons leads to a high influx of Ca^{2+} . Calcium indicators can be used to detect this rapid change in intracellular Ca^{2+} concentrations and indirectly detect action potentials. In 1985, Grynkiewicz and colleagues introduced Fura-2 as the first calcium indicator to be widely used for imaging (Grynkiewicz et al., 1985). Since then, the development of new and better indicators continued. The various indicators differ in their excitation and emission wavelength, affinity to Ca^{2+} , strength of fluorescence, and kinetics (Lohr et al., 2021). There are mainly two types of calcium indicators: synthetic or chemical indicators and genetically encoded calcium indicators (GECI).

Synthetic indicators, such as Oregon Green Bapta-1 (OGB-1), consist of a calcium-sensitive chelator and a fluorophore. These dyes are usually lipophilic, and thus, they can be loaded into the cells or directly injected inside them to be used immediately for imaging (Paredes et al., 2008). Another advantage of OGB-1 specifically, is the linear change in fluorescence with increasing number of action potentials (Hendel et al., 2008). This was demonstrated by simultaneous two-photon calcium imaging and patch clamp recordings (Rocheffort et al., 2009). The downside of chemical indicators is their limited ability to target a specific subpopulation of cells, for example only excitatory neurons.

GECIs, on the other hand, consist of the fusion of one or more fluorescent proteins with Ca^{2+} binding sites. By the combination of the right viral vector and promotor (Altahini et al., 2023, Oh et al., 2019), GECIs can be used to induce targeted expression in specific cell types or to even produce transgenic animals. Thus, GECIs are a very powerful tool for *in vivo* imaging of cellular activity, not only in neurological circuits, but also in many physiological processes (Mollinedo-Gajate et al., 2019, Kaestner et al., 2014). In neuroscience, the family of GCaMP indicators is most widely used (Dana et al., 2019). They consist of circularly permuted Green Fluorescent Protein (cpGFP), a calcium-binding protein calmodulin (CaM) and CaM-binding M13 domain (Akerboom et al., 2009). The binding of Ca^{2+} causes the CaM and M13 to change conformation and overlap, blocking H^+ from entering the GFP (Figure 3A). This causes GFP to increase in fluorescence. Although GCaMP indicators are a very powerful tool to target specific local circuits and neuron types, they do not provide a linear signal to action potentials (Fu et al., 2021, Zhang et al., 2023).

3.5.3. Two-photon microscopy

The first two-photon microscope was developed by Winfried Denk and James Strickler in the 1990 (Denk et al., 1990). At the heart of two-photon microscopy lies the principle of multiphoton or nonlinear excitation. Instead of employing a single high-energy photon to excite a fluorescent molecule, multiphoton microscopy can utilize two or more lower-energy photons that have to be absorbed simultaneously, i.e. within 10^{-15} seconds (Göppert-Mayer, 1931). This approach provides several key advantages: deeper tissue penetration, reduced scattering and absorption, and minimized photodamage to the imaged sample (Denk and Svoboda, 1997). Also, because the two-photon excitation can only occur at the focal point of the system, background fluorescence from the sample can be reduced and the imaging quality can be improved (Figure 3B). A typical two-photon imaging system would consist of a laser as a light source, a scanner system, and a light detection system (Figure 3C). The laser

needs to be powerful enough to deliver the light intensity necessary for two-photon absorption. Titanium-sapphire (Ti:Sa) lasers are most commonly used in biomedical research, since they produce high intensity light pulses in range from 640 to 1040 nanometers with a high repetition rate (Steele et al., 1991, Fu et al., 2021). The scanner is not very different from confocal microscope scanners, although some adjustments need to be made for the different laser source (Denk and Svoboda, 1997). Lastly, photomultiplier tubes (PMTs) are the typical detectors in two-photon microscopes, because of their very high sensitivity capability of detecting weak fluorescence signals.

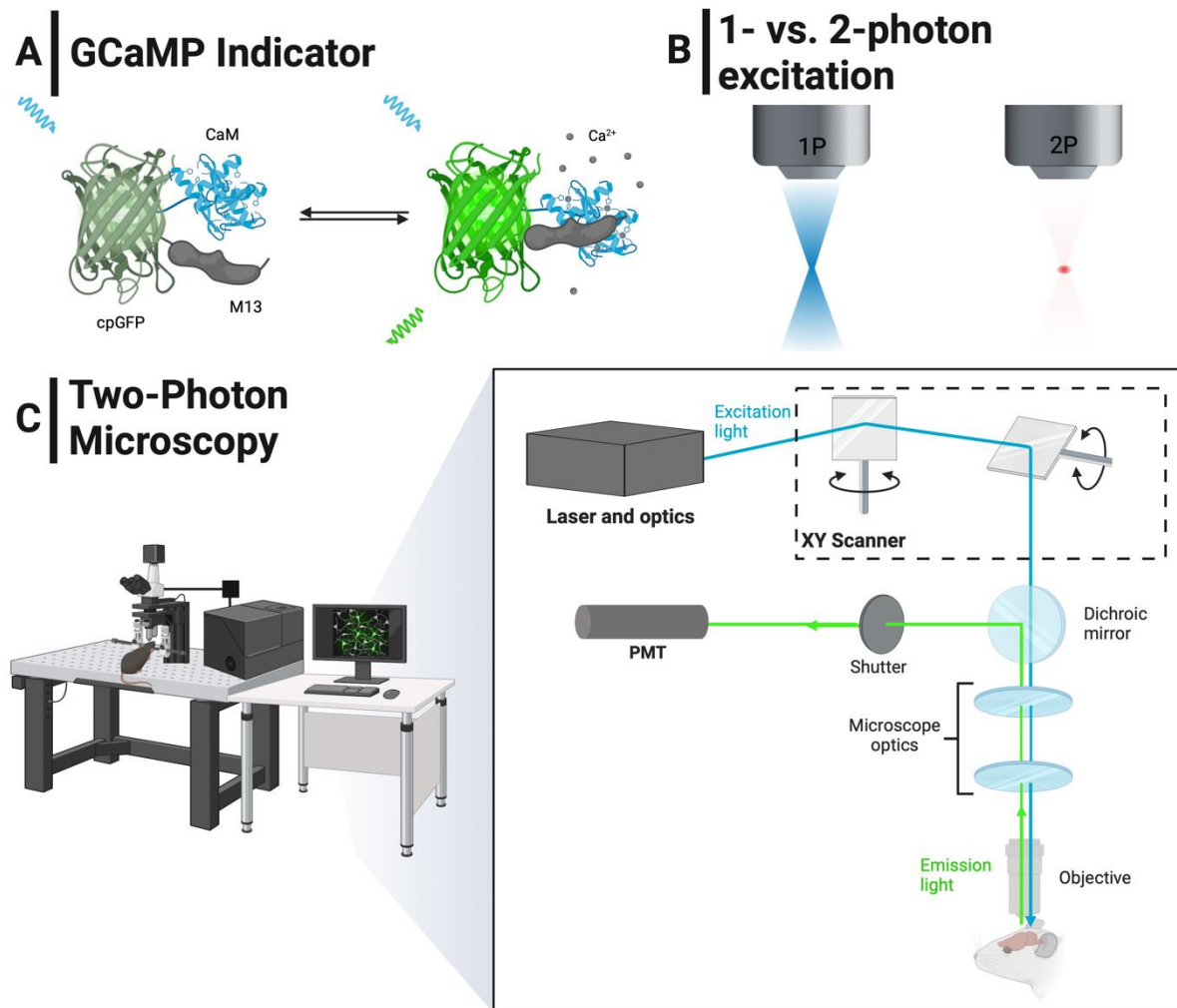


Figure 3: Changes in GCaMP indicator conformation and comparison of microscopy techniques.

(A) Schematic representation of a GCaMP indicator molecule consisting of a permuted Green Fluorescent Protein (cpGFP), a calcium-binding protein calmodulin (CaM) and CaM-binding M13 domain. The binding of Ca^{2+} to the 4 binding sites on CaM causes it and the M13 domain to overlap. This change in conformation repels H^+ from the GFP and allows it to fluoresce. **(B)** Fluorescence results obtained using one-photon and two-photon microscopy. In one-photon excitation, fluorescence can occur everywhere throughout the beam's path, whereas in the two-photon excitation, the simultaneous absorption necessary for fluorescence can only occur at the focal point. Thus, background fluorescence is eliminated from before and beyond the focal point. **(C)** Schematic illustration of a basic two-photon microscope setup. This setup includes a laser source, a scanner system, microscope optics for beam manipulation, and a photomultiplier tube (PMT) for signal detection. Figure created with BioRender.com

3.6. Analysis of functional calcium imaging data

The processing of calcium imaging data starts with a few standard steps before switching toward more unique analysis methods, which are custom-tailored to answer the questions of the study. The main goal of the common steps is to minimize any artifacts from the recording and extract the neuronal activity over time from the image series.

3.6.1. Motion Correction

The first step of the analysis after acquiring the data is to inspect the time series and look for any artifacts. The most common type of artifacts in *in vivo* imaging are motion artifacts. This is true for the recordings of both anesthetized and awake animals (Stringer and Pachitariu, 2019). Although the use of a head holder is a common practice for counteracting any motion during the recording, there still can be small movements because of the flexibility of the skull (Ren and Komiyama, 2021, Guimarães Backhaus et al., 2021). Small movements up to 15 microns in any direction in the field of view are enough to affect the trace extraction, especially in areas with high cell density. In anesthetized recordings, motion is relatively lighter and mostly caused by the breathing of the animal (Stringer and Pachitariu, 2019, Nietz et al., 2022). In awake recordings, it is caused by the activity of the animals, such as walking on a treadmill or a trackball, and is usually stronger and more irregular. Additionally, the pulsation of brain matter, caused by the beating of the heart, can also introduce movements in the field of view.

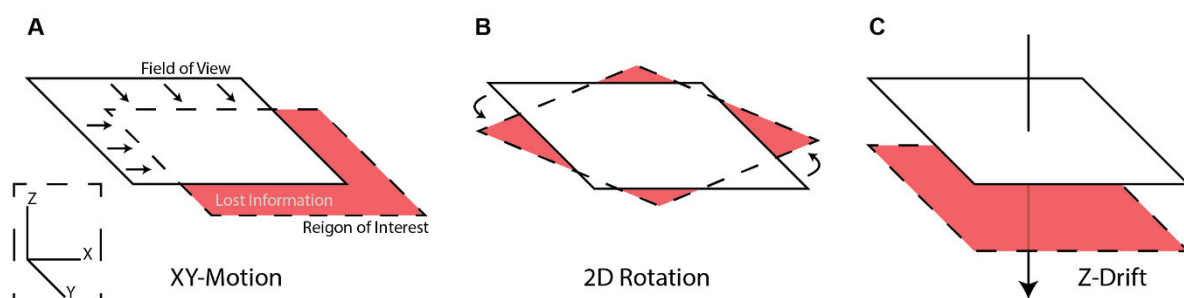


Figure 4: Loss of information in calcium recordings due to motion artefacts.

(A) XY-motion artefacts are caused by the movement of the region of interest (ROI) in the X or Y direction relative to the recorded field of view (FOV). **(B)** 2D rotation occurs as a result of a loose head holder. If the tolerances of the head holder are not tight enough, the ROI can rotate in the same 2D plane as the FOV. **(C)** Z-Drift is the most detrimental artefact of all 3. The sliding of the ROI above or below the FOV will result in the recording of a new site and the complete loss of information about the original ROI. Red areas indicate a loss of information.

The 3 most common types of movement artifacts in awake imaging are XY-motion, 2D rotation and Z-drift (Stringer and Pachitariu, 2019). XY-motion or simple 2D motion is caused by the motion of the recording site, or region of interest (ROI), in the X or Y direction relative to the microscope's objective (Figure 4A). This can be easily corrected by setting a reference frame, calculating the distance of each subsequent frame from it, and moving them back to the reference frame. Because a portion of the ROI moves outside of the field of view (FOV), the information about the cells at the edges of the field of view does not get recorded and gets lost. For this type of movement artifacts a few popular solutions already exist. Some of those solutions require the user to define landmarks in the frame of reference to compare their

positions in the image series. Some newer and more advanced solutions can compare whole frames to the frame of reference. One such popular solution is MoCo by Dubbs et al. (2016). Moco is a java-written ImageJ plugin that uses a mathematical approach (Fourier-transform) to compare each frame to a reference frame and calculate an X and Y-distance to minimize the differences between the frames. It also uses a cached down-sampling method to reduce computation time.

2D rotation is a special case of 2D motion artifacts (**Figure 4B**). Similarly to XY-motion, some information about the recording site can get lost but the majority can be corrected. It is important to note that, unlike other motion artifacts, the skull is not flexible enough to allow a high magnitude of rotation (Stringer and Pachitariu, 2019). Thus, a 2D rotation is considered more of a sign of a loose head holder and should be corrected by adjusting the holder tolerances. Due to the intricacies of this artifact and its tendency to coincide with other forms of motion artifacts, it can be more computationally intensive to correct post-hoc. On the other hand, Z-drift is caused by the relative movement of the recording site in the Z or depth axis (**Figure 4C**). Unfortunately, when the whole recording site moves outside of the FOV, all information pertaining to the cells becomes irretrievably lost. Therefore, this type of artifact cannot be corrected post-hoc. In such cases, the only solution is to limit subsequent analytical steps to the frames captured before or after the occurrence of this artifact.

3.6.2. Segmentation

The next step is to locate the cell bodies (somata) and define them as ROIs (**Figure 5**). This step is crucial for the trace extraction and can influence the quality of the analysis heavily. The segmentation can be done manually by creating an intensity projection of the image series and drawing polygons around potential cell bodies, or automatically with the help of various segmentation algorithms. The two methods could also be combined into a semi-automatic approach, where an algorithm does an initial segmentation, and the examiner could then inspect the results and manually refine them by adding more ROIs or removing them.

Today, a handful of automatic segmentation software exists. Some of those solutions utilizes a defined mathematical algorithm, such as non-negative matrix factorization (Giovannucci et al., 2019, Pachitariu et al., 2017), to extract groups of neighboring pixels with similar florescent intensity curve and define them as ROIs. This approach could be very quick and powerful for detecting active cells even in recordings with low signal-to-noise ratio (SNR), since they do not rely on the morphology of the cell, but rather on the change in fluorescence compared to the background. This, however, poses some challenges. Silent cells do not differ much from the background in intensity changes during the recording. Therefore, silent cells could be mistakenly discarded by those algorithms. Another challenge is that small cell compartments, like axons and dendrites, also show changes in fluorescence but their signals may be undesirable for the analysis. Therefore, such algorithms require a number of parameters to be set manually by the user to help them differentiate between somas and neuropil. This requires a lot of trial and error and makes the implementation a bit complicated. CalmAn, for example, tries to mitigate this problem by using a machine learning model to classify the output of its non-negative matrix factorization algorithm (Giovannucci et al., 2019).

With the advancements in the field of computer vision, some machine learning models have come to play in the field of calcium imaging segmentation as well. In the last few

years, at least 7 new machine-learning-based solutions have been introduced (Soltanian-Zadeh et al., 2019, Dolev et al., 2019, Kirschbaum et al., 2019, Bao et al., 2021, Sità et al., 2022, Xu et al., 2023). Such applications rely heavily on the morphology of the cells and less on the changes in fluorescence. This increases their ability to detect silent cells. Their performance, however, could be very limited, especially in low SNR recordings.

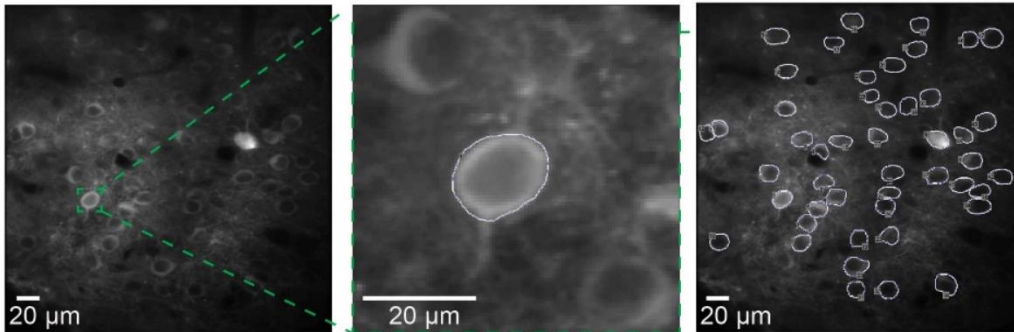


Figure 5: Manual segmentation of cell bodies into regions of interest.

In this step, cells' somata are defined as regions of interest for trace extraction. This can be done manually over an average intensity projection of the recording. Adapted from Guimarães Backhaus et al. (2021) with permission.

3.6.3. Trace Extraction

After having a defined set of ROIs, the process of converting the image series to traces of fluorescence values over time can be started. For this, the intensity values for the pixels of each ROI are averaged from each frame. Since those absolute values represent arbitrary brightness units and can be influenced by many factors, such as the calcium indicator used, the laser power and the gain of the PMTs, it's more useful to convert the fluorescence traces to the relative change in fluorescence over time, a so called $\Delta f/f$ trace. For this, some approaches need the user to define an activity-free interval as a baseline for each trace. Other approaches, like the baseline calculation script from the Allen Brain Institute (Allen Institute for Brain Science, 2023), utilize a short and long median filters in a rolling window for estimating the baseline and short timescale detrending. One advantage of this automatic baseline calculation approach, besides not needing an input from the user, is that it's impervious to indicator bleaching. If the imaging was done with high laser power or for a very long duration, the fluorescence of the cells at the end of the recording might be lower than at the start. With a manual baseline definition, this will appear as a slope in the final $\Delta f/f$ traces. However, since the automatic approach uses a rolling window, the slope is mitigated without affecting the resolution or quality of the traces.

3.6.4. Further analysis

Beyond the fundamental steps mentioned above, the possibilities of subsequent analysis methods diversify significantly. This diversity emerges due to the complex nature of neural data and the specific research objectives of each study. The endpoints of analyses and comparisons have to be tailored to the specific research questions. In most studies, all subsequent steps are based on one of the following approaches.

3.6.4.1. Raw Trace Analysis

Some publications base subsequent analyses on the raw calcium traces directly without binarization of transients, like in Somarowthu et al. (2021) as a recent example. This can also involve regression or correlation analysis to discern patterns and interactions within neural populations (Hamm et al., 2017). The idea behind this approach is to preserve the full complexity of calcium dynamics, which makes it especially pervious to noise and artefacts. Any high-intensity artefact that affects the whole FOV can be falsely interpreted as a simultaneous activity. This kind of analysis should only be considered after careful evaluation of the recording's quality. Another drawback of using this approach alone is that it does not deliver some fundamental metrics of neuronal populations, such as the firing frequency or inter-event interval (IEI). While comparing raw traces can provide information about the synchronicity of the cells, it falls short in characterizing individual cells' firing patterns. Therefore, it may be beneficial to complement raw trace analysis with other approaches to ensure a more comprehensive understanding of the neural activity under investigation.

3.6.4.2. Binary Traces for Calcium Transients

Another approach can involve detecting and binarizing calcium transients from raw calcium traces (Guimarães Backhaus et al., 2021). This could be simply accomplished by employing a thresholding technique to identify peaks in calcium concentration above a predefined threshold. The implementation is very straightforward and computationally efficient. However, thresholding on its own, could misidentify any artefacts as calcium transients. Calcium indicators, either GECl, such as GCaMP6, or synthetic, like OGB-1, typically have very characteristic transients. The transients can be seen as a sharp rise in fluorescence and a slow exponential decay of the signal. By filtering for transients that fit those characteristics and excluding any that do not, the results of the binarization can be improved. Such filtering can be done by utilizing an algorithm that looks for those criteria, for a fully automatic approach, or by manual refinement by the experimenter, for a semi-automatic approach. Since calcium recordings are usually noisy with a lot of baseline fluctuations, full-automatic transient detection can still have a high false positive rate. A semi-automatic approach could deliver better results, but could also be more time-consuming.

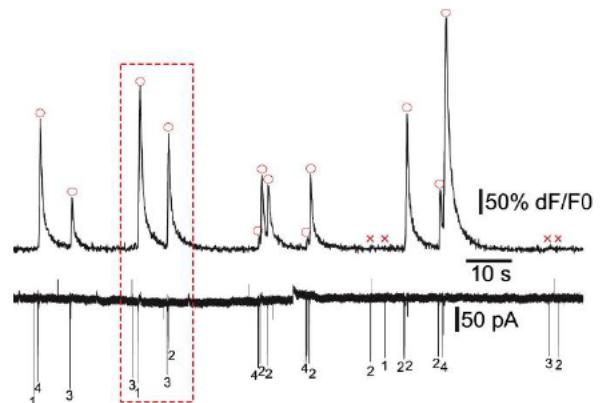


Figure 6: Simultaneous calcium imaging with GCaMP6f and electrophysiology.

This example highlights the low correlation between the amplitude of calcium transients and the underlying action potentials. The fourth transient is paradoxically smaller than the third transient, despite the higher number of spikes. Circles and crosses indicate detectable and non-detectable transients by thresholding. pA=picoAmpere. From Fu et al. (2021) with permission.

3.6.4.3. Spike inference

Spike inference aims to extract underlying neuronal spike (actual action potential) information from calcium traces. Most developments in this field were driven by the SpikeFinder challenge in 2016 (Berens et al., 2018). The challenge was sponsored by Carl Zeiss AG (Oberkochen, Germany) and provided open-access training and testing datasets of simultaneous calcium imaging, using OGB-1 and GCaMP6s, and electrophysiology recordings. Many algorithms and machine learning models were introduced to estimate the spike trains underlying observed calcium signal, but the challenge concluded that not a single approach was able to deliver reliable results. Knowledge of the precise time and number of spikes can lead to more comprehensive analysis of network dynamics. However, here, the assumption that a linear correlation between the calcium signal and underlying action potentials always exists, is very misleading. As mentioned before, some calcium indicators such as OGB-1, do have a linear relationship to the underlying cell firing (Hendel et al., 2008), but almost all GECIs do not. The closest one to have a predictable linearity is GCaMP8s, introduced in 2023 (Zhang et al., 2023). Even with linear calcium indicators, a simultaneous electrophysiology is necessary to establish the baseline relation, as it can vary from cell to cell (Wei et al., 2020). I.e., in mathematical terms, the slope of the correlation line might be known, but simultaneous electrophysiology is required to measure the intercept.

4. Material and Methods

4.1. Animals and disease model

All experiments were performed in accordance with the institutional animal welfare guidelines and were approved by the national investigation office (Landesuntersuchungsamt - LUA) of the state of Rhineland-Palatinate, Germany. To study the effects of NMDAR-Ab, a maternofetal transfer model was used with 7 pregnant C57BL/6 mice. The pregnant mice were each intraperitoneally injected twice with 240 µg of NR1-reactive monoclonal human antibody #003-102 (as a 300 µL solution) on E13.5 and E17.5 for a total of 480 µg antibodies (600 µL solution). For the control group, wild-type C57BL/6 mice were used. All animals were kept on 12h day/night cycle. Food and water were given ad libitum.

4.2. Virus injection and surgery

A viral solution containing AAV1.CamKII.GCaMP6f.WPRE.SV40 (Penn Vector Core, PA, USA, virus titer: 0,367*10¹²/ml) was used. Virus injection and chronic window implantation were performed for all animals age-matched on postnatal day 24. During the entire procedure, the animal's temperature and respiration rate were monitored. To start, the mouse was weighed and then placed in an anesthesia induction chamber with 4% Isoflurane (Forane[®], Abbott, Wiesbaden, Germany). After that, the mouse was transferred to the stereotaxic frame (Model 940, David Kopf Instruments, Tujunga, USA). Anesthesia was continuously delivered via a custom-made mask. Isoflurane concentration was set to around 1.5%. The animals were fixed with two ear bars inserted into the external auditory canals and a bite bar to prevent movements.

For the whole duration of the procedure, the mouse was placed on a heating plate (World Precision Instruments, Sarasota, FL, USA) to keep body temperature constant around a desired value of 37.5°C. The head of the animal was shaved with an electric hair trimmer (Aesculap Schermaschinen GmbH, Suhl, Germany), and a local anesthetic of 2% xylocaine (Aspen Germany GmbH, Munich, Germany) was applied to the scalp. To protect the eyes, a 5% dexpanthenol (Bepanthen[®], Bayer Vital GmbH, Leverkusen, Germany) eye cream was applied. Before any incisions were made, the absence of pain reflexes was checked by pinching the animal's paws. A 0.5 cm to 1 cm long incision of the mouse's scalp was performed at midline with scalpel blade and extended to a circular cut with surgical scissors (Fine Science Tools GmbH, Heidelberg, Germany). The edges of the scalp were sealed with surgical glue (VETBOND[™], 3M Deutschland GmbH, Neuss, Germany). The periosteum was scraped off with the scalpel blade and the skull was thoroughly cleaned with sponges (Absorption Triangles, Fine Science Tools GmbH, Heidelberg, Germany) and saline solution (NaCl 0,9% Fresenius, Fresenius Kabi Deutschland GmbH, Bad Homburg, Germany).

To improve the adhesion of the head holder to the skull, small, grid pattern grooves were made with the scalpel blade and then with the dental drill (Ultimate XL-F, NSK Europe GmbH, Eschborn, Germany). An approximately 2.5 mm circular craniectomy above V1 was done manually with a dental drill 2.7 mm posterior of the Bregma and 2.3 mm lateral of the midline (**Figure 7A**). 125 nL of GCaMP6f viral solution was then injected manually using a fine micropipette prepared specially for intracortical injections. After that, a 3.0 mm glass cover (ElectronMicroscopy Sciences, PA, USA) was placed over the craniotomy and sealed with surgical glue. The head holder was

then attached to the skull using UV-Glue (Polytec, PT GmbH, Waldbrunn, Germany) (**Figure 7B**). To minimize the pain, a diluted solution of Buprenorphine (TEMGESIC®, Indivior Europe Ltd., 0.1 mg/kg body weight) was injected subcutaneously before removing the animal from the stereotaxic frame. After the surgery, all animals were observed closely for the first 24 hours and checked on for the following 2 days.

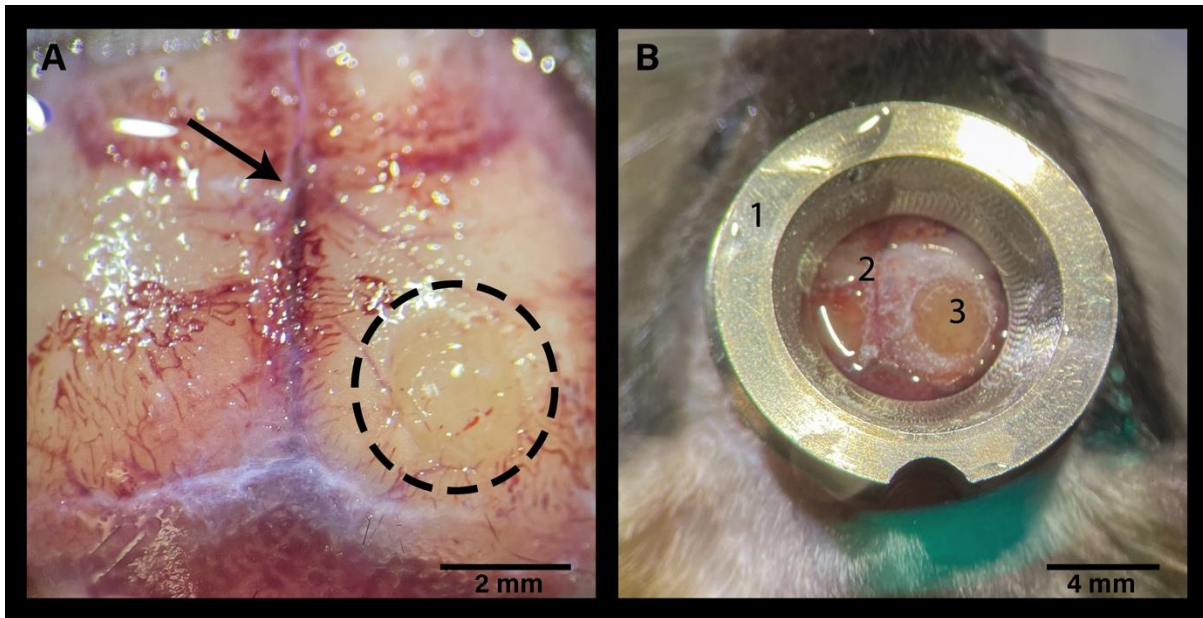


Figure 7: Micro-surgery with craniectomy and head holder implantation.

(A) the exposed skull of the animal after skin and periosteum removal. The center of the craniectomy (black circle) is located 2.7 mm posterior of the Bregma (black arrow) and 2.3 mm lateral of the midline. The craniotomy was done manually with a dental drill. **(B)** The finished implantation of the head holder (1). The head holder is attached to the skull directly via UV-glue (2). The craniotomy is covered with a 3 mm glass cover slip (3).

4.3. Two-photon calcium imaging

In vivo functional calcium imaging was performed for all animals on p51 with a custom-made two-photon microscope (TrimScope II, LaVision Biotec, Bielefeld, Germany) equipped with Ti:Sa laser (Chameleon Ultra II, Coherent, CA, USA) and a resonant scanner. The laser was tuned to 920 nm for the imaging of GCaMP6f. The laser's output was set to 5 - 60% of its maximal power output (3 Watt), depending on the individual SNR of each animal. For signal detection, a high-sensitivity PMT (H7-422-40 LV GaAsP, Hamamatsu Photonics K.K., Shizuoka, Japan) was used. A 20x water-immersion objective (W-Plan-Apochromatic 20x DIC, Carl Zeiss Microscopy LLC., New York, USA) was used to achieve a field of view of 465x465 μm . Images were sampled at a rate of 30.8 Hz and a pixel size of 512x512 pixels. Imaging depth was usually between $200 \pm 50 \mu\text{m}$ below the cortical surface. The frame trigger signal of the microscope, as transistor-transistor logic (TTL) pulses, was sampled using a data acquisition interface (Power 1401-3, Cambridge Electronic Design Limited, Cambridge, England) at 2000 Hz and was later used to sync frame timings with visual stimulation.

4.4. Visual stimulation

For visual stimulation, 10 Trials of static and drifting gratings were generated by a custom written Python script and projected onto Phenosys 270° Virtual Reality system (6 thin-film transistor (TFT) monitors arranged in a hexagonal shape) (Figure 8A). Each trial consisted of 5 s of a uniform grey screen followed by a randomized series of 8 grating orientations, each presented for 10 s (5 s static + 5 s drifting). The orientations ranged from 0° to 315° with a step size of 45°. The order of presentation was logged to a text file. The x and y coordinates and other signals from the VR system were recorded via the same data acquisition interface as the microscope's frame trigger signal. This was later used for synchronizing the frames of the functional calcium imaging to screen projections by aligning the frame trigger signal to the time points of the presentations.

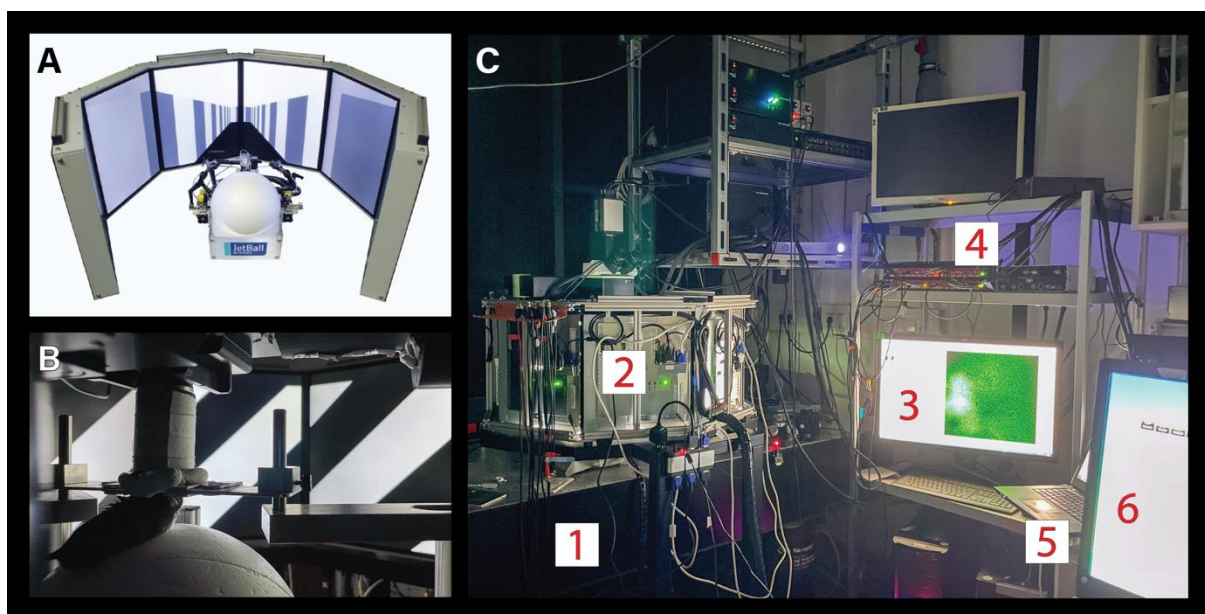


Figure 8: Overview of the imaging setup.

(A) 270° surround monitor system with air-cushioned spherical treadmill (Track Ball) as a part of the Phenosys Virtual Reality system. Image from phenosys.com (B) Wildtype C57BL6 mouse head fixated under the microscope on the trackball and surrounded by the monitors. The objective of the microscope is protected from interferences from the light of the visual stimulation with a tube of black shielding paper and double-sided adhesive to cover any small gaps between the paper and the fixation plate. (C) The overall imaging setup during an experiment. The two-photon microscope is installed on an air-suspended optical table (1) to dampen any vibrations. The surround monitor rack (2) is pushed around the stage and objective of the microscope. Image acquisition is controlled from the microscope's computer (3). The frame-trigger signal of the microscope and other signals from the virtual reality system are recorded via data acquisition interface (CED Box) (4) connected to a laptop (5). The virtual reality system is controlled via an external computer (6).

4.5. Two-photon data analysis

To analyze the images from the calcium imaging, first a mean intensity projection (Figure 9) image was made using ImageJ either by the StaAv plugin or from the first 1000 images of the recording. Segmentation and trace extraction were then done using a custom written MATLAB script. This entailed first manually drawing polygons around potential neuronal somata to define them as ROIs (Figure 10). Then, fluorescence traces were automatically calculated by the mean pixel value of each

ROI over time (Figure 11). The fluorescence traces were then normalized by manually defining a baseline over an activity-free interval for each trace, resulting in the convention of the values to $\Delta f/f$. Binarization was done semi-automatically using a custom procedure file for Igor Pro (waveMetrics). In each $\Delta f/f$ trace, all peaks above 3.8 SD were automatically marked as calcium transients and the onsets and offsets were determined automatically. The results were then reviewed, any false positives were removed, and any mismarked false negatives were annotated. The result is a binary matrix with the height matching the number of cells and a width equal to the number of frames with values of either 1 for activity or 0 for inactivity.

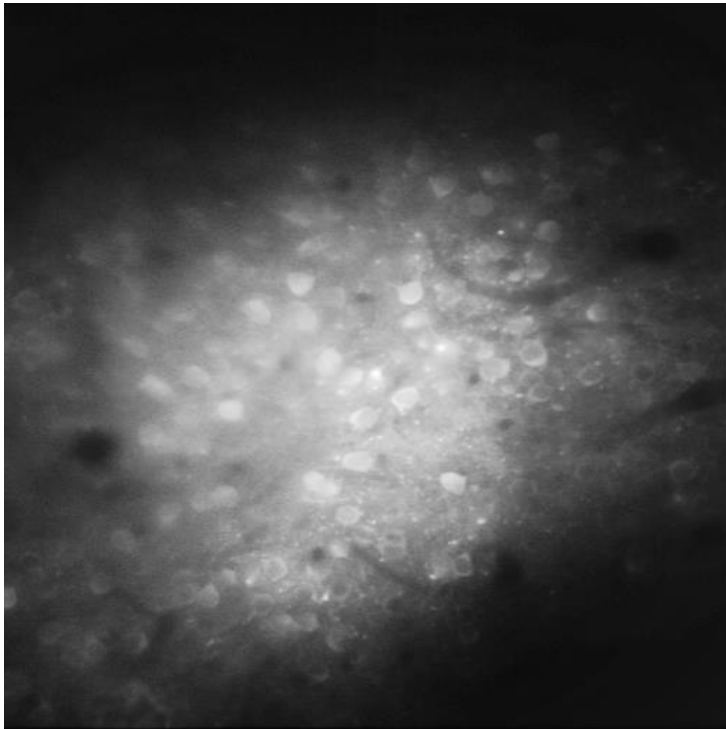


Figure 9: An exemplary average intensity projection.

The projection is used to generate a 2D image from a stack of 3D image data, where time is the 3rd (z) dimension in the image series. To create an average intensity projection, the pixel intensities from each slice in the z-stack are averaged to generate a single 2D image. The projection provides a clearer and more interpretable representation of the overall morphology of the recording plane. The averaging reduces noise from single frames and highlights the cells.

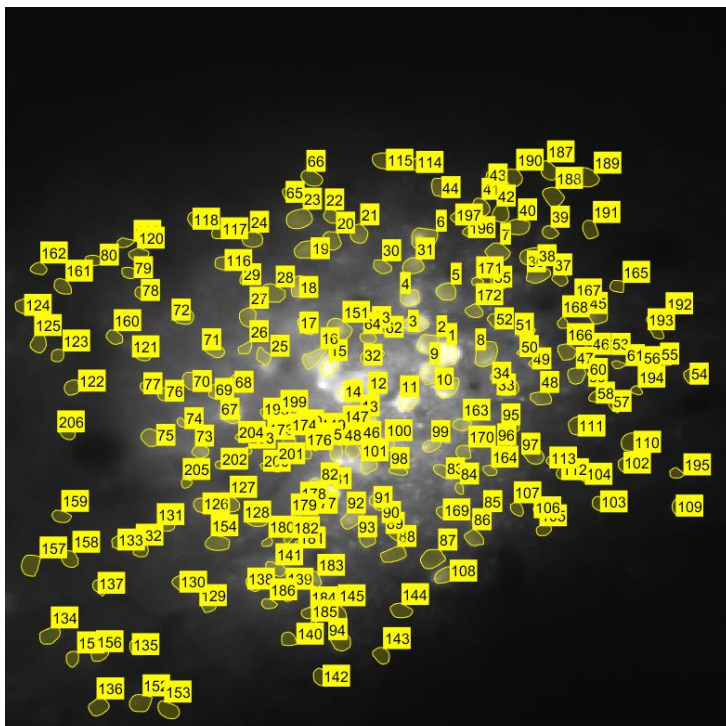


Figure 10: An exemplary manual segmentation of neuronal somata.

Depicted here is the same recording plane as in Figure 9. The goal of segmentation is to identify and outline the boundaries of individual neuronal somata. Here, this is done manually by drawing polygons around potential cells.

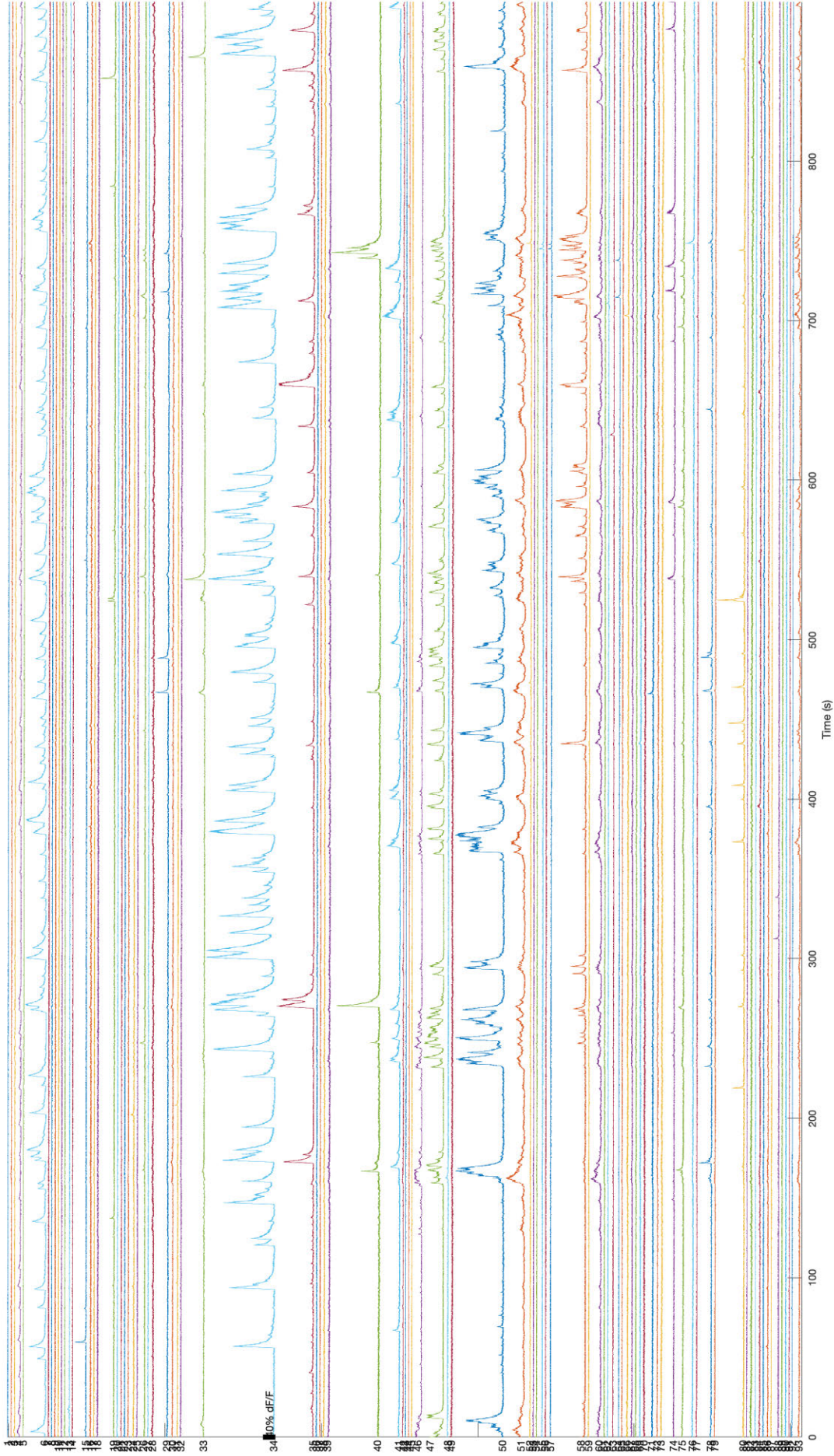


Figure 11: $\Delta f/f$ fluorescence traces extracted from calcium imaging.

After having a set of ROIs over the imaging series, the trace extraction can be automatically calculated from the mean pixel value of each ROI over time. The y-axis scale of this plot was automatically calculated to fit all traces.

4.6. Analysis of visually evoked activity

After the analysis steps described above, we used multiple downstream analyses specific for each objective (Figure 12). For the correlation of activation patterns under visual stimulation, we used cosine similarity as a measure of correlation. The cosine similarity was calculated as the dot product of two vectors:

$$\text{Cos}(x, y) = \frac{x * y}{\|x\| * \|y\|}$$

The Orientation Selectivity Index (OSI) (Niell and Stryker, 2008) was calculated by first determining the orientation, at which the highest response of the neuron was observed (R_{pref}). Then the response of the cell evoked by the orthogonal orientation was calculated (R_{ortho}). OSI was then the result of the multiplication of the two, divided by the sum of the two.

$$\text{OSI} = \frac{R_{pref} \times R_{ortho}}{R_{pref} + R_{ortho}}$$

The Circular Variance (CV) (Ringach et al., 2002) was calculated as the variance of the cell's response to all orientations and does not require the definition of a preferred orientation:

$$\text{CV} = 1 - \left| \frac{\sum_k r_k e^{i2\theta_k}}{\sum_k r_k} \right|$$

Where r_k is the cell's response to a given orientation and θ_k is the angle of the grating in radians.

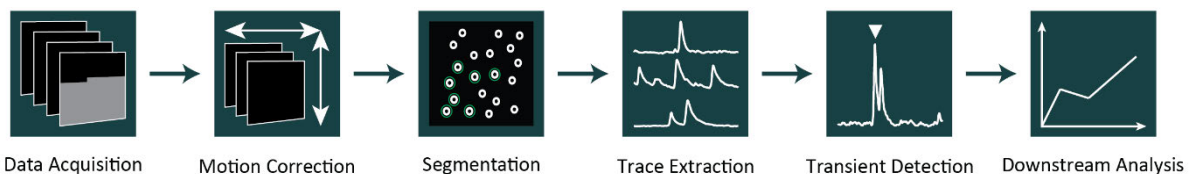


Figure 12: Schematic illustration of the analysis pipeline for this study.

This pipeline follows the first few preprocessing steps as described in the introduction. Motion correction was done with the ImageJ plugin MoCo, when necessary. The identification of cells was carried on manually. After the trace extraction, a semi-automatic approach of thresholding and manual corrections was done to binarize the traces. Finally, each downstream analysis was done to answer a specific research question.

4.7. Statistical tests

Recordings with no cell activity were excluded from the study. Unless otherwise stated, all analyses for the spontaneous activity were done on 10 imaging regions from 8 animals (436 active cells) in the WT group and 10 regions from 6 animals (384 active cells) in the NMDAR-Ab group. Silent cells were excluded from the analysis. Analysis of visually evoked activity was done on 6 regions from 6 animals (277 active cells) in the WT group, and 6 regions from 4 animals (255 active cells) in the NMDAR-Ab group.

Statistical analysis was done with GraphPad Prism. All datasets were first tested for normal distribution, in the case where normal distribution was rejected, a non-parametric test was done. For analysis of variance, the Levene's test was used. All statistical tests and exact p-values are noted under the corresponding figures. Box-and-whisker plots indicate the median value (center line), the 25–75th percentiles (box) and the 10–90th percentiles (whiskers). All other graphs represent mean \pm standard error of the mean (SEM) unless otherwise stated. The significance level was set at $p < 0.05$.

4.8. Benchmarking the analysis pipeline

Imaging data was acquired from the microscope to a windows 7 machine using a custom made I/O interface and protocols (LaVision Biotec, Bielefeld, Germany). The computer was equipped with an Intel Core i7-3770k processor operating at a clock speed of 3.4 GHz. It had 32GB of DDR3 RAM, a 1TB SATA SSD and a 2TB SATA HDD for storage. Imaging data was directly written to the SSD and subsequently transferred to an external HDD (WD My PassPort), attached to a USB 2.0 port on the front. The data analysis was then conducted on a workstation with the following specifications:

Operating System: Windows 10
Processor: Intel Core i7-4770k 3.8GHz
RAM: 32GB DDR4
Storage: 120GB SATA SSD (OS), 4TB SATA HDD (Data)
Graphics Card: NVIDIA GeForce GTX 1070

The necessary time needed to finish each analysis step was either measured externally using a stopwatch or directly in the program, if it had a function to measure the execution time, e.g., using “tic” and “toc” functions for MATLAB scripts and “time.process_time()” for python scripts.

4.9. Software development

In this work, we present three separate software packages. First, we developed the StaAv Tool plugin to address the limitations of conventional intensity projections created from the initial n frames from a given image series. The plugin was designed for ImageJ and was written in Java, leveraging the capabilities of the ImageJ API for image processing and analysis (Rasband, 1997-2023). StaAv Tool is publicly available on the Stroh Lab GitHub page: <https://github.com/Strohlab/StaAv-Tool>.

The trace extraction in Python for ViNe-Seg is based on a simple extraction algorithm similar to our established MATLAB analysis script. This algorithm runs in two steps. First, it converts the shape and location of each ROI into a binary mask. Then, a loop over all images uses the binary mask to extract the mean pixel intensity of each ROI. The results are then returned as a matrix with a size of $n \text{ ROIs} \times n \text{ Frames}$. For a faster processing time, we utilized Python's native multiprocessing package. ViNe-Seg is publicly available, for install instructions see this GitHub page: <https://github.com/NiRuff/ViNe-Seg>.

Lastly, we tested Mask RCNN for frame-by-frame segmentation of calcium imaging datasets. We used the standard architecture of Mask RCNN as described in He et al.

(2017), only modifying the head layers for 16-bit 1-channel images with a size of 512x512 pixels. We utilized TensorFlow for the full implementation and training of the model (Abadi et al., 2016). We first trained only the head layers on synthetic datasets for 5 epochs with 1000 steps each and at a learning rate of 0.002. We then trained the whole model for 10 epochs with 1000 steps each and a learning rate of 0.001. Finally, we fine-tuned the model by training it on real-world calcium imaging recordings from this study. For this, we trained the whole model for 5 epochs with 1000 steps and a learning rate of 0.0002. All datasets were carefully curated and split into distinct training and validation sets to ensure a valid assessment of the model's performance. During training, the loss function was closely monitored on both the training and validation datasets. The behaviors of the loss functions on both datasets were consistent, showing steady decreases without any significant divergences, reassuring the absence of overfitting effects. A detailed benchmark of the model's capabilities was not performed, due to the lack of datasets with single frame annotations. Because of the noisy nature of single frames of calcium recordings, cells' visibility might not be as clear in single frames as in an intensity projection. The use of annotations made on intensity projections for benchmarking the model's performance on single frames may deliver inaccurate results. This model and its UI are available upon request.

5. Results

5.1. Improvements in data analysis and new software developments

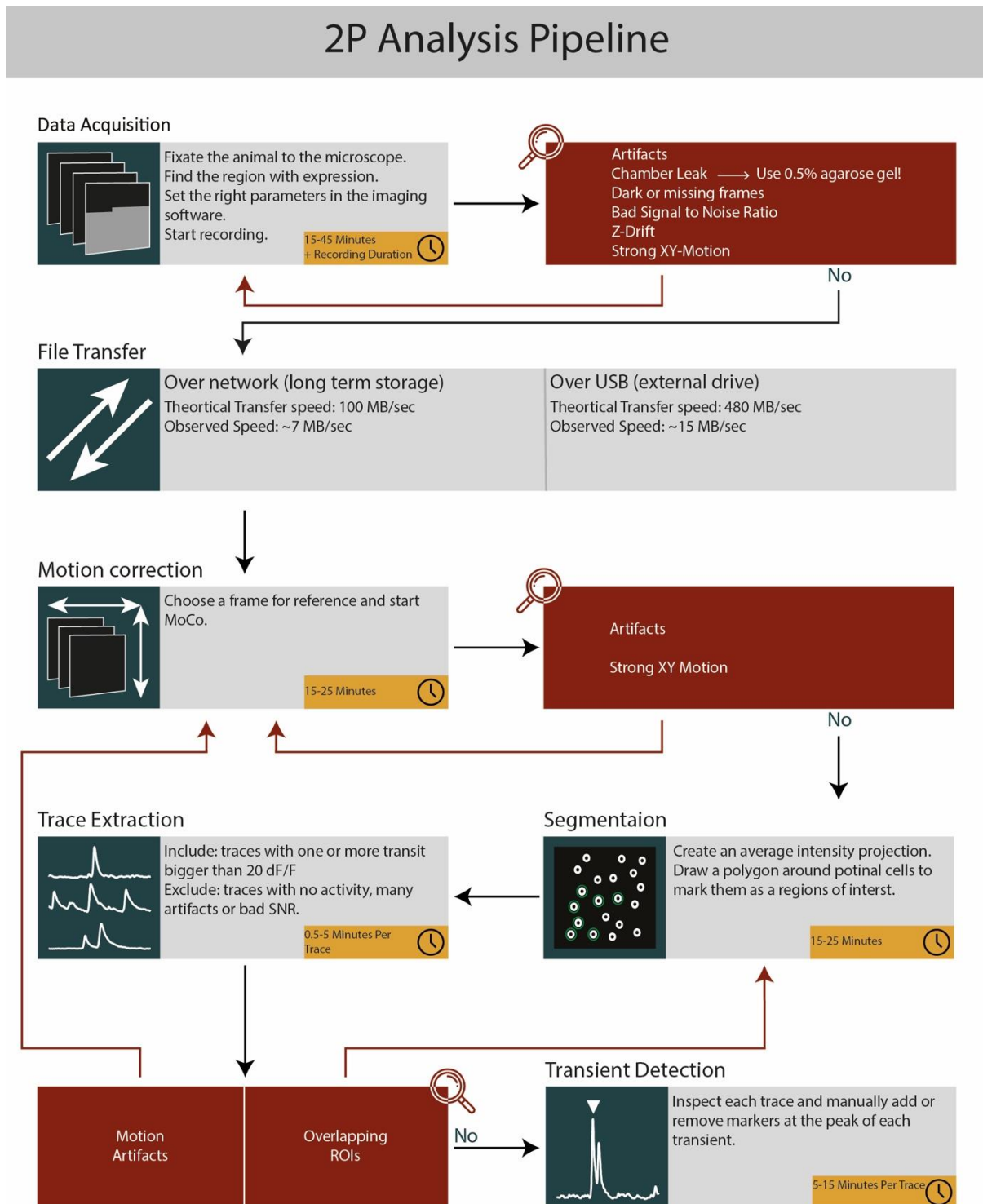


Figure 13: Proposed quality control steps for an efficient calcium imaging analysis pipeline.

Each grey box represents a step in the analysis pipeline. The yellow boxes with the clock symbol indicate the average time necessary to complete each step. The red boxes show a proposed quality control step. If no issues were found during the quality control, the pipeline is followed to the next step (black arrows). Otherwise, the previous step should be redone to eliminate the issues (red arrows).

5.1.1. Data analysis pipeline and quality control measures

To improve the analysis pipeline, first, we need to closely examine the data analysis pipeline that was followed for this study, detailing the individual steps, the time taken for each step, and the quality control measures that could be incorporated at various stages (Figure 13). The study starts with the fixation of the animal under the microscope, starting up the microscope and configuring the acquisition software. This step is usually not time consuming since the animals are previously habituated to the microscope and the acquisition software requires only a few parameters to be changed before starting the acquisition. During and after finishing the recording, it is important to inspect the acquired data for any defects that may make the recording unusable. Recording issues, such as missing frames, very bad signal-to-noise ratio, or very strong motion artifacts, cannot be corrected post-hoc and will require the recording to be redone.

The image series needs to be transferred over to a different workstation for analysis. The data transfer could be done over the local network or via an external disk drive. Both methods of transfer showed lower transfer speeds compared to the maximum theoretical speeds, which might be due to the data format of the image series. After the transfer, the analysis can begin with the first step of motion correction. This step could be skipped if the image series shows no motion artifacts. We used MoCo, a plugin for ImageJ (Dubbs et al., 2016), for this step. The time needed for this step depends on the number of images in the series. On our workstation, it took around 15-20 minutes for each image series consisting of 27720 frames. After the motion correction, the data needs to be reevaluated to make sure that no motion artifacts or any new artifacts presented by the motion correction are present. If necessary, this step can be repeated multiple times.

Next, we need to transform the image series into activity traces. For this, we first need to define visible neurons as ROIs, a step that could take around 15-25 minutes depending on the number of neurons and the SNR of the recording. Then, the MATLAB script will go through the recording frame by frame and average the intensity values of the pixels that fall inside each ROI. This automatic step takes around 10-15 minutes, also depending on the length of the recording and the number of ROIs. After the script finishes processing, the traces are displayed for the user to define an activity-free interval to use as a baseline for the $\Delta f/f$ calculation. It's also important here to examine the resulting activity traces for issues and redo this step if any are present.

The activity traces can be loaded into Igor Pro for the final step of binarization. Our custom procedure script for Igor runs in distinct steps. Here, a semi-automatic approach is used to correctly classify transients as such and generate a binary matrix of the activity. This step is the most time-consuming step of the analysis pipeline. Depending on the number of cells in the recording, their firing frequency, and the overall signal quality of the recording, it could take hours to finish.

5.1.2. StaAv Tool: a new plugin for improved intensity projections

Creating an average intensity projection from the first n images of the recording might result in the omission of cells that are only active after those frames. The alternative, creating the intensity projection from all frames, is very computationally intensive. Here, we introduce an alternative method. We developed a new ImageJ plugin, "Stack Averaging Tool" or "StaAv Tool", that can create an intensity projection from selected frames (Figure 14). This Plugin can be used by either manually selecting the frames

where cell activity is visible, automatically marking a frame for every half of the calcium indicator decay time or both methods together.

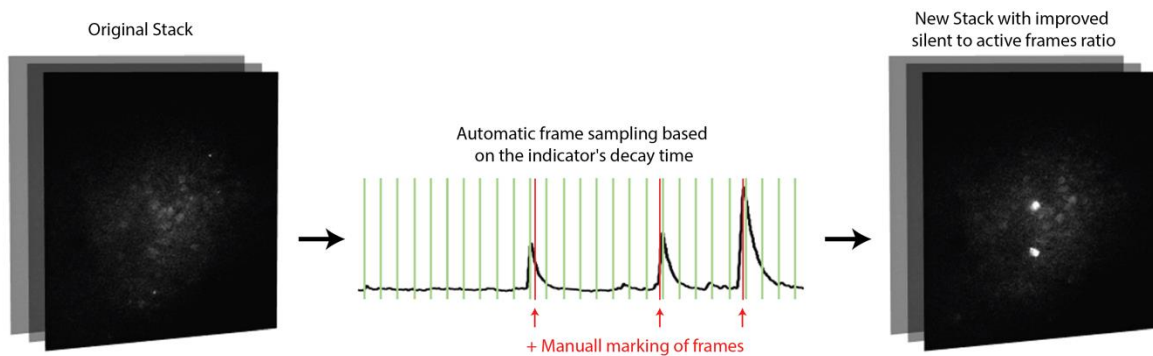


Figure 14: StaAv Tool for enhancing cells' visibility in average intensity projections.

By strategically sampling from the image stack, based on the decay time of the calcium indicator, it's possible to create an intensity projection from the entire recording length. This helps in cases where some cells are not active during the initial few hundred frames, which are typically used for intensity projections. Furthermore, frames can be selectively marked and incorporated manually. The result is a refined image stack spanning the entire recording duration and entailing a greater number of frames capturing neuronal activity.

The plugin's architecture can be broken down to three main components that facilitate user interaction, frame selection, and stack generation. The plugin starts by declaring necessary variables and setting them for default values, in addition to adding its icon to the tool bar with the function "run".

```
public class StaAv_Tool extends PlugInTool implements ImageListener, KeyListener{

    ImagePlus monitored_stack;
    boolean listeners_active = false;
    List<Integer> slices = new ArrayList<Integer> ();
    int current_frame;
    ImageWindow win;
    ImageCanvas canvas;
    double fpm = 100; // number of frames per single mark
    boolean get_background = true;
    double freq = 30.8; // imaging frequency in Hz
    double decay = 1100; // decay time in ms
    double fprm = 1;

    public void run(String arg) {
        Toolbar.addPlugInTool(this);
    }
}
```

Code Block 1: Frist few lines of the StaAv Tool code.

Once the plugin is activated, by double clicking on its icon, a dialog box will appear to change the key parameters and choose the original images stack (Figure 15). The function "showOptionsDialog()" handles the display and interaction with the dialog box.

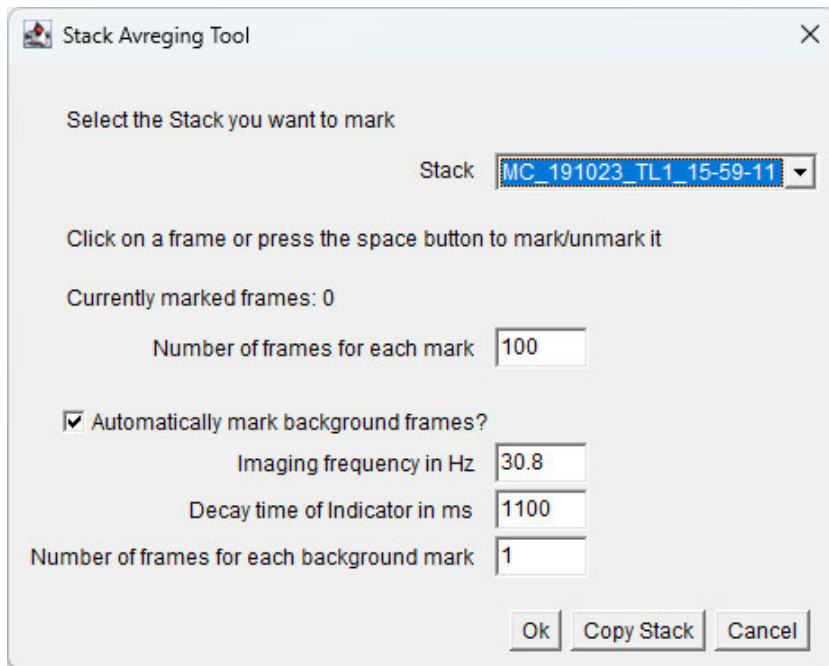


Figure 15: Settings dialog box of StaAv Tool.

By double clicking on the plugin's icon, this dialog box can be shown. Here, the user can choose the original image stack from a list of currently opened stacks. The default parameters of the plugin can be also changed to fit any imaging conditions. The automatic marking of frames can be enabled or disabled by simply ticking on or off the checkbox "Automatically mark background frames".

```

public void showOptionsDialog() {
    // Get a list of opened images and stacks
    String w_names[] = new String[(WindowManager.getWindowCount()+1)];
    [...]

    // Setup the dialog box
    GenericDialog gd = new GenericDialog("Stack Averaging Tool");
    gd.enableYesNoCancel("Ok", "Get Stack");
    [...]

    // Display the dialog box
    gd.showDialog();

    // If canceled, change nothing and return
    if (gd.wasCanceled()) return;

    // If not canceled, save the new parameters
    get_background = gd.getNextBoolean();
    fpm = gd.getNextNumber();
    freq = gd.getNextNumber();
    decay = gd.getNextNumber();
    fprm = gd.getNextNumber();
    String stack_name = gd.getNextChoice();

    // If 'ok' was pressed, start listening for keyboard presses
    if (gd.wasOKed()){
        [...]
        monitored_stack = WindowManager.getImage(stack_name);
        registerListeners();
    }else{
        // 'get' stack was pressed, start copying frames to new stack
        [...]
        getNewStack();
    }
}

```

Code Block 2: showOptionsDialog function for handling the display and interaction of the plugin's main dialog box.

For frame selection, the plugin uses event listeners that monitor the user's input. It can set a frame as marked if it was clicked on with the mouse or the space button was pressed. Marked frames will have the word "marked" overlaid on them in the top right corner. If the "Automatically mark background frames" was ticked on in the dialog box, the plugin will automatically mark frames based on the decay time of the calcium indicator and the imaging frequency with the following formula:

$$\text{Frame Interval} = \frac{\text{Imaging frequency in Hz}}{1000} \times \frac{\text{Decay time of Indicator in ms}}{2}$$

As a Java code:

```
frame_interval = (int) Math.round((freq/1000)*(decay/2));
```

```
// Register listeners for key presses and mouse events
private void registerListeners(){
    [...]
}

// Handle events when a frame is clicked on by the mouse
public void mousePressed(ImagePlus imp, MouseEvent e) {
    markImage(imp);
}

// Handle events when the mouse pointer is moved, update the status bar
public void mouseMoved(ImagePlus imp, MouseEvent e){
    [...]
}

// Handle events when a key was pressed, check if it was space and mark the frame
public void keyPressed(KeyEvent e) {
    [...]
}

// Add the frame to the list of marked frames and draw an overlay on it
private void markImage(ImagePlus imp) {
    [...]
}
```

Code Block 3: Functions for handling listening to mouse and keyboard inputs and marking of frames.

Finally, the function "getNewStack()" handles the creation of a new empty virtual stack and copying the marked frames over to it. This function is evoked by clicking on the plugin's icon in the toolbar to reveal the dialog box again and clicking on the "Copy Stack" button. The newly created image stack with only marked frames will open and in addition, a table containing the indexes of the marked frames from the original will appear. The intensity projection can be created from the newly created stack by going to "image -> stacks -> Z Project".

```

private void getNewStack(){
    // Display a confirmation message with the number of frames being copied
    [...]

    // Update the marked frames array
    IJ.showStatus("Indexing Images");
    [...]

    // Create a new empty stack and copy marked frames into it
    IJ.showStatus("Copying images");
    ImageStack fullStack = monitored_stack.getImageStack();
    int height = WindowManager.getCurrentImage().getHeight();
    int width = WindowManager.getCurrentImage().getWidth();
    ImageStack newStack = new ImageStack(width,height);
    [...]

    // Display the new stack
    ImagePlus newImages = new ImagePlus("New Stack", newStack);
    StackWindow window = new StackWindow(newImages);
    rt.show("Results");
    IJ.showStatus("Done!");

    // Clean up
    listeners_active = false;
    deregisterListeners();
    slices.clear();
}

```

Code Block 4: getNewStack function for handling the creation of the new image stack.

5.1.3. Faster, integrated, and multithreaded analysis in Python for ViNe-Seg

ViNe-Seg, our Deep-Learning assisted analysis program, is designed with a user-friendly graphical interface to facilitate easy semi-automatic segmentation and fast and complete analysis of calcium imaging datasets. One of the fundamental aspects of ViNe-Seg is offering the user the most flexibility in choosing the right segmentation models for their data and in incorporating further analysis steps in the same GUI. In this subsection, we present our contributions towards the development of ViNe-Seg. These improvements were essential to ensure seamless integration of the different analysis steps, enabling the program to perform its designed purpose.

To create a new analysis pipeline that could easily be integrated with other tools, we needed a fast and reliable trace extraction algorithm. For this, we used our established MATLAB algorithm and changed it from a single threaded process to a multithreaded one (**Figure 16**). Multithreading allows a significant reduction in processing time for such algorithms. The new algorithm runs mainly in two steps. First, the location data of the ROIs from the segmentation algorithm needs to be converted to binary masks. Binary masks are basically a matrix with a size of the original image and have the value of 0 for all the pixels outside of the ROI and 1 for the pixels inside. Multiplying this mask with the original image allows for quick isolation of the pixel values of only the pixels inside the ROI. For this step, we can rely on the function “shape_to_mask” that is already built in the ViNe-Seg base code, originally adapted from labelMe.

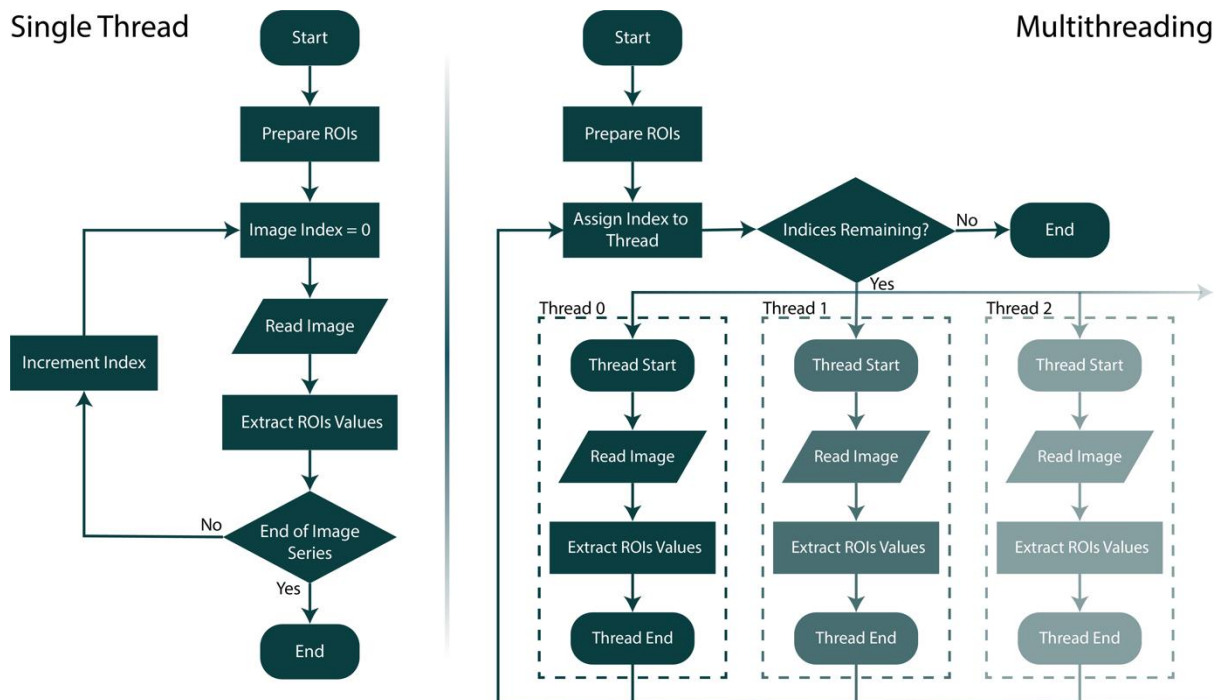


Figure 16: Multithreading can reduce trace extraction time.

During trace extraction, the reading of each single frame can be the most time-consuming step. By moving this step into multiple processes (threads) that can run in parallel, computation time can be reduced by a factor roughly proportional to the number of threads. On modern computer hardware, the number of threads is usually between 12 to 32 threads, so we should expect faster execution by a similar factor.

```
# Initialize an empty list to store binary masks for each Region of Interest (ROI)
masks = []

# Loop through each ROI in the 'data' dictionary
for i in range(0, len(data[rois])):
    # Extract the points defining the current ROI and convert it to a binary mask
    roimask = shape_to_mask((data['imageHeight'], data['imageWidth']),
                            data[rois][i]['points'],
                            shape_type=None,
                            line_width=1, point_size=1)

    # Add the generated mask to the 'masks' list
    masks.append(roimask)
```

Code Block 5: ROI to mask conversion in ViNe-Seg

The second part of the algorithm runs in each thread separately. Here, we read the image, isolate the pixel value of each ROI, and save this value in an array. The resulting array represents a vertical slice of the final matrix containing all ROIs. The final matrix then has the size $n \text{ ROIs} \times n \text{ Frames}$. The creation of the separate threads is handled via Python’s native multiprocessing package. Specifically, we employ the “multiprocessing.Pool.Starmap” function to generate the threads and pass specific indices and a copy of the ROI masks for execution. This function preserves the original order of the frames during processing, so the final traces do not get altered in any form.

```

def tracesForImage(imagePath, masks):
    """
    Calculate the intensity traces for each Region of Interest (ROI) in the given image.

    Args:
        imagePath (str): Path to the input image.
        masks (list): List of binary masks representing ROIs.

    Returns:
        np.array: Array containing intensity traces for each ROI in the input image.
    """

    # Initialize an array to store intensity values for each ROI
    trace = np.zeros(len(masks))

    # Read the input image from the specified imagePath
    im = image2array(imagePath)

    # Iterate over each ROI mask and calculate its intensity value
    for x in range(0, len(masks)):
        # Invert the mask to get the pixels inside the ROI
        roimask = np.invert(masks[x])

        # Apply the mask to the image and calculate mean intensity value
        a = np.ma.array(im, mask=roimask)
        trace[x] = a.mean()

    # Return the array representing intensity traces for each ROI
    return trace

# Create a pool of worker processes for parallel computation
with Pool() as pool:
    # Using starmap to apply tracesForImage function to each image
    # zip(imagesArray, repeat(masks, len(imagesArray))) combines each image with the
    # same masks for processing
    traces = pool.starmap(tracesForImage, zip(imagesArray, repeat(masks,
        len(imagesArray))))

```

Code Block 6: Using the multiprocessing module to parallelize the calculation of intensity traces for multiple images and masks.

We also developed a model manager for ViNe-Seg to enable easy user download and management of available segmentation models (**Figure 17**). This functions in a very simple way. When the user installs ViNe-Seg for the first time, the model manager downloads the default model and creates a basic manifest file. The user can then at any time access the model manager from the segmentation menu. When the model manager is evoked, it connects to the online servers to check which models are available and compares them to the entries in the local manifest file. Therefore, the model manager can display the status of models and enable the user to install and uninstall any model very easily. New models can be quickly integrated by simply uploading the model to the server and adding its description to the online manifest.

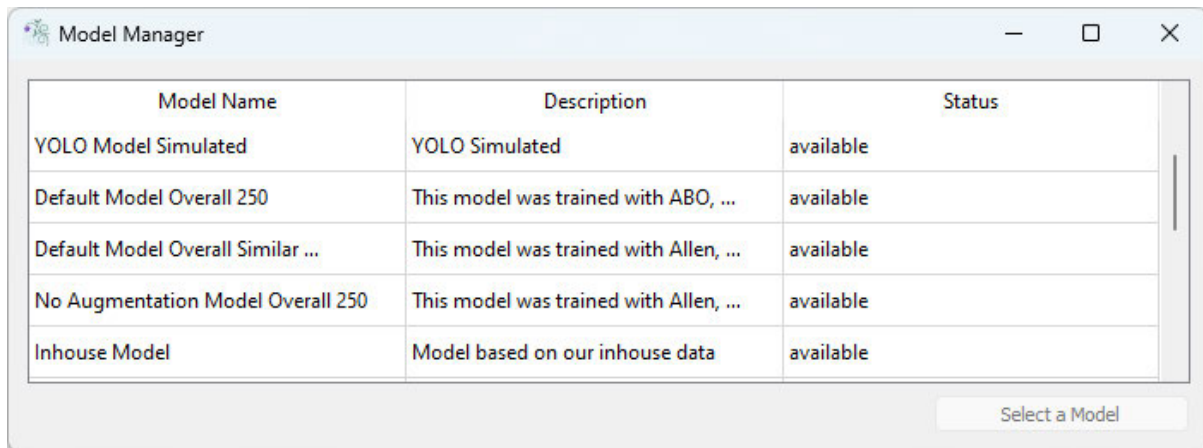


Figure 17: Model Manager in ViNe-Seg for intuitive overview and management of available segmentation models.

The model manager checks an online manifest to find available models and compares the entries to a local manifest file. It can then allow the user with one button click to install or uninstall any model.

5.1.4. Mask RCNN can detect both cells and vessels in single frames of functional calcium recordings

In addition to ViNe-Seg, we wanted to experiment with different machine learning models and test their capability in segmenting calcium imaging data for a real-time analysis pipeline. Here, we present the remarkable performance of Mask RCNN in detecting both cells and vessels within functional calcium recordings. Mask RCNN is a model created by He et al. (2017) and was designed to perform instance-level segmentation in contrast to most publicly available models that focus on object detection. We trained the model on a dataset that encompassed rudimentary simulations (**Figure 18A**) and then fine-tuned it with in-house datasets. These simulations intentionally included noise as the background to mimic real-world conditions, with the average pixel intensity remaining within real-world calcium recordings. Cells were overlaid over the noisy background as round objects that exhibit intensities above the noise level, while vessels were crafted to remain beneath this noise level. This deliberate construction of the training dataset aimed to challenge the model's ability to differentiate between subtle signal variations and noise, closely simulating the intricacies of actual calcium imaging recordings.

The outcomes of our experiments revealed the robustness and adaptability of the Mask RCNN architecture. The model successfully learned to distinguish between cellular and vascular elements in single frames (**Figure 18B**), despite the presence of noise that often accompanies calcium imaging data. We complimented the Mask RCNN model with an intuitive GUI to make usage easier. The GUI features a timelapse analysis mode (**Figure 19**), which is designed to enable the user to inspect the segmentation results as well as the quality of calcium traces. In addition, it can display any metadata found associated with the recording. The user can see both an average intensity projection with all detected ROIs, and a single frame view with only the currently selected ROI. The user can scroll in the recording to any timepoint to see the intensity change of the selected ROI and check for artifacts.

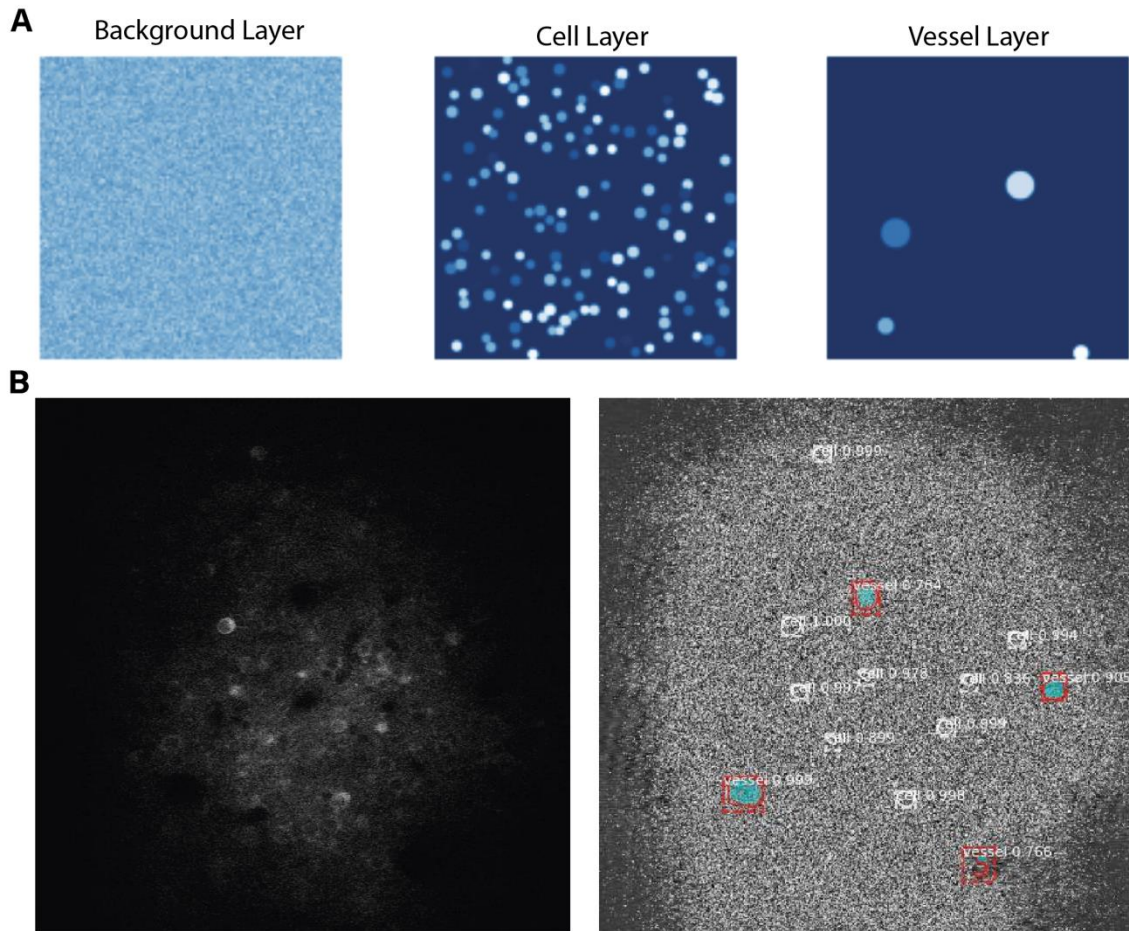


Figure 18: Mask RCNN can detect both neurons and vessels in low SNR single frames.

(A) Synthetic data used to simulate noisy single frames of calcium recordings. Each 16-bit frame is composed of a random noise layer that has pixel values between 100 and 1000. A random number of neurons is then overlaid on top of the background layer. Neurons have a random pixel intensity of 1-120 above noise with a small subset with an increased intensity up to 12000 to simulate active neurons. Vessels are subtracted from the background with a random negative intensity of 50-100% of the background. (B) Results from running Mask RCNN on a single frame from a real calcium recording. The original frame is on the left. On the right is the normalized frame with the output of the model. White represents detected cells, red represents detected vessels. Of note, the dark circle in the middle of the original frame is most likely the canal from GCaMP6f viral solution injection, which explains why it's not detected as a vessel by the model.

The second interface is for live analysis (Figure 20), which runs the Mask RCNN model on newly acquired frames directly after they are written on disk. This mode is designed to give the user a general estimation of the quality of the recording in real-time. Before running this mode, the user has to set a few key parameters, such as the folder location where the images will be saved and the image extension. The model is then run on newly acquired images on a frame-by-frame basis. The user can choose if the segmentation results, i.e., ROIs, from previous frames are preserved and new ROIs are simply added to them, or if they should be degraded and the results for each frame are completely new. The interface utilizes a heatmap for visualizing the segmentation results from the recording and highlight motion artifacts. The user can also adjust recording parameters in real-time to see how to optimize them for achieving highest SNR and best segmentation results.

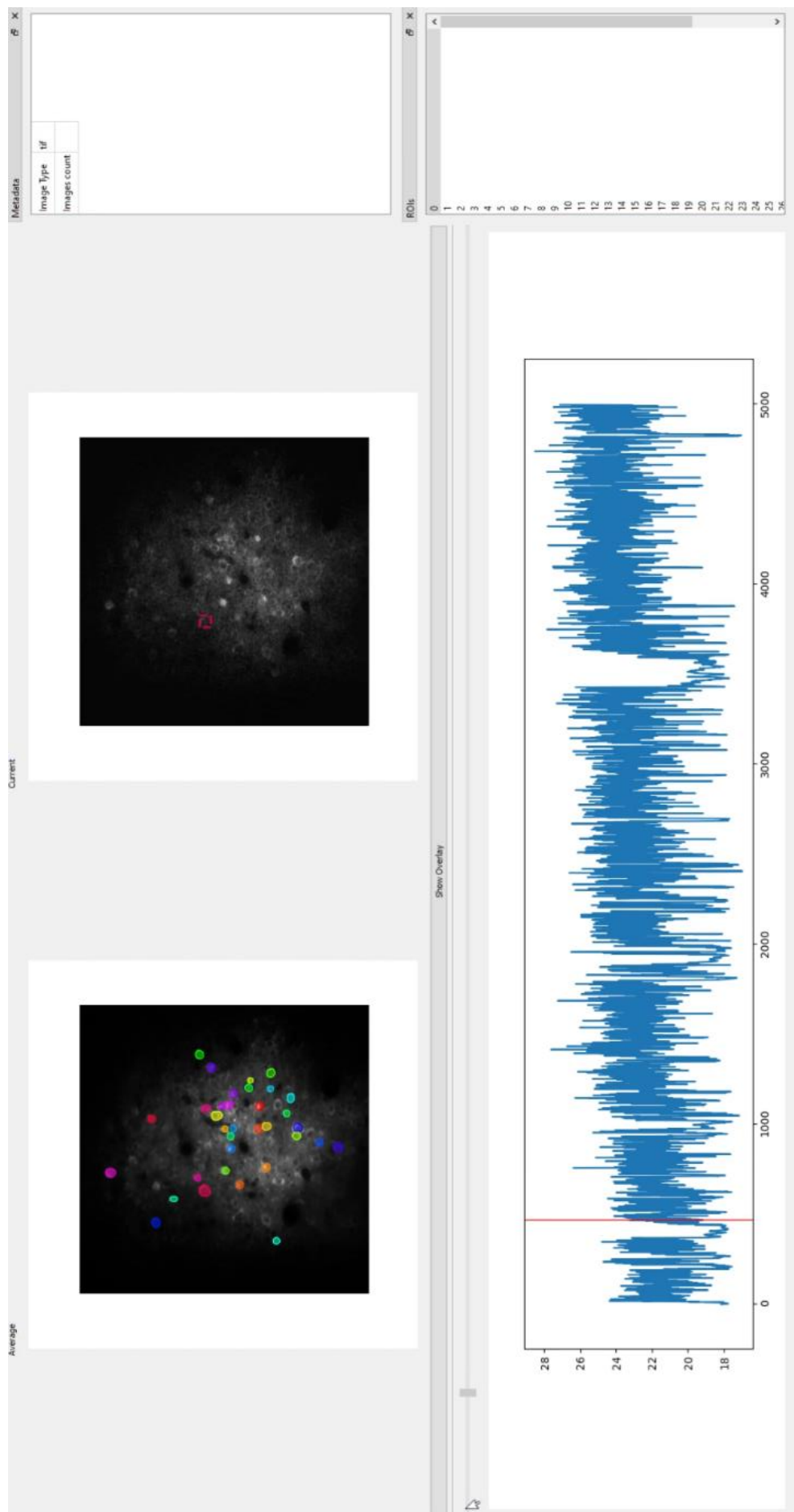


Figure 19: Timelapse mode UI for inspecting multiple aspects of the analysis at once.

This mode shows the user both the overall segmentation results overlaid on an average intensity projection (left) as well as the currently selected ROI within a single frame view (right). All ROIs are listed in the bottom right panel. The calcium trace of the selected ROI is displayed in the bottom panel. The frame for the "current" view can be changed by sliding the red indicator over the calcium trace. This allows the user to inspect the overall segmentation as well as the traces extracted from each ROI. Any metadata found in the recording file is displayed in the top right panel.

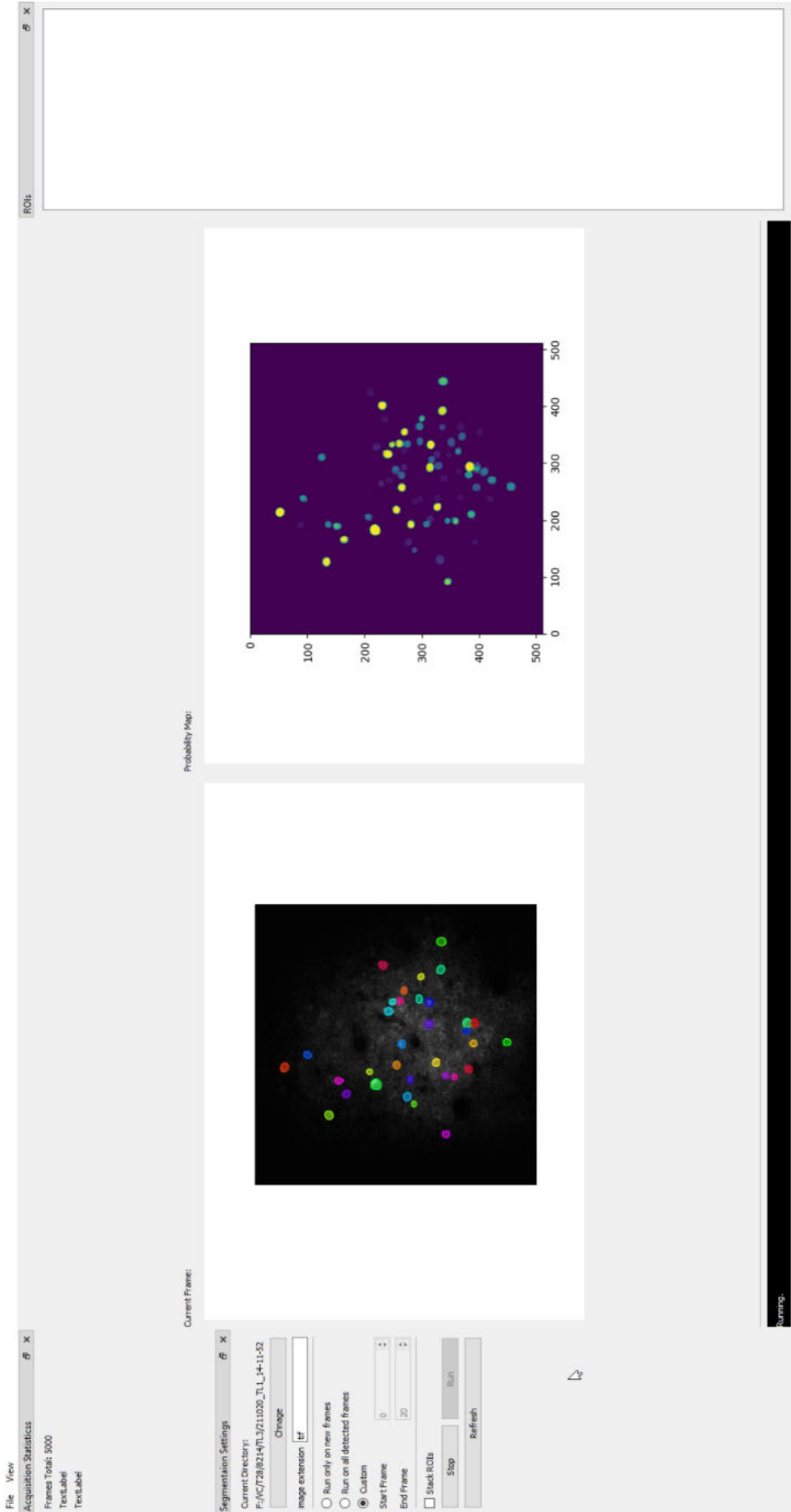


Figure 20: Live mode UI gives an indication of the quality of the recording in real-time.

Before starting the real-time frame-by-frame segmentation, the user needs to enter key recording parameters in the left panel. While running, newly acquired frames are queued for segmentation as soon as they are written to disk. This mode shows the user the most recently acquired frame on the left side with the detected ROIs as an overlay. On the right side, the user can see a probability map of the segmentation which reflects the confidence of the model for each ROI. This heatmap view is also useful for visualizing motion artefacts, as the shape of the ROIs can become blurry in the direction of motion.

5.2. Examining microcircuit changes in Anti-NMDA receptor encephalitis

5.2.1. Awake two-photon calcium imaging of excitatory microcircuits in layers II/III of mouse primary visual cortex.

To study the long-term effects of maternofetal transfer of anti-NMDAR antibodies on neuronal microcircuit dynamics of mouse primary visual cortex (V1), we injected pregnant C57BL/6 mice with 300 μ L of NMDAR-Ab solution on gestational day E13.5 and again on day E17.5 (**Figure 21A**). On postnatal day 24, we stereotactically injected a viral solution encoding for GCaMP6f, targeting layer II/III of V1, alongside with the implantation of metal head holder and chronic window for awake imaging. GCaMP6f-expression was controlled by the CaMKII-promoter targeting only excitatory neurons. In early adulthood (P51) we conducted two-photon imaging in layer II/III of V1 of awake behaving mice (**Figure 21B**). To test whether these NMDAR antibodies already had early structural effects on the microcircuitry, we examined neuronal densities of V1. We did not find a significant difference in both, overall cell densities (**Figure 21C**), and densities of spontaneously active cells (**Figure 21D**) comparing mice exposed to anti-NMDAR antibodies and wildtype mice. This indicates that morphologically, the network is still intact, devoid of apparent cell loss.

5.2.2. NMDAR antibody exposure leads to a decrease in spontaneous firing rates and to a bursty firing profile of V1 neurons.

Next, we probed the functional architecture of ongoing, spontaneous activity, in adult mice exposed to NMDAR antibodies more than four weeks earlier. Conforming the morphological findings, within a field of view, we could record from a similar number of neurons (**Figure 21E**). Moreover, the percentage of cells exhibiting spontaneous activity, i.e., functional calcium transient, did not differ significantly between NMDAR-Ab group and healthy controls (**Figure 21F**). Notably, in the NMDAR-Ab group, we found a reduced mean frequency of spontaneous Ca²⁺ transients (**Figure 22A**). Splitting up the activity levels into 11 activity bins in a cumulative probability graph, a rather homogenous shift towards lower activity bins became apparent in NMDAR-Ab exposed animals (**Figure 22B**). This indicates a rather microcircuit-wide reduction in activity, in both high and low active neurons. Moreover, we noticed that highly active cells in animals exposed to anti-NMDAR antibodies displayed a unique firing pattern, characterized by short bursts of Ca²⁺ transients (**Figure 22C**), while the activity of wildtype mice was more evenly distributed in time. Indeed, while the mean of the inter-event-intervals is not significantly different between groups, the variance is significantly higher in the NMDAR-Ab group (**Figure 22D**), reflecting a distinct firing pattern. Both, the overall reduction in activity, and the new temporal pattern of activity suggest a stable new setpoint of the functional microarchitecture in cortical circuits upon early NMDAR-Ab exposure.

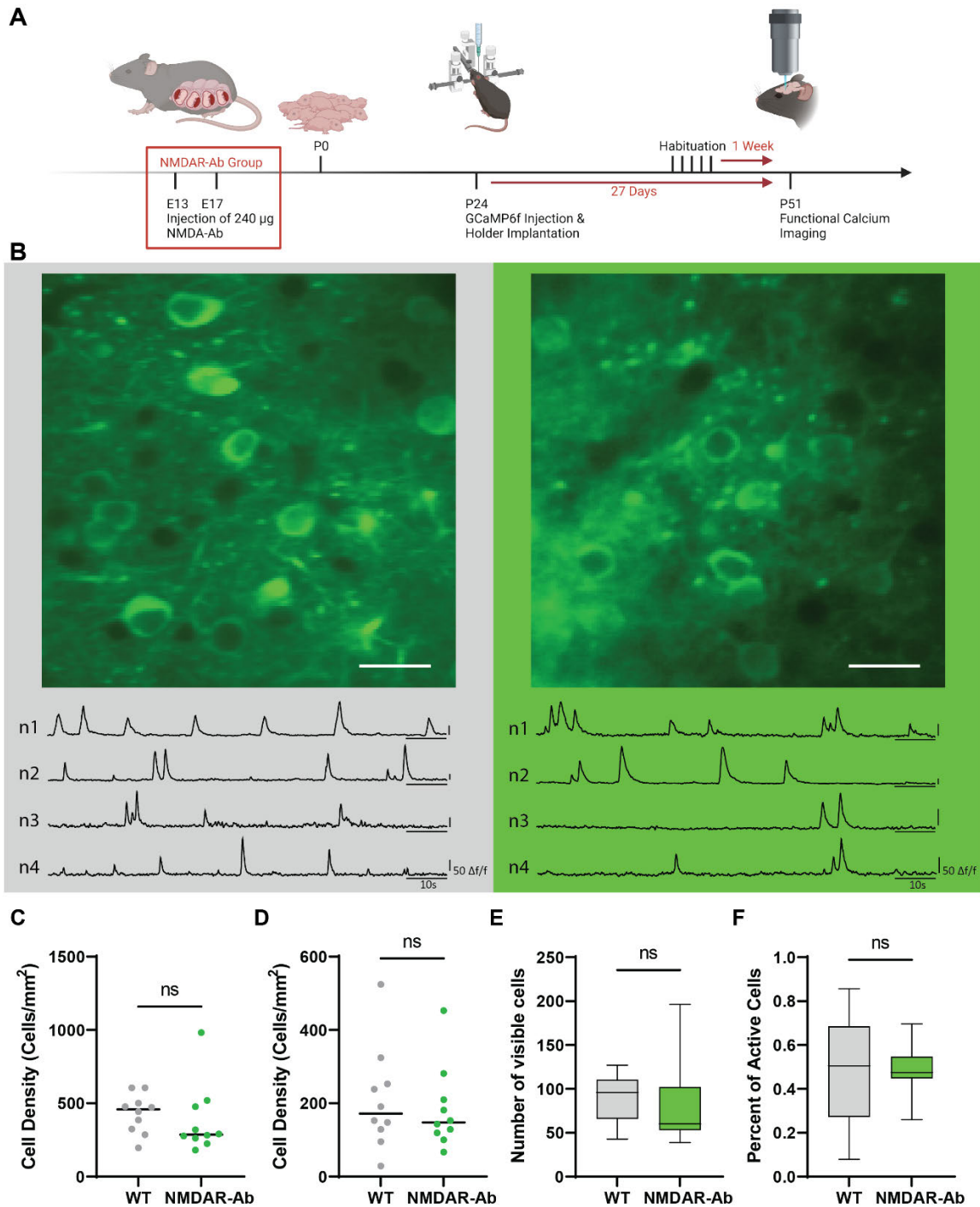


Figure 21: Study design and methodological approach.

(A) The timeline of the experiments. For maternofetal transfer of antibodies, pregnant C57BL/6 mice were injected with 240 μg of NMDAR-Ab on gestational day E13.5 and E17.5. On postnatal day 24, the injection of GCaMP6f viral solution and implantation of a chronic window were performed. 3 weeks after the surgery, the mice were habituated to the experimental setup. Imaging was finally conducted on P51. (B) Two-photon imaging fields from WT (left) and NMDAR-Ab (right) and respective extracted fluorescence traces from four selected neurons. (Magnified view from the center of 20x field of view. Scale bar 50 μm). (C) No difference was observed in overall cell density between WT and NMDAR-Ab. (Unpaired t test, $p=0.5811$). (D) No difference in density of spontaneously active cells was detected between WT and NMDAR-Ab exposed animals. (Unpaired t test, $p=0.6664$). (E) No significant difference was seen for the mean number of visible neurons per field of view. (Unpaired t test, $p=0.9469$) (F) No significant differences were present in mean fraction of visible neurons that display spontaneous activity. (Unpaired t test, $p=0.9469$). Panel A was created with BioRender.com.

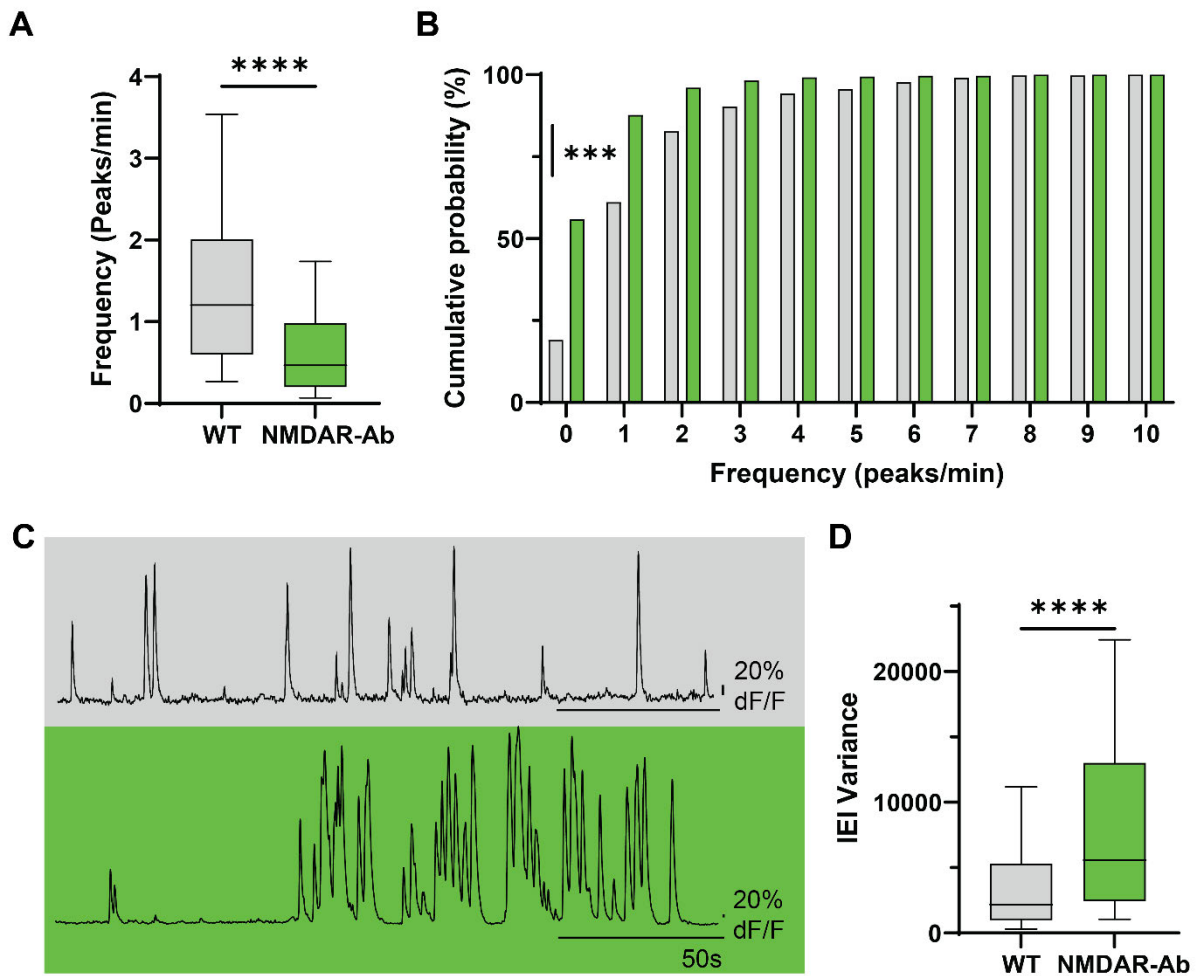


Figure 22: Reduced Spontaneous activity and bursty firing profile in NMDAR-Ab animals.

(A) Spontaneous firing frequencies are reduced in NMDAR-Ab animals. (Mann Whitney test, $p < 0.0001$.) (B) Cumulative frequency distribution of spontaneous activity (Two-way ANOVA, Bin factor $p = 0.0007$, Group factor $p = 0.0387$). (C) Representative fluorescence traces of highly active cells from WT (top) and NMDAR-Ab (bottom). (D) Higher inter-event interval variance in NMDAR-Ab animals. (Mann Whitney test, $p < 0.0001$).

5.2.3. Local microcircuit connectivity remains unchanged after antibody exposure.

To examine functional connectivity strengths within local microcircuits, we conducted network analysis based on Parsons's correlation. This enabled us to create a network graph for each microcircuit (Figure 23A, B), visualizing the activity frequency of the cells and their connection strength. The network graphs are based on the individual correlation matrices of each microcircuit (Figure 23C, D). We found no apparent differences between networks of NMDAR-Ab exposed animals and controls. Similarly, quantifying the overall mean correlation coefficient on a group level showed no significant differences (Figure 23E).

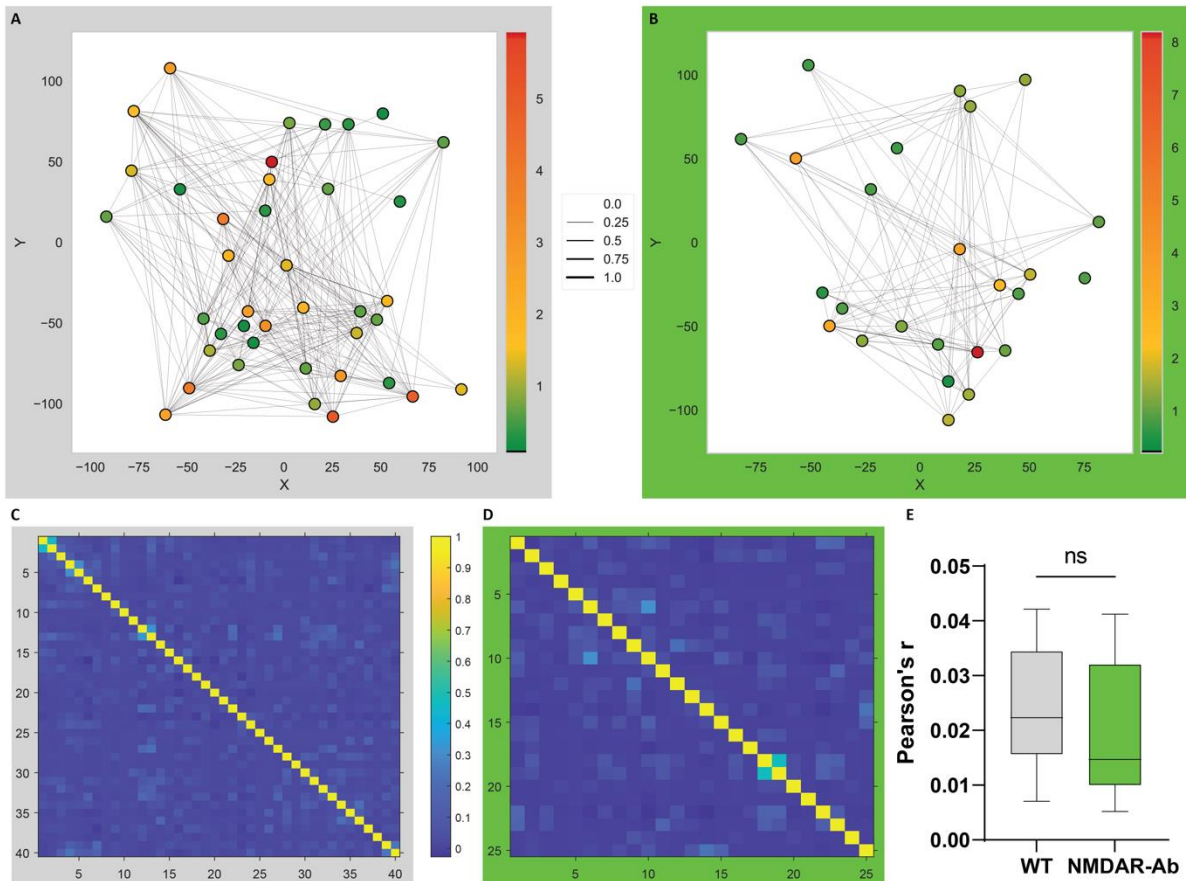


Figure 23: No significant changes in local functional connectivity due to NMDAR-Ab exposure.

(A) An exemplary network graph from a control animal. Colors of the nodes indicate their activity frequency. The thickness of lines between nodes indicates the correlation. (B) Network graph from an NMDAR-Ab exposed animal, same as in A. (C-D) Corresponding correlation matrices from the same networks as in A and B. (E) No significant differences detected in the overall Pearson's correlation coefficient. (Unpaired t test, $p=0.4502$).

5.2.4. V1 excitatory neurons of NMDAR-Ab exposed animals exhibit a higher orientation tuning and a narrowing of their receptive fields.

Returning to the local microcircuit assessed by two-photon Ca^{2+} imaging, we examined the representation of visual stimuli in V1. The animals were subjected to a randomized sequence of 5-second-long drifting and static gratings (Figure 24B) in a 270° virtual reality setup (Figure 24A). Layer II/III of visual cortex is particularly characterized by highly tuned neurons, i.e., neurons responding to only one or few orientations of the gratings. While highly tuned neurons could be observed in both groups, the representation of visual afferents was only altered in NMDAR-Ab exposed mice (Figure 24C, D). Both the circular variance (Figure 24E, G) and the orientation selectivity index (Figure 24F, H), two commonly used measures for assessing the degree of orientation tuning in visual cortex, were shifted towards higher orientation tuning in NMDAR-Ab exposed mice. We then asked whether the higher degree of tuning might be due to the overall lower activity state, as observed in the spontaneous, ongoing activity recordings. However, when randomizing, i.e., reshuffling the timing of the Ca^{2+} transient, while preserving the overall number of calcium transients, the effect vanished. This indicates an active, adaptive to maladaptive network state shift.

We averaged the binarized response patterns across all 11 stimulation trials, resulting in a mean activation matrix for each stimulus, i.e., grating orientation (**Figure 25A**). Calculating the cosine similarity index now allows for an assessment of the degree of similarity of the given responses upon different gratings. NMDAR-Ab exposed animals showed a lower overall similarity (**Figure 25B**), implicating a constriction of the neuron's receptive fields. The decrease in the disease group becomes even more apparent in the respective correlation matrices (**Figure 25C-D**): while in healthy controls, the activity patterns between gratings of different orientations are rather similar, i.e. highly correlated, in NMDAR-Ab mice, each orientation seems to evoke a unique activation pattern, very dissimilar to those of other orientations. A higher proportion of neurons were uniquely active to only one orientation in NMDAR-Ab-exposed animals (**Figure 25E-F**).

5.2.5. Microcircuits of NMDAR-Ab exposed mice maintain a bias towards cardinal orientations.

During the analysis of visually evoked activity patterns, we noticed that most cells have a preference for cardinal orientations (**Figure 26A, B**), i.e. most cells showed the highest activity during the presentation of gratings with an orientation of 0° , 90° , 180° or 270° . This bias is in line with other publications and is known as the "oblique effect" (Appelle, 1972). The fact that neurons of NMDAR-Ab exposed animals still show the bias towards cardinal gratings, hints towards the network potentially compensating to preserve an efficient encoding of visual afferents. Looking further at the visually evoked activity, our approach of using two common measures of cells' orientation selectivity, OSI and CV, raised the question of how they relate to each other. We compared the outcome of both measures for all cells in this study. As expected, a higher OSI corresponds to a lower CV (**Figure 26C**). However, we observed a higher number of cells at the extremes with OSI compared to CV. This indicates that CV might have a more granular distribution of the cells' selectivity. We also wanted to test whether static and drifting grating stimulation are similarly processed by the microcircuit. We calculated the CV for each separately and compared the selectivity for drifting and static gratings. We found that a lower CV in one condition generally corresponds to a low value in the other, but not always (**Figure 26D**). This implies that moving visual stimuli might be differently processed compared to static ones.

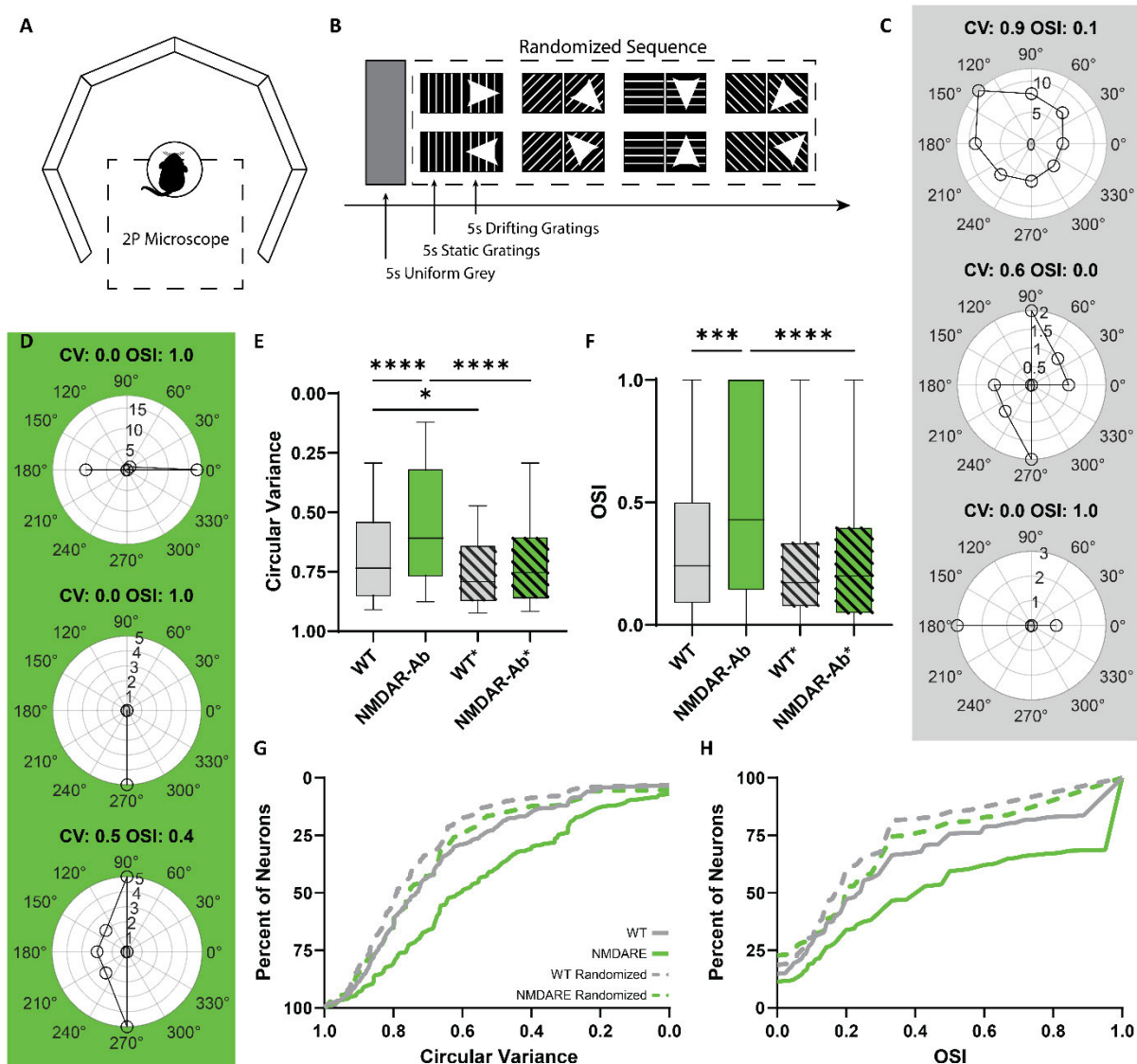


Figure 24: Higher orientation tuning in NMDAR-Ab animals.

(A) Illustration of the virtual reality setup. The mouse is head-mounted under the microscope on a Styrofoam trackball and can move freely in all directions. A 270° surrounding monitor system is placed around the mouse for visual stimulation. (B) Illustration of the visual stimulation paradigm. Each trial starts with 5 seconds of uniform grey screen, followed by a randomized sequence of gratings at different orientations, where each orientation is displayed for 5 seconds statically and then 5 seconds in drifting motion. (C) Exemplary response and orientation tuning plots of three cells from WT mice. (D) Exemplary response and orientation tuning plots of three cells from NMDAR-Ab exposed mice. (E) Lower circular variance (CV) reveals a higher orientation tuning of V1 neurons in NMDAR-Ab compared to WT and randomized controls (*=randomized, Kruskal-Wallis test, WT vs NMDAR-Ab $p < 0.0001$, WT vs. WT* $p = 0.0282$, NMDAR-Ab vs NMDAR-Ab* $p < 0.0001$). (F) Neurons of NMDAR-Ab exposed animals have higher orientation selectivity index (OSI) (*=randomized, Kruskal-Wallis test, WT vs NMDAR-Ab $p = 0.0002$, WT vs. WT* $p < 0.0001$, NMDAR-Ab vs NMDAR-Ab* $p < 0.0001$). (G) Cumulative distribution of CV. (H) Cumulative distribution of OSI.

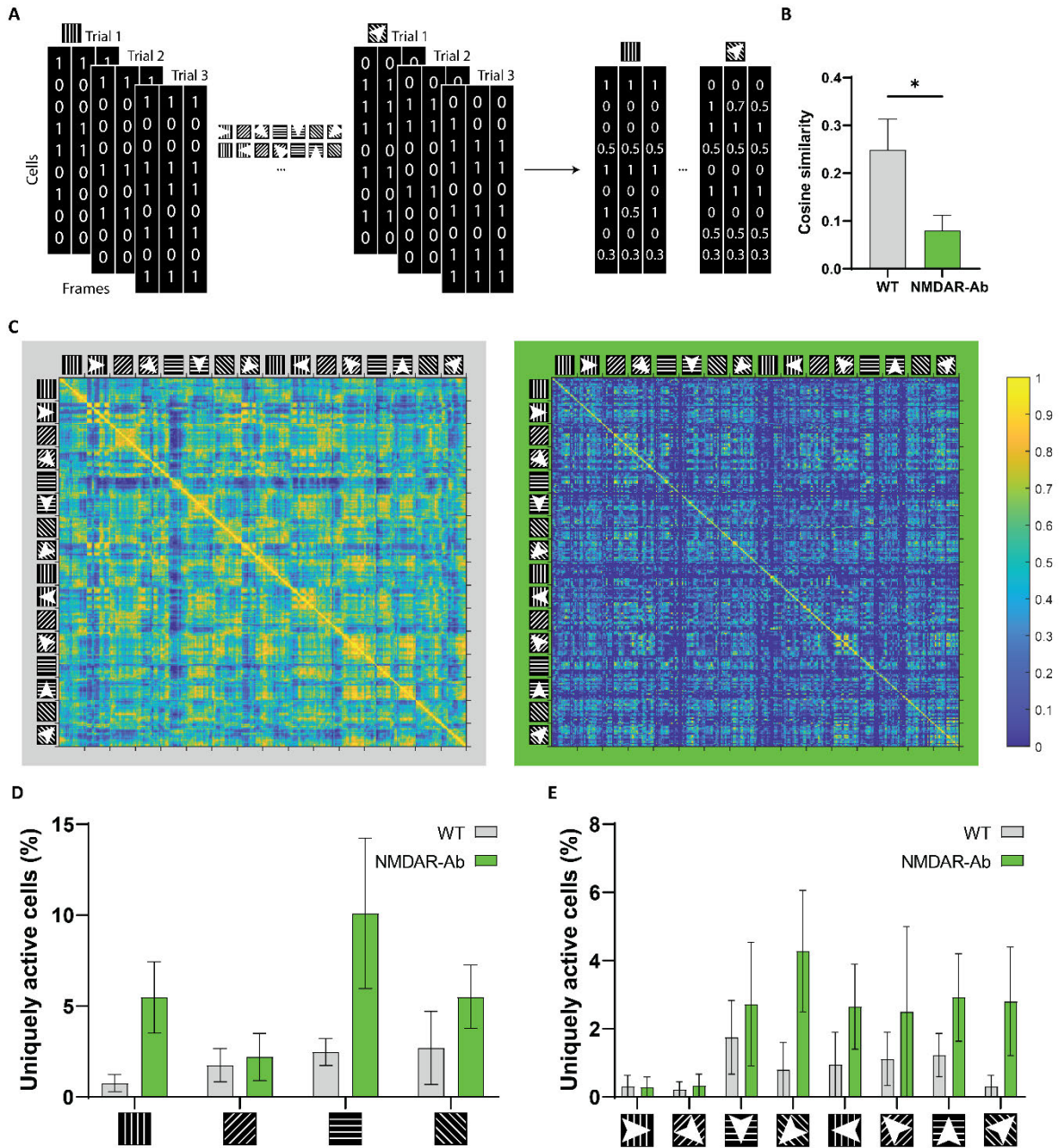


Figure 25: Constriction of V1 neurons receptive fields after NMDAR-Ab exposure.

(A) Schematic illustration of visual response averaging. For each orientation all trials were aligned together and averaged, resulting in a new activity matrix. Rows represent cells and columns represent frames. The values range between 0 and 1 depending on cells activity, where 1 means that the cell had a Ca^{2+} transient at that frame across all 10 trials and 0 means that the cell showed no activity at all. (B) Lower cosine similarity coefficient in NMDAR-Ab animals reflects higher orientation tuning. (WT $n=6$, NMDAR-Ab $n=6$, Unpaired t test with Welch's correction, $p=0.0483$). (C) Correlation matrixes reveal lower similarity in NMDAR-Ab (right) animals when correlating activity matrixes of each orientation. Rows and columns represent the frames of each orientation, color codes for the cosine similarity coefficient. (D-E) A higher proportion of the network is highly selective for only one orientation in NMDAR-Ab animals. Comparison for static gratings (D, Two-way ANOVA, orientation factor $p=0.2349$, group factor $p=0.0136$, interaction $p=0.3954$) and comparison for drifting gratings (E, Two-way ANOVA, orientation factor $p=0.5251$, group factor $p=0.0236$, interaction $p=0.8883$).

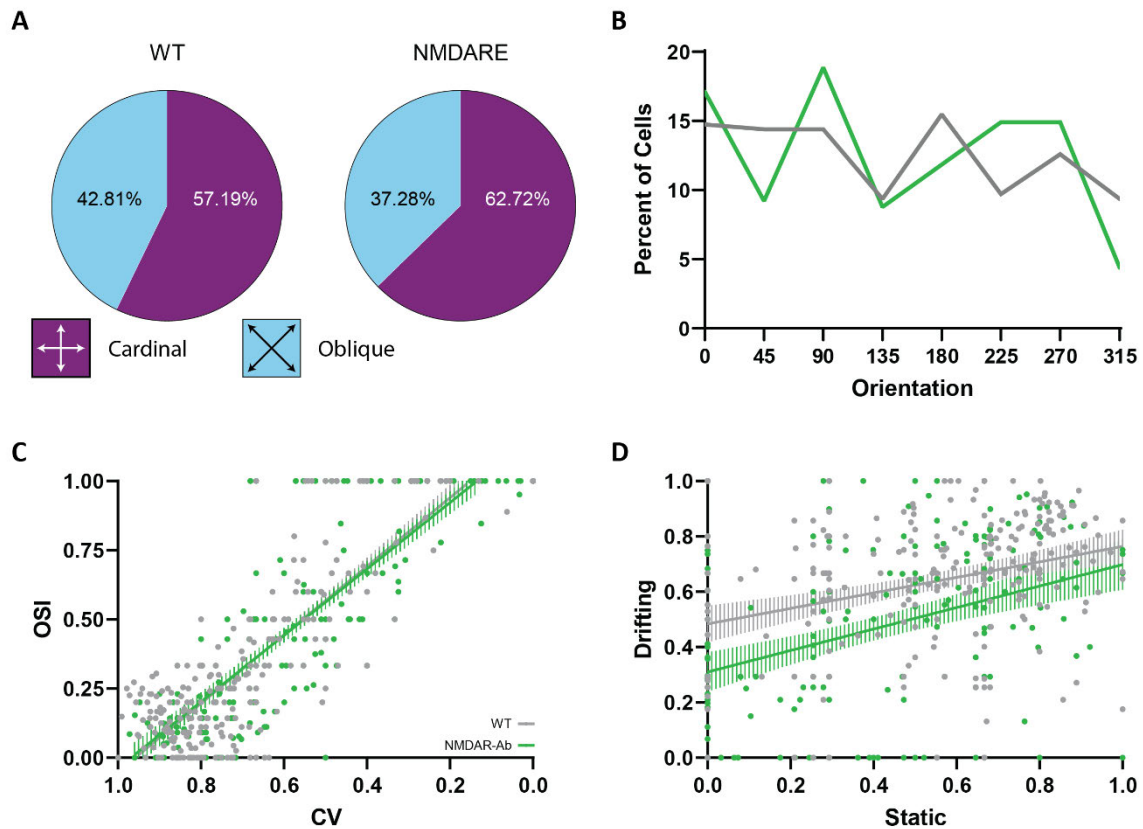


Figure 26: Preserved bias towards cardinal orientations after NMDARE-Ab exposure.

(A) V1 neurons of both NMDAR-Ab exposed animals and controls exhibit a higher preference for cardinal orientations. Pie charts illustrating the orientation preferences of cells. A binomial test against an expected 50% orientation preference revealed significant results (P (one-tailed) = 0.0096, P (two-tailed) = 0.0192). (B) Line chart displaying the detailed distribution of orientation preferences. This provides a more granular view of the distribution patterns observed in A. (C) Scatter plot and simple regression line fitting comparing circular variance (CV) and orientation selectivity index (OSI) for NMDA-Ab and Control animals. Higher OSI values correspond to lower CV values. Best-fit line equations and 95% confidence intervals (profile likelihood) are shown ($R^2 = 0.7420$ and 0.7346 , line equations: $Y = -1.200 * X + 1.162$ and $Y = -1.239 * X + 1.188$ for NMDA-Ab and WT respectively). (D) Comparison of CV values between drifting gratings and static gratings in NMDA-Ab and Control animals. Both NMDA-Ab and Control groups exhibit a significant non-zero slope ($F = 30.68$, DFn , $DFd = 1, 194$, $P < 0.0001$ and $F = 25.28$, DFn , $DFd = 1, 252$, $P < 0.0001$, respectively), indicating a significant deviation from zero. ($R^2 = 0.1365$ and 0.09119 , line equations: $Y = 0.3881 * X + 0.3099$ and $Y = 0.2802 * X + 0.4837$ for NMDA-Ab and WT respectively).

5.2.6. Local cortical networks in NMDAR-Ab exposed animals are characterized by a dissociation between spontaneous and visually evoked activity.

In healthy circuits, spontaneous activity provides a replay of the earlier representation of sensory afferents, i.e., similar network motives should occur (Miller et al., 2014). As we recorded the very same neuron both task-free, as well as upon visual stimulation, we could directly ask, whether the same neuron is active under both conditions, in the absence of modality-specific sensory input, and upon grating stimulation. Indeed, in healthy controls, neurons were generally active under both conditions (**Figure 27A**). In sharp contrast, this overlap vanished almost completely in NMDAR-Ab exposed mice. In the disease group, the majority of neurons were either active spontaneously or active upon visual stimulation. Even within the visually activated neurons, the majority is only active upon a distinct orientation (**Figure 25E, F**). Both functional populations, while very much overlapping in healthy controls, are almost entirely separated. This indicates a dissociation between spontaneous and sensory-evoked activity (**Figure 27B, C**).

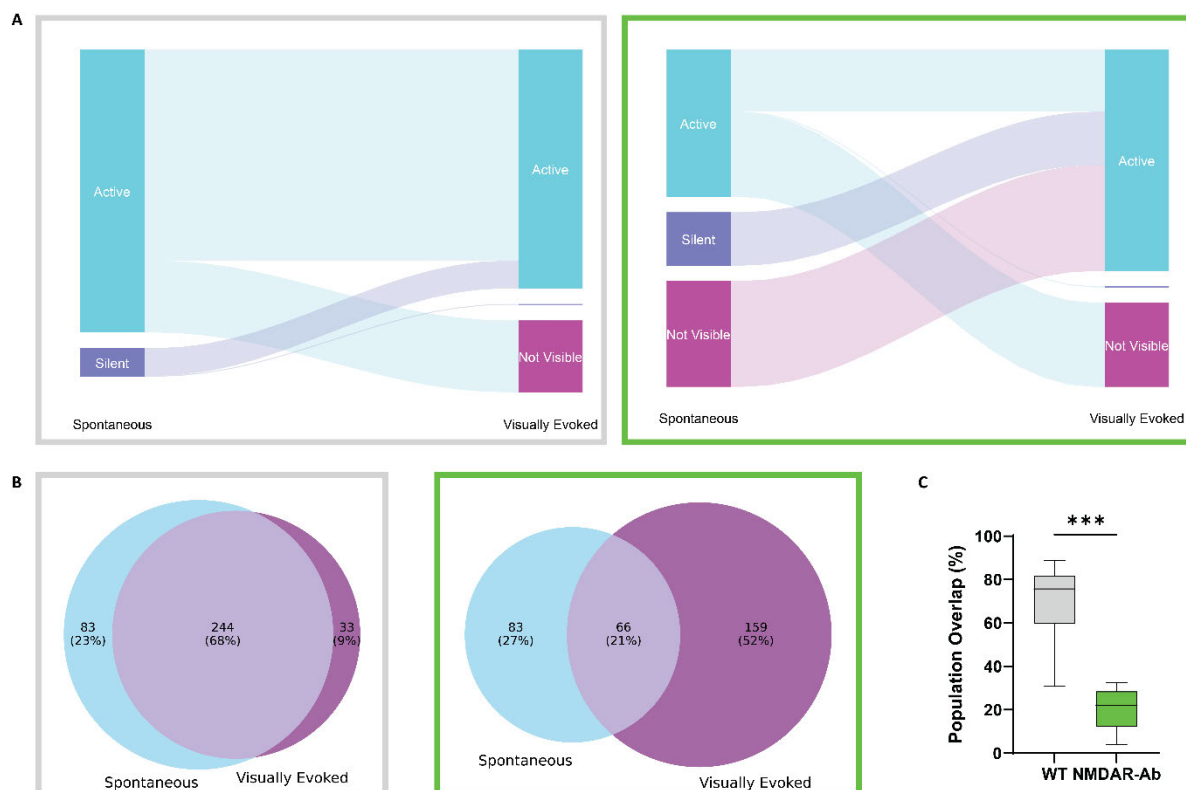


Figure 27: Dissociation of neuronal population recruited by spontaneous activity and visual stimulation in NMDAR-Ab exposed animals.

(A) Larger fraction of spontaneously inactive cells show activity under visual stimulation in NMDAR-Ab (right) compared to WT (left). Cells that are inactive in both conditions are excluded from analysis. **(B)** Antibody exposure leads to a significant reduction in population overlap between spontaneously active and visually activated cells. The numbers and percentages are related to all cells observed in this study. **(C)** The reduction in population overlap is visible on an individual level. ($n = 6$ animals for each WT and NMDAR-Ab, unpaired t -test, $p=0.0003$).

6. Discussion

6.1. functional state changes caused by NMDAR-Ab exposure

Our study reveals that a maternofetal transfer of anti-NMDAR antibodies leads to multiple cortical network defects in adult offspring mice. As NMDARs are found throughout the cortex, we chose to examine the primary visual cortex. This allowed us to examine deficits including both aberrant spontaneous network dynamics as well as processing of sensory afferents (**Figure 28**). First, we report that NMDAR-Ab exposure leads to reduced spontaneous activity and a bursty firing profile. This represents a distinctive and maladaptive microcircuit signature which may have an effect on the temporal stability of ensemble states. Second, our study showed no significant differences in the local microcircuit functional connectivity in NMDAR-Ab exposed mice compared to healthy controls. This indicates that the antibodies' effects are mostly homogenous, affecting the whole microcircuit. Third, in NMDAR-Ab exposed mice, excitatory V1 neurons exhibit a distinct aberration in the processing of visual afferents with a narrowing of visual neurons' receptive fields. Fourth, we found the bias towards cardinal orientation to be preserved in NMDAR-Ab exposed microcircuits. This hints at the network potentially compensating to maintain efficient encoding of visual representations. Lastly and most importantly, we found a dissociation between spontaneous and visually evoked activity, i.e., cells that are spontaneously active do not contribute to visual representations and cells that do, are not spontaneously active. These findings may represent a key pathological mechanism in the development of psychiatric disorders well beyond NMDAR encephalitis.

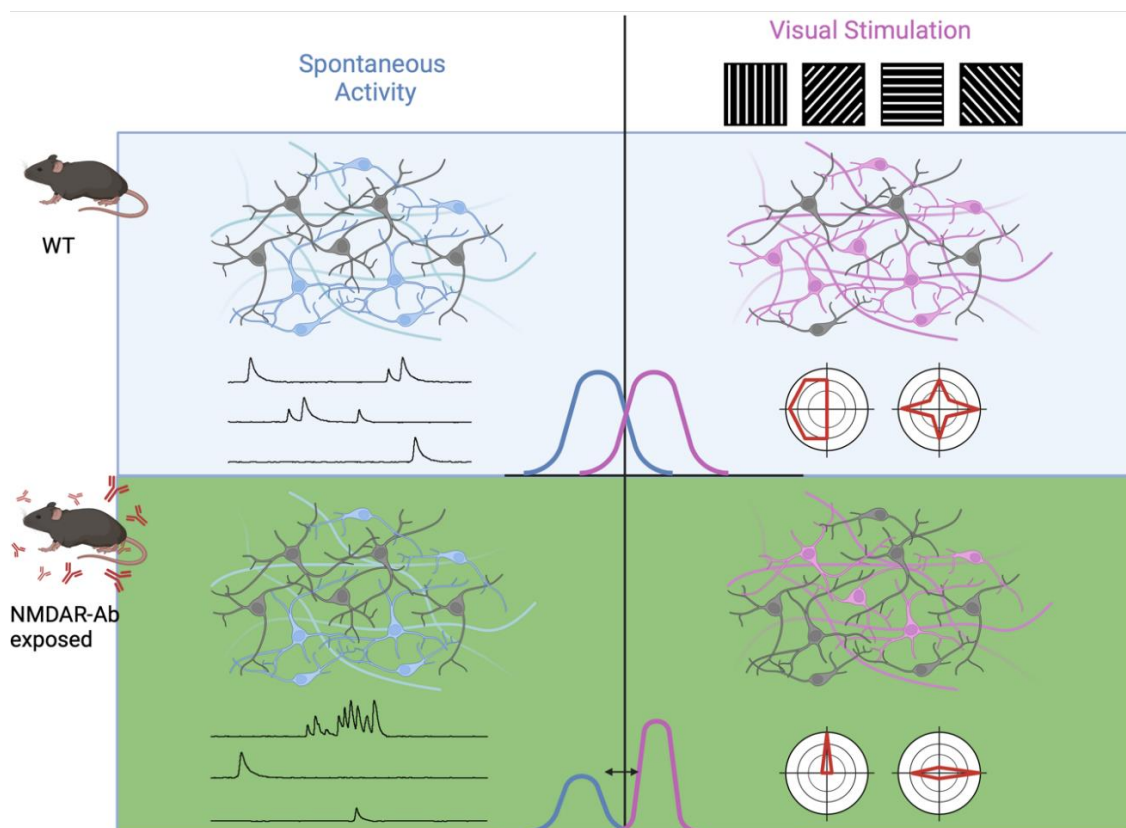


Figure 28: Exposure to anti-NMDAR antibodies leads to functional defects of cortical microcircuits.

Under spontaneous conditions (left panel), NMDAR-Ab exposure leads to reduced activity and a bursty firing profile. During visual stimulation (middle panel), excitatory V1 neurons in exposed mice exhibit a higher orientation tuning to visual stimuli such as static and drifting gratings. Most importantly, we found a dissociation between spontaneous and visually evoked activity patterns, where most cells that are spontaneously active do not contribute to visual representations and cells that do, are not spontaneously active. Figure created with BioRender.com

6.1.1. Distinct functional microarchitecture characterized by low-active, bursty neurons

Our functional calcium imaging data revealed a circuit-wide transition to a state of low spontaneous activity in NMDAR-Ab exposed mice. This is in sharp contrast to findings in early states of neurological disorders, such as Alzheimer's Disease, Multiple Sclerosis and Huntington's Disease. In those disorders, a shift towards hyperactivity has been reported by many (Arnoux et al., 2018, Rosales Jubal et al., 2021, Ellwardt et al., 2018, Burgold et al., 2019, Wei et al., 2021, Sosulina et al., 2021). However, this dysregulation was limited to a subset of excitatory neurons exhibiting an increased firing rate. In this study, we did not find only a sub-population of neurons to be dysregulated. Rather, the network defect seems to affect the entire local excitatory network. This is in line with our finding that the local functional connectivity is not significantly altered. Functional connectivity analyses, based on correlation analysis such as adopted here, are not capable of revealing absolute measures. As long as any effect is homogeneously distributed in the entire network, no changes will be detected.

The bursty firing pattern in V1 excitatory neurons in NMDAR-Ab exposed animals represents a critical deviation to the general sparse firing of cortical networks in healthy circuits (Petersen and Crochet, 2013). A concentration of activity in time could be a compensation mechanism for a decreased synaptic receptor density. Dysfunction of inhibitory networks might be a candidate mechanism evoking bursty firing (Zhou and Yu, 2018). In autism spectrum disorder, it is assumed that a shift in the balance of excitatory and inhibitory neuronal activity (E/I-balance) underlies pathological mechanism of the symptoms (Kirischuk, 2022, Canitano and Palumbi, 2021). Also in Fragile X syndrome, a monogenetic cognitive impairment syndrome that is the most common cause of ASD, studies hint at an altered E/I-balance (Tempio et al., 2023, Nomura, 2021). These findings are backed up by the fact that patients often show altered glutamine and GABA levels. In the case of ASD and related disorders, a shift towards higher excitability is theorized to lead to instability of the network and imprecision in learning and cognition. Accordingly, here, the combination of a shift towards lower excitability, and increased precision in visual representations would be very much in line with the aforementioned theory, albeit in the opposing direction.

6.1.2. Altered yet efficient encoding of visual representations

The analysis of visually evoked activity revealed a significant increase in orientation tuning. The mechanism for the emergence of orientation selectivity in the visual cortex is still a mystery, although there are some theories about it (Scholl et al., 2013, Priebe, 2016, Pattadkal et al., 2018, Xu et al., 2020a). One hypothesis is that a broad inhibition and a narrow enhancement of a neuron's activity around a preferred orientation drives this selectivity (Shapley et al., 2003). Here, an E/I-balance shifted towards increased inhibition could as well be an explanation for the increased selectivity we observed in neurons of NMDAR-Ab exposed animals. Our data did not just show an increased tuning, but also a decrease in the temporal stability of visually evoked activity patterns.

This can be considered as an increased adaptation to visual stimuli (Piasini et al., 2021), as the networks of NMDAR-Ab exposed animals did not even hold the same evoked patterns for a similar duration of each orientation, as that of control animals. Inhibitory interneurons play an important role in controlling adaptation and attention modulation in the visual cortex (Heintz et al., 2022). If we assume a shift towards increased inhibition due to the antibody exposure, as indicated by the other findings, the increased adaptation can be explained as well.

While we cannot provide any absolute metrics by the data from this study about the network's performance in processing visual afferents, one aspect stands out: the oblique effect (OE). This effect refers to the bias towards increased selectivity for visuals with a horizontal or vertical orientation (Appelle, 1972) and is observed in many species, including humans and mice. It is believed that the OE increases the networks efficiency in encoding visual representations, as cardinal orientations are more frequently occurring in nature (Henderson and Serences, 2021). Our data show that microcircuits of NMDAR-Ab exposed animals still exhibit such bias. This might be a hint that the other findings like the reduced firing frequency and increased orientation selectivity could be compensatory in part, to preserve an efficient encoding.

6.1.3. Early, *in utero*, exposure leads to a long-term (mal)adaptive network state

One particular aspect of our study represents the large developmental interval between the administration of the NMDAR-Ab at E13.5 and E17.5, roughly comparable to the 5th and 15th gestational week in humans, and the assessments of the network state in P51, roughly corresponding to early adulthood. Our data show that even a short transient exposure to NMDAR-Ab can lead to long lasting defects. Early, *in utero*, exposure to plasticity-mediating factors seems to lead to a long-term maladaptive network state. Our model bears a high translational weight, as we administered human-derived recombinant antibodies isolated from CSF samples of encephalitis patients (Kreye et al., 2016). Exposure to human NMDAR-Ab was found to affect dendritic branching and maturation in cell cultures of rat cortical neurons (Okamoto et al., 2022). A phenotypic assessment in a very comparable maternofetal transfer of human NMDAR-Ab resulted in altered nest building, poor motor coordination and impaired memory (Garcia-Serra et al., 2021). On the clinical side this is of special relevance, since the seroprevalence of anti-NMDAR-Ab was found in up to 1 % of healthy individuals.

6.1.4. Subtle long-term effects of *in utero* antibody exposure, a representation of a network one hit away from total breakdown?

In NMDAR-Ab exposed animals, our data shows a network characterized by many subtle deficits and deviations from the normal operation mode of a healthy network. Yet, some of those alterations could be considered as compensatory changes to maintain efferent encoding of visual afferents, as indicated by the presence of the OE. Similarly, NMDAR-Ab exposed animals tend to recover from the behavioral changes caused by the antibodies at old age (Garcia-Serra et al., 2021). Based on all of this, we believe that the maternofetal transfer of the antibodies leads to a particularly vulnerable cortical circuitry characterized by many subtle deficits and deviations from the normal. During the critical time window of brain development until adulthood, a potential second hit from environmental factors such as trauma, social distress, drug abuse etc., could exacerbate the malfunctioning of the neuronal circuitry and thereby lead to clinical very prominent phenotypes with high psychiatric morbidity.

6.1.5. Dissociation of the neuronal representation of ongoing – spontaneous – and visually evoked activity – a generalizable mechanism underlying psychosis?

An important theoretical framework of psychosis represents the predictive coding theory (Sterzer et al., 2018). It postulates that impaired NMDAR signaling leads to a weakening of internal predictions while the precision of external sensory inputs is increased. Internal predictions will be necessarily reflected by spontaneous, ongoing activity. Indeed, ongoing activity includes both a replay of previous visual stimuli as well as an anticipation signature. Of note, these predictions are not limited to prefrontal cortical areas, but, are also embedded in primary cortical circuits, such as the visual cortex (Zatka-Haas et al., 2021, Luczak et al., 2009, Stringer et al., 2019). This predicted bimodal shift is very much in line with our findings. The misalignment of predictions and current representations, either in time or in space, might represent the network correlate of psychotic symptoms (Friston, 2005). Such mismatch can lead the network to interpret known stimuli as new and flag them as attention needing, which on the long term can overwhelm the brain and exacerbate feelings of paranoia, making one believe that everything is constantly being manipulated and changed.

Our finding that the neuronal population recruited by spontaneous activity and visual stimulation in healthy controls dissociates in NMDAR-Ab exposed brain might reflect the dissociation of internal predictions and sensory input during psychosis in the framework of predictive coding. This maladaptive network state shift in processing of external sensory inputs already taking place in primary visual areas is opening up a network-centered theory on neuropsychiatric symptoms. Finally, it may eventually lead to new therapeutic, network informed interventions.

6.2. Improved data analysis pipeline

Functional calcium imaging has enabled us and many other researchers to probe network dynamics under various contexts. Yet, the data directly generated by calcium imaging is, raw, and needs a powerful and detailed analysis to transform it to useful and understandable information. In this work, we paid special attention to current analysis approaches. We proposed standardized quality assessment steps to ensure accurate and efficient analysis. We introduced a new ImageJ plugin that addresses the drawbacks of common intensity projection approaches, leading to enhanced cell visualization. This plugin and its source code are publicly available. We also contributed to the development of ViNe-Seg, the deep-learning assisted segmentation software that focuses on the user aspect of the analysis. This software is also publicly available for the scientific community to use. Lastly, we tested state-of-the-art machine learning models for real-time frame-by-frame analysis and introduced an intuitive GUI that enables the user to evaluate the results of the model in real time.

6.2.1. Powerful calcium analysis pipeline to detect subtle network changes

Once calcium imaging data is acquired, the next critical step is the analysis of the data to extract meaningful insights into neuronal activity. But, calcium imaging can be very challenging to analyze due to them being particularly noisy (Robbins et al., 2021). Therefore, meticulous attention to detail is paramount, as even the smallest imperfections can have a substantial impact on the integrity of the results. The most powerful analysis pipeline would not yield useful results if the underlying information about neuronal activity is not discernable from noise. Recognizing the importance of identifying these details is the first step towards their resolution. In this study, we

proposed multiple steps of quality control with examples of common issues to ensure that the collected data and analysis are both robust and trustworthy.

One small detail that might not seem to be very important initially, is the format in which the images are saved. Image format can have a substantial impact on transfer speeds, analysis time and data integrity. The necessary time to finish the analysis of calcium imaging data, at least in a preliminary way, is arguably the most important factor of any analysis pipeline. If a recording turns out to be unusable several days after the initial experiment, it might not be possible to redo the recording. Some recording issues can only be noticeable after some analysis steps. For example, a low SNR might only become noticeable after completing the necessary steps up until trace extraction. Therefore, a very important goal of any study involving calcium imaging should be to incorporate as much as possible of the analysis routine directly after image acquisition. Preliminary analysis results can serve as a quality assurance step to ensure that the most information can be successfully extracted from the recording.

6.2.2. Fast and accurate machine learning assisted analysis

In this work, we contributed to the development of ViNe-Seg in two main ways. We developed a very fast trace extraction algorithm to deliver the results more quickly. In addition, we created a model manager to enable the user to select the right ML model for their datasets. ViNe-Seg offers multiple models with different architecture that were trained on different datasets. For segmentation of calcium imaging datasets, the choice of the model is very important. Unlike the problems that computer vision has evolved to easily solve, like detecting everyday objects in images, detecting neuronal somata and segmenting them out of calcium imaging data is much more difficult (Abbas and Masip, 2022). For one, neuronal somata are much smaller in pixel size compared to the normal objects which those models were originally designed to detect. Moreover, calcium recordings tend to be high bit-depth, one-channel images instead of the everyday 8-bit images with three RGB channels. Therefore, the model's architecture needs to be adapted for this format. Some research groups tried to repurpose pre-trained neural networks for the problem of calcium imaging segmentation without adjusting the networks architecture, like RetinaNet and UNet2d (Klibisz et al., 2017, Sità et al., 2022). Not to mention that some machine learning algorithms were not designed for instance segmentation, but for semantic segmentation (**Figure 29**). For example, UNet can classify each pixel as belonging to the object or background, practically segmenting out a single continuous object in each image. Additional algorithms must process the output of the model to separate the objects into multiple instances, potentially introducing errors (Kornilov et al., 2022).

Another problem is that single frames of calcium recordings are noisy, and a clear view of all cells is sometimes only achievable using intensity projections. This can not only impact automatic segmentation approaches that rely on intensity projections, but also manual segmentation. In this work, we introduced StaAv Tool to address those issues. This approach of strategic sampling can be translated into any programming language to be incorporated into other analysis pipelines.

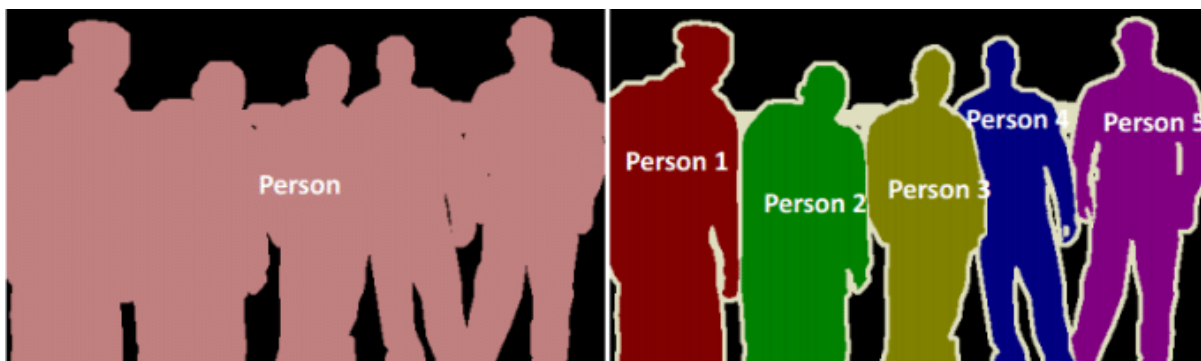


Figure 29: Semantic vs instance segmentation.

With semantic segmentation (left), each pixel of the image is classified as either belonging to an object or the background. On the other hand, instance segmentation (right) distinguishes between individual instances of the same object. From Varatharasan et al. (2019) with permission. © 2019 IEEE.

6.2.3. Towards real-time closed-loop experiments

One major advantage of calcium imaging is that it can easily be combined with optogenetics for an all-optical approach for reading and manipulating neuronal activity (Backhaus et al., 2023). Such an approach can be further developed into a closed-loop system, where the optogenetic intervention is based on current network dynamic. Ideally, the optogenetic intervention should emulate naturalistic network dynamics, to enable the unraveling of complex interactions, especially in the context of movement, memory, cognition and consciousness disorders (Altahini et al., 2023). This requires a fully integrated system for real-time automatic analysis pipeline, since neuronal interactions happen in very small timescales that do not allow for delays in such context (Backhaus et al., 2023). We experimented with Mask RCNN, a state-of-the-art machine learning model, to test whether it can be reliably used for real-time frame-by-frame analysis. Our results show that it can detect both neurons and vessels in single frames. This makes the results not only useful for frame-by-frame analysis but also for live quality control. With Mask RCNN, the additional detection of vessels can be used as landmarks to detect motion artifacts. In cases where longitudinal imaging of the same region is desired, the vessel information can be used to compare the region with previous recordings, since they are more likely not to change as much as the visibility of neurons.

The speed of Mask RCNN can easily match image acquisition frequencies up to 60 Hz on a capable hardware. Beside Mask RCNN, some newer models such as YOLOv8 are even faster (Jocher et al., 2022). However, for true real-time results useable for a closed-loop application, the latency of the analysis is paramount. To fully optimize efficiency, integration within the image acquisition software is necessary. Without this, the time lost in writing images to disk and subsequently reading them can be very significant, leading to delays and inefficiencies for real-time applications. The possibility of incorporating an analysis routine on newly acquired images before they are written to disk relies mostly on the acquisition software. If the microscope's software is flexible enough, Mask RCNN or other fast models can be used for closed-loop experiments, allowing a network centered approach to unravel complex neuronal interactions.

7. Summary and Conclusion

In this work, we examined the long-term effects of transient *in utero* exposure to NMDAR-Ab. When present in CSF, these antibodies are known to cause NMDARE in young adults, triggering severe neuropsychiatric symptoms. Alarmingly, they have been identified in up to 1% of healthy individuals, suggesting a potential risk for transmission to the developing fetal brain during pregnancy. To investigate the effects of the antibodies, we used a mouse model of maternofetally transferred human NMDAR-Ab. At P51, corresponding to early adulthood in humans, we conducted two-photon calcium imaging in awake behaving mice. To be able to detect the most subtle alterations in the network dynamics using calcium imaging, we first had to establish a powerful and fine-tuned analysis pipeline.

We started by looking at currently used analysis routines. From the possible methods for analysis, we opted for a semi-automatic approach, known for its precision. To eliminate any potential noise from interfering with the results, our analysis was based on the binarization of calcium transients. In the pursuit of accuracy, every aspect of the analysis pipeline was meticulously scrutinized, and multiple quality control checkpoints were implemented. Even the smallest imperfections in the analysis routine can have a substantial impact on the integrity of the results. During this work, we introduced three new tools. First, we developed StaAv Tool, a java based ImageJ plugin for enhancing cells' visibility in intensity projections. This plugin and its source code are publicly available on our GitHub. Second, we contributed to ViNe-Seg, a deep-learning assisted segmentation software. ViNe-Seg is publicly available on GitHub as well. Third and last, we experimented with Mask RCNN for a near real-time frame-by-frame analysis. To simplify its useability, we crafted an intuitive user interface meticulously designed to enhance user experience. Our implementation of the model proved very powerful, capable of detecting both vessels and neurons even in low SNR individual frames of calcium recordings.

Returning to the neurophysiological aspect of this work, our analysis showed that the transient *in utero* exposure to NMDAR-Ab can still have a significant impact on the network, even more than 7 weeks after birth. In the exposed animals, the examined cortical networks are characterized by multiple subtle deficits and deviations from the normal operation mode of a healthy network. These alterations can be categorized into three key points:

- I. **The Homogeneous effects of NMDAR-Ab on spontaneous activity.** Exposed microcircuits exhibited a reduced spontaneous activity and a bursty firing profile. However, the results of the antibodies are rather homogenous, affecting all excitatory neurons equally. This is in contrast with many other neurological disorders, such as Alzheimer's Disease or Multiple Sclerosis, where only a subpopulation of neurons shows differences in firing profile. The homogeneity of the effects also explains why the functional connectivity of exposed networks appears to be unchanged. Connectivity analysis, like the one used in this study, depends on relative measures of activity correlation. If the effect is uniform across the network, changes in functional connectivity might not be detectable.
- II. **Altered processing of visual afferents.** The exposure to NMDAR-Ab did not only result in a higher orientation tuning of the individual cells, but also affected how the network encodes visual afferents. Since the visual stimulation paradigm in this study included 11 randomized trials, averaging the evoked

activity patterns allowed the assessment of the similarity of the responses to the various gratings. This revealed a constriction in the neurons' receptive fields, where a significant percentage of the network will only respond to a single orientation. Therefore, unlike a healthy network, the exposed microcircuits had a reduced similarity in the evoked activity patterns. Yet, those alterations in visual processing might still reflect an efficient encoding. The exposed networks still exhibited a bias towards cardinal orientations – an effect believed to help visual circuitry maintain an efficient encoding of visual afferent.

III. Dissociation of neural populations. The spontaneous activity of cortical networks is believed to be very important, as they include both a replay of previous experiences, as well as an anticipation or a prediction of new inputs. In healthy networks, the majority of the cells are involved in both spontaneous activity patterns, as well as the processing of visual afferents. On the other hand, NMDAR-Ab exposed networks appear to have a dissociation in those two populations. The spontaneously active cells do not contribute to visual processing and the ones that do, are not spontaneously active. This dissociation can lead to the network flagging known experiences as new and attention-needing, which can be very overwhelming.

Some of those findings hint at an underlying shift of E/I-balance towards increased inhibition. As the inhibitory parts of the network also play an important role in modulating the firing profile of excitatory cells and their orientation tuning, future studies should include simultaneous calcium imaging of both inhibitory and excitatory cells. Our data shows that the effects of the antibody exposure appear to be still detectable in adult animals. Yet, comparable studies show that behavioral alterations could resolve in adulthood. This hints at the *in utero* exposure potentially acting as a 1st hit, leading to a vulnerable network that can be easily pushed into total breakdown. Therefore, it might be worthy to include behavioral tests and potential 2nd environmental hits in future studies. Most importantly, the dissociation of spontaneous and visually evoked activity is implicated in the predictive coding theory, an important theoretical framework of psychosis. Exploring this effect of the antibody exposure can help improve our knowledge about the emergence of psychotic symptoms not only in disorders caused by NMDAR-Ab, like NMDARE, but also in many other disorders.

Putting everything together, this work serves as an essential first step towards an understanding of the effects of NMDAR-Ab exposure. Focusing on the underlying transition towards maladaptive network states and shifts in the processing of sensory inputs can help in the development of network-centered theory of neuropsychiatric disorders. Eventually, it could lead to better, more effective treatments and network informed interventions.

8. References

- ABADI, M., AGARWAL, A., BARHAM, P., BREVDO, E., CHEN, Z., CITRO, C., CORRADO, G. S., DAVIS, A., DEAN, J. & DEVIN, M. 2016. Tensorflow: Large-scale machine learning on heterogeneous distributed systems. *arXiv preprint arXiv:1603.04467*.
- ABBAS, W. & MASIP, D. 2022. Computational Methods for Neuron Segmentation in Two-Photon Calcium Imaging Data: A Survey. *Applied Sciences*, 12, 6876.
- AKERBOOM, J., RIVERA, J. D., GUILBE, M. M., MALAVÉ, E. C., HERNANDEZ, H. H., TIAN, L., HIRES, S. A., MARVIN, J. S., LOOGER, L. L. & SCHREITER, E. R. 2009. Crystal structures of the GCaMP calcium sensor reveal the mechanism of fluorescence signal change and aid rational design. *J Biol Chem*, 284, 6455-64.
- ALLEN INSTITUTE FOR BRAIN SCIENCE. 2023. *AllenSDK* [Online]. Available: <https://github.com/AllenInstitute/AllenSDK> [Accessed 24.01.2023].
- ALTAHINI, S., ARNOUX, I. & STROH, A. 2023. Optogenetics 2.0: challenges and solutions towards a quantitative probing of neural circuits. *Biological Chemistry*.
- AMBOSS GMBH. 2023. *Kapitel: Enzephalitis, Sektion: Ätiologie* [Online]. Available: <https://next.amboss.com/de/article/qt0Ce3#Z80952614b7b8432c624c094584ac9e0a> [Accessed 24.01. 2023].
- APPELLE, S. 1972. Perception and discrimination as a function of stimulus orientation: The "oblique effect" in man and animals. *Psychological Bulletin*, 78, 266-278.
- APPLEBY, P. & CATTY, D. 1983. Transmission of immunoglobulin to foetal and neonatal mice. *Journal of Reproductive Immunology*, 5, 203-213.
- ARNOUX, I., WILLAM, M., GRIESCHE, N., KRUMMEICH, J., WATARI, H., OFFERMANN, N., WEBER, S., NARAYAN DEY, P., CHEN, C., MONTEIRO, O., BUETTNER, S., MEYER, K., BANO, D., RADYUSHKIN, K., LANGSTON, R., LAMBERT, J. J., WANKER, E., METHNER, A., KRAUSS, S., SCHWEIGER, S. & STROH, A. 2018. Metformin reverses early cortical network dysfunction and behavior changes in Huntington's disease. *Elife*, 7.
- BACKHAUS, H., RUFFINI, N., WIERCZEIKO, A. & STROH, A. 2023. An All-Optical Physiology Pipeline Toward Highly Specific and Artifact-Free Circuit Mapping. *In: PAPAGIAKOUMOU, E. (ed.) All-Optical Methods to Study Neuronal Function*. New York, NY: Springer US.
- BAEHRING, J. M., HOCHBERG, E. P., RAJE, N., ULRICKSON, M. & HOCHBERG, F. H. 2008. Neurological manifestations of Waldenström macroglobulinemia. *Nature Clinical Practice Neurology*, 4, 547-556.
- BALU, D. T. 2016. The NMDA Receptor and Schizophrenia: From Pathophysiology to Treatment. *Adv Pharmacol*, 76, 351-82.
- BALU, R., MCCRACKEN, L., LANCASTER, E., GRAUS, F., DALMAU, J. & TITULAER, M. J. 2019. A score that predicts 1-year functional status in patients with anti-NMDA receptor encephalitis. *Neurology*, 92, e244-e252.
- BAO, Y., SOLTANIAN-ZADEH, S., FARSIU, S. & GONG, Y. 2021. Segmentation of neurons from fluorescence calcium recordings beyond real time. *Nature Machine Intelligence*, 3, 590-600.
- BENROS, M. E., WALTOFT, B. L., NORDENTOFT, M., OSTERGAARD, S. D., EATON, W. W., KROGH, J. & MORTENSEN, P. B. 2013. Autoimmune diseases and severe infections as risk factors for mood disorders: a nationwide study. *JAMA Psychiatry*, 70, 812-20.
- BERENS, P., FREEMAN, J., DENEUX, T., CHENKOV, N., MCCOLGAN, T., SPEISER, A., MACKE, J. H., TURAGA, S. C., MINEAULT, P., RUPPRECHT, P., GERHARD, S., FRIEDRICH, R. W., FRIEDRICH, J., PANINSKI, L., PACHITARIU, M., HARRIS, K. D., BOLTE, B., MACHADO, T.

- A., RINGACH, D., STONE, J., ROGERSON, L. E., SOFRONIEW, N. J., REIMER, J., FROUDARAKIS, E., EULER, T., ROMÁN ROSÓN, M., THEIS, L., TOLIAS, A. S. & BETHGE, M. 2018. Community-based benchmarking improves spike rate inference from two-photon calcium imaging data. *PLOS Computational Biology*, 14, e1006157.
- BERRIDGE, M. J., BOOTMAN, M. D. & RODERICK, H. L. 2003. Calcium signalling: dynamics, homeostasis and remodelling. *Nature Reviews Molecular Cell Biology*, 4, 517-529.
- BONNEY, S., SEITZ, S., RYAN, C. A., JONES, K. L., CLARKE, P., TYLER, K. L. & SIEGENTHALER, J. A. 2019. Gamma Interferon Alters Junctional Integrity via Rho Kinase, Resulting in Blood-Brain Barrier Leakage in Experimental Viral Encephalitis. *mBio*, 10, 10.1128/mbio.01675-19.
- BOOTHBY, M. R., BROOKENS, S. K., RAYBUCK, A. L. & CHO, S. H. 2022. Supplying the trip to antibody production—nutrients, signaling, and the programming of cellular metabolism in the mature B lineage. *Cellular & Molecular Immunology*, 19, 352-369.
- BRACZKOWSKI, M., SOSZYŃSKI, D., SIERAKOWSKA, A., BRACZKOWSKI, R., KUFEL, K. & ŁABUZ-ROSZAK, B. 2023. Autoimmune Encephalitis with Antibodies: Anti-NMDAR, Anti-AMPA, Anti-GQ1b, Anti-DPPX, Anti-CASPR2, Anti-LGI1, Anti-RI, Anti-Yo, Anti-Hu, Anti-CV2 and Anti-GABAAR, in the Course of Psychoses, Neoplastic Diseases, and Paraneoplastic Syndromes. *Diagnostics*, 13, 2589.
- BRANDES, R., LANG, F., SCHMIDT, R. F. & SPRINGER-VERLAG GMB, H. 2019. *Physiologie des Menschen mit Pathophysiologie*, Berlin, Springer Berlin.
- BURGOLD, J., SCHULZ-TRIEGLAFF, E. K., VOELKL, K., GUTIÉRREZ-ÁNGEL, S., BADER, J. M., HOSP, F., MANN, M., ARZBERGER, T., KLEIN, R., LIEBSCHER, S. & DUDANOVA, I. 2019. Cortical circuit alterations precede motor impairments in Huntington's disease mice. *Scientific Reports*, 9, 6634.
- CANITANO, R. & PALUMBI, R. 2021. Excitation/Inhibition Modulators in Autism Spectrum Disorder: Current Clinical Research. *Frontiers in Neuroscience*, 15.
- CARSON, M. J., DOOSE, J. M., MELCHIOR, B., SCHMID, C. D. & PLOIX, C. C. 2006. CNS immune privilege: hiding in plain sight. *Immunol Rev*, 213, 48-65.
- CARVALHO, L. A., TORRE, J. P., PAPAPOULOS, A. S., POON, L., JURUENA, M. F., MARKOPOULOU, K., CLEARE, A. J. & PARIANTE, C. M. 2013. Lack of clinical therapeutic benefit of antidepressants is associated overall activation of the inflammatory system. *J Affect Disord*, 148, 136-40.
- CATTERALL, W. A. 2011. Voltage-gated calcium channels. *Cold Spring Harb Perspect Biol*, 3, a003947.
- CHOI, D. W., KOH, J. Y. & PETERS, S. 1988. Pharmacology of glutamate neurotoxicity in cortical cell culture: attenuation by NMDA antagonists. *J Neurosci*, 8, 185-96.
- COOKE, S. F. & BLISS, T. V. P. 2006. Plasticity in the human central nervous system. *Brain*, 129, 1659-1673.
- COYLE, J. T. 2012. NMDA receptor and schizophrenia: a brief history. *Schizophr Bull*, 38, 920-6.
- CULLEN, A. E., HOLMES, S., POLLAK, T. A., BLACKMAN, G., JOYCE, D. W., KEMPTON, M. J., MURRAY, R. M., MCGUIRE, P. & MONDELLI, V. 2019. Associations Between Non-neurological Autoimmune Disorders and Psychosis: A Meta-analysis. *Biol Psychiatry*, 85, 35-48.
- DAHM, L., OTT, C., STEINER, J., STEPNIAK, B., TEEGEN, B., SASCHENBRECKER, S., HAMMER, C., BOROWSKI, K., BEGEMANN, M., LEMKE, S., RENTZSCH, K., PROBST, C., MARTENS, H., WIENANDS, J., SPALLETTA, G., WEISSENBORN, K., STOCKER, W. & EHRENREICH, H.

2014. Seroprevalence of autoantibodies against brain antigens in health and disease. *Ann Neurol*, 76, 82-94.
- DALMAU, J., ARMANGUÉ, T., PLANAGUMÀ, J., RADOSEVIC, M., MANNARA, F., LEYPOLDT, F., GEIS, C., LANCASTER, E., TITULAER, M. J., ROSENFELD, M. R. & GRAUS, F. 2019. An update on anti-NMDA receptor encephalitis for neurologists and psychiatrists: mechanisms and models. *The Lancet Neurology*, 18, 1045-1057.
- DALMAU, J., LANCASTER, E., MARTINEZ-HERNANDEZ, E., ROSENFELD, M. R. & BALICE-GORDON, R. 2011. Clinical experience and laboratory investigations in patients with anti-NMDAR encephalitis. *Lancet Neurol*, 10, 63-74.
- DALMAU, J., TÜZÜN, E., WU, H. Y., MASJUAN, J., ROSSI, J. E., VOLOSCHIN, A., BAEHRING, J. M., SHIMAZAKI, H., KOIDE, R. & KING, D. 2007. Paraneoplastic anti-N-methyl-D-aspartate receptor encephalitis associated with ovarian teratoma. *Annals of neurology*, 61, 25-36.
- DANA, H., SUN, Y., MOHAR, B., HULSE, B. K., KERLIN, A. M., HASSEMAN, J. P., TSEGAYE, G., TSANG, A., WONG, A., PATEL, R., MACKLIN, J. J., CHEN, Y., KONNERTH, A., JAYARAMAN, V., LOOGER, L. L., SCHREITER, E. R., SVOBODA, K. & KIM, D. S. 2019. High-performance calcium sensors for imaging activity in neuronal populations and microcompartments. *Nature Methods*, 16, 649-657.
- DANTZER, R., O'CONNOR, J. C., FREUND, G. G., JOHNSON, R. W. & KELLEY, K. W. 2008. From inflammation to sickness and depression: when the immune system subjugates the brain. *Nat Rev Neurosci*, 9, 46-56.
- DENK, W., STRICKLER, J. H. & WEBB, W. W. 1990. Two-Photon Laser Scanning Fluorescence Microscopy. *Science*, 248, 73-76.
- DENK, W. & SVOBODA, K. 1997. Photon upmanship: why multiphoton imaging is more than a gimmick. *Neuron*, 18, 351-7.
- DOLEV, N., PINKUS, L. & RIVLIN-ETZION, M. 2019. Segment2P: Parameter-free automated segmentation of cellular fluorescent signals. *bioRxiv*, 832188.
- DUBBS, A., GUEVARA, J. & YUSTE, R. 2016. moco: Fast Motion Correction for Calcium Imaging. *Front Neuroinform*, 10, 6.
- ELLWARDT, E., PRAMANIK, G., LUCHTMAN, D., NOVKOVIC, T., JUBAL, E. R., VOGT, J., ARNOUX, I., VOGELAAR, C. F., MANDAL, S., SCHMALZ, M., BARGER, Z., RUIZ DE AZUA, I., KUHLMANN, T., LUTZ, B., MITTMANN, T., BITTNER, S., ZIPP, F. & STROH, A. 2018. Maladaptive cortical hyperactivity upon recovery from experimental autoimmune encephalomyelitis. *Nat Neurosci*, 21, 1392-1403.
- ERICKSON, M. A. & BANKS, W. A. 2018. Neuroimmune Axes of the Blood–Brain Barriers and Blood–Brain Interfaces: Bases for Physiological Regulation, Disease States, and Pharmacological Interventions. *Pharmacological Reviews*, 70, 278-314.
- FILIANO, A. J., GADANI, S. P. & KIPNIS, J. 2015. Interactions of innate and adaptive immunity in brain development and function. *Brain Res*, 1617, 18-27.
- FRISTON, K. 2005. A theory of cortical responses. *Philos Trans R Soc Lond B Biol Sci*, 360, 815-36.
- FU, T., ARNOUX, I., DÖRING, J., BACKHAUS, H., WATARI, H., STASEVICIUS, I., FAN, W. & STROH, A. 2021. Exploring two-photon optogenetics beyond 1100 nm for specific and effective all-optical physiology. *iScience*, 24.
- GARCIA-SERRA, A., RADOSEVIC, M., PUPAK, A., BRITO, V., RIOS, J., AGUILAR, E., MAUDES, E., ARINO, H., SPATOLA, M., MANNARA, F., PEDRENO, M., JOUBERT, B., GINES, S., PLANAGUMA, J. & DALMAU, J. 2021. Placental transfer of NMDAR antibodies causes reversible alterations in mice. *Neurol Neuroimmunol Neuroinflamm*, 8.

- GIOVANNUCCI, A., FRIEDRICH, J., GUNN, P., KALFON, J., BROWN, B. L., KOAY, S. A., TAXIDIS, J., NAJAFI, F., GAUTHIER, J. L., ZHOU, P., KHAKH, B. S., TANK, D. W., CHKLOVSKII, D. B. & PNEVMATIKAKIS, E. A. 2019. CalmAn an open source tool for scalable calcium imaging data analysis. *eLife*, 8, e38173.
- GLEICHMANN, M. & MATTSON, M. P. 2011. Neuronal calcium homeostasis and dysregulation. *Antioxid Redox Signal*, 14, 1261-73.
- GLOVER, G. H. 2011. Overview of functional magnetic resonance imaging. *Neurosurg Clin N Am*, 22, 133-9, vii.
- GONG, X., CHEN, C., LIU, X., LIN, J., LI, A., GUO, K., ZHOU, D. & HONG, Z. 2021. Long-term Functional Outcomes and Relapse of Anti-NMDA Receptor Encephalitis. A Cohort Study in Western China, 8, e958.
- GÖPPERT-MAYER, M. 1931. Über Elementarakte mit zwei Quantensprüngen. *Annalen der Physik*, 401, 273-294.
- GRAUS, F., TITULAER, M. J., BALU, R., BENSELER, S., BIEN, C. G., CELLUCCI, T., CORTESE, I., DALE, R. C., GELFAND, J. M., GESCHWIND, M., GLASER, C. A., HONNORAT, J., HOFTBERGER, R., IIZUKA, T., IRANI, S. R., LANCASTER, E., LEYPOLDT, F., PRUSS, H., RAEGRANT, A., REINDL, M., ROSENFELD, M. R., ROSTASY, K., SAIZ, A., VENKATESAN, A., VINCENT, A., WANDINGER, K. P., WATERS, P. & DALMAU, J. 2016. A clinical approach to diagnosis of autoimmune encephalitis. *Lancet Neurol*, 15, 391-404.
- GRIENBERGER, C. & KONNERTH, A. 2012. Imaging Calcium in Neurons. *Neuron*, 73, 862-885.
- GRYNKIEWICZ, G., POENIE, M. & TSIEN, R. Y. 1985. A new generation of Ca²⁺ indicators with greatly improved fluorescence properties. *J Biol Chem*, 260, 3440-50.
- GUIMARÃES BACKHAUS, R., FU, T., BACKHAUS, H. & STROH, A. 2021. Pipeline for 2-photon all-optical physiology in mouse: From viral titration and optical window implantation to binarization of calcium transients. *STAR Protocols*, 2, 101010.
- HADDAD-TÓVOLI, R., DRAGANO, N. R. V., RAMALHO, A. F. S. & VELLOSO, L. A. 2017. Development and Function of the Blood-Brain Barrier in the Context of Metabolic Control. *Frontiers in Neuroscience*, 11.
- HAMM, J. P., PETERKA, D. S., GOGOS, J. A. & YUSTE, R. 2017. Altered Cortical Ensembles in Mouse Models of Schizophrenia. *Neuron*, 94, 153-167.e8.
- HAYWARD, A. R. 1983. The human fetus and newborn: development of the immune response. *Birth Defects Orig Artic Ser*, 19, 289-94.
- HE, K., GKIOXARI, G., DOLLÁR, P. & GIRSHICK, R. Mask r-cnn. Proceedings of the IEEE international conference on computer vision, 2017. 2961-2969.
- HEINE, J., DUCHOW, A., RUST, R., PAUL, F., PRÜß, H. & FINKE, C. 2023. [Autoimmune encephalitis-An update]. *Nervenarzt*, 94, 525-537.
- HEINE, J., KOPP, U. A., KLAG, J., PLONER, C. J., PRÜSS, H. & FINKE, C. 2021. Long-Term Cognitive Outcome in Anti-N-Methyl-D-Aspartate Receptor Encephalitis. *Annals of Neurology*, 90, 949-961.
- HEINTZ, T. G., HINOJOSA, A. J., DOMINIÁK, S. E. & LAGNADO, L. 2022. Opposite forms of adaptation in mouse visual cortex are controlled by distinct inhibitory microcircuits. *Nature Communications*, 13, 1031.
- HENDEL, T., MANK, M., SCHNELL, B., GRIESBECK, O., BORST, A. & REIFF, D. F. 2008. Fluorescence changes of genetic calcium indicators and OGB-1 correlated with neural activity and calcium in vivo and in vitro. *J Neurosci*, 28, 7399-411.
- HENDERSON, M. & SERENCES, J. T. 2021. Biased orientation representations can be explained by experience with nonuniform training set statistics. *J Vis*, 21, 10.

- HUSSAIN, T., MURTAZA, G., KALHORO, D. H., KALHORO, M. S., YIN, Y., CHUGHTAI, M. I., TAN, B., YASEEN, A. & REHMAN, Z. U. 2022. Understanding the Immune System in Fetal Protection and Maternal Infections during Pregnancy. *Journal of Immunology Research*, 2022, 7567708.
- IWASAKI, A. 2017. Immune Regulation of Antibody Access to Neuronal Tissues. *Trends Mol Med*, 23, 227-245.
- JOCHER, G., CHAURASIA, A., STOKEN, A., BOROVEC, J., KWON, Y., MICHAEL, K., FANG, J., YIFU, Z., WONG, C. & MONTES, D. 2022. ultralytics/yolov5: v7. 0-yolov5 sota realtime instance segmentation. *Zenodo*.
- JUREK, B., CHAYKA, M., KREYE, J., LANG, K., KRAUS, L., FIDZINSKI, P., KORNAU, H. C., DAO, L. M., WENKE, N. K., LONG, M., RIVALAN, M., WINTER, Y., LEUBNER, J., HERKEN, J., MAYER, S., MUELLER, S., BOEHM-STURM, P., DIRNAGL, U., SCHMITZ, D., KOLCH, M. & PRUSS, H. 2019. Human gestational N-methyl-d-aspartate receptor autoantibodies impair neonatal murine brain function. *Ann Neurol*, 86, 656-670.
- KAESTNER, L., SCHOLZ, A., TIAN, Q., RUPPENTHAL, S., TABELLION, W., WIESEN, K., KATUS, H. A., MÜLLER, O. J., KOTLIKOFF, M. I. & LIPP, P. 2014. Genetically encoded Ca²⁺ indicators in cardiac myocytes. *Circ Res*, 114, 1623-39.
- KAPPELMANN, N., LEWIS, G., DANTZER, R., JONES, P. B. & KHANDAKER, G. M. 2018. Antidepressant activity of anti-cytokine treatment: a systematic review and meta-analysis of clinical trials of chronic inflammatory conditions. *Mol Psychiatry*, 23, 335-343.
- KIPNIS, J., CARDON, M., AVIDAN, H., LEWITUS, G. M., MORDECHAY, S., ROLLS, A., SHANI, Y. & SCHWARTZ, M. 2004. Dopamine, through the extracellular signal-regulated kinase pathway, downregulates CD4+CD25+ regulatory T-cell activity: implications for neurodegeneration. *J Neurosci*, 24, 6133-43.
- KIRISCHUK, S. 2022. Keeping Excitation–Inhibition Ratio in Balance. *International Journal of Molecular Sciences*, 23, 5746.
- KIRSCHBAUM, E., BAILONI, A. & HAMPRECHT, F. A. 2019. DISCo: Deep learning, Instance Segmentation, and Correlations for cell segmentation in calcium imaging. *arXiv preprint arXiv:1908.07957*.
- KLIBISZ, A., ROSE, D., EICHOLTZ, M., BLUNDON, J. & ZAKHARENKO, S. Fast, Simple Calcium Imaging Segmentation with Fully Convolutional Networks. *In: CARDOSO, M. J., ARBEL, T., CARNEIRO, G., SYEDA-MAHMOOD, T., TAVARES, J. M. R. S., MORADI, M., BRADLEY, A., GREENSPAN, H., PAPA, J. P., MADABHUSHI, A., NASCIMENTO, J. C., CARDOSO, J. S., BELAGIANNIS, V. & LU, Z., eds. Deep Learning in Medical Image Analysis and Multimodal Learning for Clinical Decision Support, 2017// 2017 Cham. Springer International Publishing, 285-293.*
- KOHLER-FORSBERG, O., C, N. L., HJORTHJ, C., NORDENTOFT, M., MORS, O. & BENROS, M. E. 2019. Efficacy of anti-inflammatory treatment on major depressive disorder or depressive symptoms: meta-analysis of clinical trials. *Acta Psychiatr Scand*, 139, 404-419.
- KONG, S. S., CHEN, Y. J., SU, I. C., LIN, J. J., CHOU, I. J., CHOU, M. L., HUNG, P. C., HSIEH, M. Y., WANG, Y. S., CHOU, C. C., WANG, H. S., LIN, K. L. & GROUP, C. S. 2019. Immunotherapy for anti-NMDA receptor encephalitis: Experience from a single center in Taiwan. *Pediatr Neonatol*, 60, 417-422.
- KONSMAN, J. P. 2019. Inflammation and Depression: A Nervous Plea for Psychiatry to Not Become Immune to Interpretation. *Pharmaceuticals (Basel)*, 12.

- KORNILOV, A., SAFONOV, I. & YAKIMCHUK, I. 2022. A Review of Watershed Implementations for Segmentation of Volumetric Images. *J Imaging*, 8.
- KREYE, J., WENKE, N. K., CHAYKA, M., LEUBNER, J., MURUGAN, R., MAIER, N., JUREK, B., LY, L. T., BRANDL, D., ROST, B. R., STUMPF, A., SCHULZ, P., RADBRUCH, H., HAUSER, A. E., PACHE, F., MEISEL, A., HARMS, L., PAUL, F., DIRNAGL, U., GARNER, C., SCHMITZ, D., WARDEMANN, H. & PRÜSS, H. 2016. Human cerebrospinal fluid monoclonal N-methyl-D-aspartate receptor autoantibodies are sufficient for encephalitis pathogenesis. *Brain*, 139, 2641-2652.
- LANG, K. & PRUSS, H. 2017. Frequencies of neuronal autoantibodies in healthy controls: Estimation of disease specificity. *Neurol Neuroimmunol Neuroinflamm*, 4, e386.
- LEE, E. J., CHOI, S. Y. & KIM, E. 2015. NMDA receptor dysfunction in autism spectrum disorders. *Curr Opin Pharmacol*, 20, 8-13.
- LI, F. & TSIEN, J. Z. 2009. Memory and the NMDA receptors. *N Engl J Med*, 361, 302-3.
- LIU, Z., CONROY, W. G., STAWICKI, T. M., NAI, Q., NEFF, R. A. & BERG, D. K. 2008. EphB receptors co-distribute with a nicotinic receptor subtype and regulate nicotinic downstream signaling in neurons. *Mol Cell Neurosci*, 38, 236-44.
- LOERINC, L. B., BLACKWELL, L., HOWARTH, R. & GOMBOLAY, G. 2021. Evaluation of the Anti-N-Methyl-D-Aspartate Receptor Encephalitis One-Year Functional Status Score in Predicting Functional Outcomes in Pediatric Patients with Anti-N-Methyl-D-Aspartate Receptor Encephalitis. *Pediatric Neurology*, 124, 21-23.
- LOHR, C., BEIERSDORFER, A., FISCHER, T., HIRNET, D., ROTERMUND, N., SAUER, J., SCHULZ, K. & GEE, C. E. 2021. Using genetically encoded calcium indicators to study astrocyte physiology: A field guide. *Frontiers in Cellular Neuroscience*, 15.
- LUCZAK, A., BARTHÓ, P. & HARRIS, K. D. 2009. Spontaneous events outline the realm of possible sensory responses in neocortical populations. *Neuron*, 62, 413-425.
- LUSCHER, C. & MALENKA, R. C. 2012. NMDA receptor-dependent long-term potentiation and long-term depression (LTP/LTD). *Cold Spring Harb Perspect Biol*, 4.
- MACVICAR, B. A. & NEWMAN, E. A. 2015. Astrocyte regulation of blood flow in the brain. *Cold Spring Harb Perspect Biol*, 7.
- MADER, S. & BRIMBERG, L. 2019. Aquaporin-4 Water Channel in the Brain and Its Implication for Health and Disease. *Cells*, 8.
- MASDEU, J. C., DALMAU, J. & BERMAN, K. F. 2016. NMDA Receptor Internalization by Autoantibodies: A Reversible Mechanism Underlying Psychosis? *Trends Neurosci*, 39, 300-310.
- MILLER, B. J., HERZIG, K. H., JOKELAINEN, J., KARHU, T., KEINANEN-KIUKAANNIEMI, S., JARVELIN, M. R., VEIJOLA, J., VIINAMAKI, H., PAIVIKKI, T., JAASKELAINEN, E., ISOHANNI, M. & TIMONEN, M. 2021. Inflammation, hippocampal volume, and cognition in schizophrenia: results from the Northern Finland Birth Cohort 1966. *Eur Arch Psychiatry Clin Neurosci*, 271, 609-622.
- MILLER, J.-E. K., AYZENSHTAT, I., CARRILLO-REID, L. & YUSTE, R. 2014. Visual stimuli recruit intrinsically generated cortical ensembles. *Proceedings of the National Academy of Sciences*, 111, E4053-E4061.
- MOLLINEDO-GAJATE, I., SONG, C. & KNÖPFEL, T. 2019. Genetically Encoded Fluorescent Calcium and Voltage Indicators. *Handb Exp Pharmacol*, 260, 209-229.
- MORRIS, G. P. 2021. Visualizing antibody production in a human lymph node in a dish. *Science Translational Medicine*, 13, eabg5638.
- MULDOON, L. L., ALVAREZ, J. I., BEGLEY, D. J., BOADO, R. J., DEL ZOPPO, G. J., DOOLITTLE, N. D., ENGELHARDT, B., HALLENBECK, J. M., LONSER, R. R., OHLFEST, J. R., PRAT, A.,

- SCARPA, M., SMEYNE, R. J., DREWES, L. R. & NEUWELT, E. A. 2013. Immunologic privilege in the central nervous system and the blood-brain barrier. *J Cereb Blood Flow Metab*, 33, 13-21.
- MULLER, N. 2018. Inflammation in Schizophrenia: Pathogenetic Aspects and Therapeutic Considerations. *Schizophr Bull*, 44, 973-982.
- NIELL, C. M. & STRYKER, M. P. 2008. Highly Selective Receptive Fields in Mouse Visual Cortex. *The Journal of Neuroscience*, 28, 7520-7536.
- NIETZ, A. K., POPA, L. S., STRENG, M. L., CARTER, R. E., KODANDARAMAIAH, S. B. & EBNER, T. J. 2022. Wide-Field Calcium Imaging of Neuronal Network Dynamics In Vivo. *Biology*, 11, 1601.
- NIKOLAUS, M., RAUSCH, P., ROSTÁSY, K., BERTOLINI, A., WICKSTRÖM, R., JOHANNSEN, J., DENECKE, J., BREU, M., SCHIMMEL, M., DIEPOLD, K., HAEUSLER, M., QUADE, A., BERGER, A., ROSEWICH, H., STEEN, C., VON AU, K., DREESMANN, M., FINKE, C., BARTELS, F., KAINDL, A. M., SCHUELKE, M. & KNIERIM, E. 2023. Retrospective Pediatric Cohort Study Validates NEOS Score and Demonstrates Applicability in Children With Anti-NMDAR Encephalitis. *Neurol Neuroimmunol Neuroinflamm*, 10.
- NOMURA, T. 2021. Interneuron Dysfunction and Inhibitory Deficits in Autism and Fragile X Syndrome. *Cells*, 10.
- OH, J., LEE, C. & KAANG, B. K. 2019. Imaging and analysis of genetically encoded calcium indicators linking neural circuits and behaviors. *Korean J Physiol Pharmacol*, 23, 237-249.
- OKAMOTO, S., TAKAKI, M., HINOTSU, K., KAWAI, H., SAKAMOTO, S., OKAHISA, Y., TAKAO, S., TSUTSUI, K., KANBAYASHI, T., TANAKA, K. & YAMADA, N. 2022. Impairment of early neuronal maturation in anti-NMDA-receptor encephalitis. *Psychopharmacology (Berl)*, 239, 525-531.
- PACHITARIU, M., STRINGER, C., DIPOPPA, M., SCHRÖDER, S., ROSSI, L. F., DALGLEISH, H., CARANDINI, M. & HARRIS, K. D. 2017. Suite2p: beyond 10,000 neurons with standard two-photon microscopy. *bioRxiv*, 061507.
- PALMEIRA, P., QUINELLO, C., SILVEIRA-LESSA, A. L., ZAGO, C. A. & CARNEIRO-SAMPAIO, M. 2012. IgG placental transfer in healthy and pathological pregnancies. *Clin Dev Immunol*, 2012, 985646.
- PAREDES, R. M., ETZLER, J. C., WATTS, L. T., ZHENG, W. & LECHLEITER, J. D. 2008. Chemical calcium indicators. *Methods*, 46, 143-51.
- PATTADKAL, J. J., MATO, G., VAN VREESWIJK, C., PRIEBE, N. J. & HANSEL, D. 2018. Emergent Orientation Selectivity from Random Networks in Mouse Visual Cortex. *Cell Reports*, 24, 2042-2050.e6.
- PETERSEN, C. C. & CROCHET, S. 2013. Synaptic computation and sensory processing in neocortical layer 2/3. *Neuron*, 78, 28-48.
- PIASINI, E., SOLTUZU, L., MURATORE, P., CARAMELLINO, R., VINKEN, K., OP DE BEECK, H., BALASUBRAMANIAN, V. & ZOCCOLAN, D. 2021. Temporal stability of stimulus representation increases along rodent visual cortical hierarchies. *Nature Communications*, 12, 4448.
- PIERZYNOWSKA, K., WOLIŃSKI, J., WESTRÖM, B. & PIERZYNOWSKI, S. G. 2020. Maternal Immunoglobulins in Infants—Are They More Than Just a Form of Passive Immunity? *Frontiers in Immunology*, 11.
- PLATT, M. P., AGALLIU, D. & CUTFORTH, T. 2017. Hello from the Other Side: How Autoantibodies Circumvent the Blood–Brain Barrier in Autoimmune Encephalitis. *Frontiers in Immunology*, 8.

- PRIEBE, N. J. 2016. Mechanisms of Orientation Selectivity in the Primary Visual Cortex. *Annual Review of Vision Science*, 2, 85-107.
- PRÜSS, H. 2021. Autoantibodies in neurological disease. *Nature Reviews Immunology*, 21, 798-813.
- RASBAND, W. S. 1997-2023. *ImageJ* [Online]. U. S. National Institutes of Health, Bethesda, Maryland, USA. Available: <https://imagej.nih.gov/ij/> [Accessed 2023].
- REN, C. & KOMIYAMA, T. 2021. Wide-field calcium imaging of cortex-wide activity in awake, head-fixed mice. *STAR Protocols*, 2, 100973.
- RINGACH, D. L., SHAPLEY, R. M. & HAWKEN, M. J. 2002. Orientation Selectivity in Macaque V1: Diversity and Laminar Dependence. *The Journal of Neuroscience*, 22, 5639-5651.
- ROBBINS, M., CHRISTENSEN, C. N., KAMINSKI, C. F. & ZLATIC, M. 2021. Calcium imaging analysis - how far have we come? *F1000Res*, 10, 258.
- ROCHFERT, N. L., GARASCHUK, O., MILOS, R.-I., NARUSHIMA, M., MARANDI, N., PICHLER, B., KOVALCHUK, Y. & KONNERTH, A. 2009. Sparsification of neuronal activity in the visual cortex at eye-opening. *Proceedings of the National Academy of Sciences*, 106, 15049-15054.
- ROSALES JUBAL, E., SCHWALM, M., DOS SANTOS GUILHERME, M., SCHUCK, F., REINHARDT, S., TOSE, A., BARGER, Z., ROESLER, M. K., RUFFINI, N., WIERCZEIKO, A., SCHMEISSER, M. J., SCHMITT, U., ENDRES, K. & STROH, A. 2021. Acitretin reverses early functional network degradation in a mouse model of familial Alzheimer's disease. *Sci Rep*, 11, 6649.
- RUSSELL, J. T. 2011. Imaging calcium signals in vivo: a powerful tool in physiology and pharmacology. *Br J Pharmacol*, 163, 1605-25.
- SALUSSOLIA, C. L., PRODROMOU, M. L., BORKER, P. & WOLLMUTH, L. P. 2011. Arrangement of subunits in functional NMDA receptors. *J Neurosci*, 31, 11295-304.
- SCHOLL, B., TAN, A. Y. Y., COREY, J. & PRIEBE, N. J. 2013. Emergence of Orientation Selectivity in the Mammalian Visual Pathway. *The Journal of Neuroscience*, 33, 10616-10624.
- SHAPLEY, R., HAWKEN, M. & RINGACH, D. L. 2003. Dynamics of Orientation Selectivity in the Primary Visual Cortex and the Importance of Cortical Inhibition. *Neuron*, 38, 689-699.
- SHEN, J. X. & YAKEL, J. L. 2009. Nicotinic acetylcholine receptor-mediated calcium signaling in the nervous system. *Acta Pharmacol Sin*, 30, 673-80.
- SINGER, W. 2009. The Brain, a Complex Self-organizing System. *European Review*, 17, 321-329.
- SITÀ, L., BRONDI, M., LAGOMARSINO DE LEON ROIG, P., CURRELI, S., PANNIELLO, M., VECCHIA, D. & FELLIN, T. 2022. A deep-learning approach for online cell identification and trace extraction in functional two-photon calcium imaging. *Nature Communications*, 13, 1529.
- SLIFKA, M. K., MATLOUBIAN, M. & AHMED, R. 1995. Bone marrow is a major site of long-term antibody production after acute viral infection. *J Virol*, 69, 1895-902.
- SOLTANIAN-ZADEH, S., SAHINGUR, K., BLAU, S., GONG, Y. & FARSIU, S. 2019. Fast and robust active neuron segmentation in two-photon calcium imaging using spatiotemporal deep learning. *Proceedings of the National Academy of Sciences*, 116, 8554-8563.
- SOMAROWTHU, A., GOFF, K. M. & GOLDBERG, E. M. 2021. Two-photon calcium imaging of seizures in awake, head-fixed mice. *Cell Calcium*, 96, 102380.
- SOSULINA, L., MITTAG, M., GEIS, H.-R., HOFFMANN, K., KLYUBIN, I., QI, Y., STEFFEN, J., FRIEDRICH, D., HENNEBERG, N., FUHRMANN, F., JUSTUS, D., KEPPLER, K., CUELLO, A. C., ROWAN, M. J., FUHRMANN, M. & REMY, S. 2021. Hippocampal hyperactivity in a rat model of Alzheimer's disease. *Journal of Neurochemistry*, 157, 2128-2144.

- STEELE, T. R., GERSTENBERGER, D. C., DROBSHOFF, A. & WALLACE, R. W. 1991. Broadly tunable high-power operation of an all-solid-state titanium-doped sapphire laser system. *Opt Lett*, 16, 399-401.
- STEINMETZ, N. A., ZATKA-HAAS, P., CARANDINI, M. & HARRIS, K. D. 2019. Distributed coding of choice, action and engagement across the mouse brain. *Nature*, 576, 266-273.
- STERZER, P., ADAMS, R. A., FLETCHER, P., FRITH, C., LAWRIE, S. M., MUCKLI, L., PETROVIC, P., UHLHAAS, P., VOSS, M. & CORLETT, P. R. 2018. The Predictive Coding Account of Psychosis. *Biol Psychiatry*, 84, 634-643.
- STEUJLET, P., CABUNGAL, J. H., MONIN, A., DWIR, D., O'DONNELL, P., CUENOD, M. & DO, K. Q. 2016. Redox dysregulation, neuroinflammation, and NMDA receptor hypofunction: A "central hub" in schizophrenia pathophysiology? *Schizophrenia Research*, 176, 41-51.
- STRINGER, C. & PACHITARIU, M. 2019. Computational processing of neural recordings from calcium imaging data. *Current Opinion in Neurobiology*, 55, 22-31.
- STRINGER, C., PACHITARIU, M., STEINMETZ, N., REDDY, C. B., CARANDINI, M. & HARRIS, K. D. 2019. Spontaneous behaviors drive multidimensional, brainwide activity. *Science*, 364, eaav7893.
- TEIXEIRA, A. L., ROCHA, N. P. & ZHANG, X. 2017. Anti-NMDAR antibodies as a new piece in schizophrenia's puzzle. *Future Sci OA*, 3, Fso178.
- TEMPIO, A., BOULKSIBAT, A., BARDONI, B. & DELHAYE, S. 2023. Fragile X Syndrome as an interneuronopathy: a lesson for future studies and treatments. *Frontiers in Neuroscience*, 17.
- TIAN, G. F., AZMI, H., TAKANO, T., XU, Q., PENG, W., LIN, J., OBERHEIM, N., LOU, N., WANG, X., ZIELKE, H. R., KANG, J. & NEDERGAARD, M. 2005. An astrocytic basis of epilepsy. *Nat Med*, 11, 973-81.
- TITULAER, M. J., MCCRACKEN, L., GABILONDO, I., ARMANGUÉ, T., GLASER, C., IIZUKA, T., HONIG, L. S., BENSELER, S. M., KAWACHI, I., MARTINEZ-HERNANDEZ, E., AGUILAR, E., GRESA-ARRIBAS, N., RYAN-FLORANCE, N., TORRENTS, A., SAIZ, A., ROSENFELD, M. R., BALICE-GORDON, R., GRAUS, F. & DALMAU, J. 2013. Treatment and prognostic factors for long-term outcome in patients with anti-NMDA receptor encephalitis: an observational cohort study. *The Lancet Neurology*, 12, 157-165.
- TREPEL, M., URBAN & FISCHER, V. 2015. *Neuroanatomie Struktur und Funktion*, München, Elsevier, Urban & Fischer München.
- VARATHARASAN, V., SHIN, H. S., TSOURDOS, A. & COLOSIMO, N. Improving Learning Effectiveness For Object Detection and Classification in Cluttered Backgrounds. 2019 Workshop on Research, Education and Development of Unmanned Aerial Systems (RED UAS), 25-27 Nov. 2019 2019. 78-85.
- WANG, R. & REDDY, P. H. 2017. Role of Glutamate and NMDA Receptors in Alzheimer's Disease. *J Alzheimers Dis*, 57, 1041-1048.
- WEI, L., XUE, Z., LAN, B., YUAN, S., LI, Y., GUO, C., ZHANG, R., DING, R. & SHEN, H. 2021. Arctigenin Exerts Neuroprotective Effect by Ameliorating Cortical Activities in Experimental Autoimmune Encephalomyelitis In Vivo. *Front Immunol*, 12, 691590.
- WEI, Z., LIN, B.-J., CHEN, T.-W., DAIE, K., SVOBODA, K. & DRUCKMANN, S. 2020. A comparison of neuronal population dynamics measured with calcium imaging and electrophysiology. *PLOS Computational Biology*, 16, e1008198.
- XU, X., CANG, J. & RIECKE, H. 2020a. Development and binocular matching of orientation selectivity in visual cortex: a computational model. *Journal of Neurophysiology*, 123, 1305-1319.

- XU, X., LU, Q., HUANG, Y., FAN, S., ZHOU, L., YUAN, J., YANG, X., REN, H., SUN, D., DAI, Y., ZHU, H., JIANG, Y., ZHU, Y., PENG, B., CUI, L. & GUAN, H. 2020b. Anti-NMDAR encephalitis. *A single-center, longitudinal study in China*, 7, e633.
- XU, Z., WU, Y., GUAN, J., LIANG, S., PAN, J., WANG, M., HU, Q., JIA, H., CHEN, X. & LIAO, X. 2023. NeuroSeg-II: A deep learning approach for generalized neuron segmentation in two-photon Ca²⁺ imaging. *Frontiers in Cellular Neuroscience*, 17.
- YAMAMOTO, H., HAGINO, Y., KASAI, S. & IKEDA, K. 2015. Specific Roles of NMDA Receptor Subunits in Mental Disorders. *Curr Mol Med*, 15, 193-205.
- ZATKA-HAAS, P., STEINMETZ, N. A., CARANDINI, M. & HARRIS, K. D. 2021. Sensory coding and the causal impact of mouse cortex in a visual decision. *Elife*, 10.
- ZHANG, Y., RÓZSA, M., LIANG, Y., BUSHEY, D., WEI, Z., ZHENG, J., REEP, D., BROUSSARD, G. J., TSANG, A., TSEGAYE, G., NARAYAN, S., OBARA, C. J., LIM, J. X., PATEL, R., ZHANG, R., AHRENS, M. B., TURNER, G. C., WANG, S. S., KORFF, W. L., SCHREITER, E. R., SVOBODA, K., HASSEMAN, J. P., KOLB, I. & LOOGER, L. L. 2023. Fast and sensitive GCaMP calcium indicators for imaging neural populations. *Nature*, 615, 884-891.
- ZHENG, J. 2013. Molecular mechanism of TRP channels. *Compr Physiol*, 3, 221-42.
- ZHOU, S. & YU, Y. 2018. Synaptic E-I Balance Underlies Efficient Neural Coding. *Frontiers in Neuroscience*, 12.
- ZHOU, X., HOLLERN, D., LIAO, J., ANDRECHEK, E. & WANG, H. 2013. NMDA receptor-mediated excitotoxicity depends on the coactivation of synaptic and extrasynaptic receptors. *Cell Death Dis*, 4, e560.
- ZHOU, Y. & GAO, J. 2022. Why not try to predict autism spectrum disorder with crucial biomarkers in cuproptosis signaling pathway? *Front Psychiatry*, 13, 1037503.

9. Acknowledgments

First of all, I would like to express my heartfelt gratitude to [REDACTED], for his guidance, mentorship, and expertise. His insightful feedback and encouragement shaped the direction of this research, making my thesis possible.

I would like to extend my gratitude to [REDACTED] for his oversight and support during my research. His clinical expertise was instrumental for this work.

Special thanks go to everyone who helped the development of this work. Especially to:

- [REDACTED] for initially planning this project and performing a part of the experiments for the antibody exposed group.
- [REDACTED] and [REDACTED] for their supervision of my initial animal surgeries and helpful feedback.
- [REDACTED] for introducing me to the world of calcium imaging analysis and help troubleshooting imaging issues.
- [REDACTED] for her help in establishing the experimental plan.
- [REDACTED], and [REDACTED], for their various contributions towards the development of ViNe-Seg.

I heartfully thank all the members of the [REDACTED] Lab, namely [REDACTED] and [REDACTED]. Their support and insightful feedback helped improve the quality of this work. Without the professional and scientific work environment they created, this work would have not been possible.

I would like to express my gratitude to the Saudi Ministry of Education and the King Abdullah Scholarship Program for the generous support that allowed me to pursue my education abroad.

Last but not the least, I would like to thank my parents, [REDACTED] and [REDACTED] my two sisters, [REDACTED] and [REDACTED] and my wife, [REDACTED]. Your support and encouragements have helped me throughout my education. Without you, I would never be where I am today.

10. Publications

Published:

Altahini, S., Arnoux, I. & Stroh, A. "Optogenetics 2.0: challenges and solutions towards a quantitative probing of neural circuits" *Biological Chemistry*, 2023.
<https://doi.org/10.1515/hsz-2023-0194>

In preparation:

Altahini, S., Doering, J., Kuchling, J., Backhaus, H., Kreye, J., Guimaraes-Backhaus, R., Finke, C., Prüss H. & Stroh A. " Maternofetal transfer of human NMDAR antibodies leads to cortical network defect in the adult"

Ruffini, N., Altahini, S., Weißbach, S., Weber, N., Milkowits, J., Wierczeiko, A., Backhaus, H. & Stroh A. "ViNe-Seg: Deep-Learning assisted Segmentation of Visible Neurons and subsequent Analysis embedded in a Graphical User Interface"

Backhaus, H., Altahini, S., Wierczeiko, A., Ruffini, N. & Stroh A. " Resilient networks: Social stress-resilience is reflected in an increased performance of visual cortical circuits"

Poster presentations:

International Winter Neuroscience Conference. 11th - 15th April 2023. Sölden, Austria.
"Apparent microcircuit recruitment dynamics in the mouse model of Anti-NMDA Receptor encephalitis indicate a disassociation between spontaneous and visually evoked activity" Altahini, S., Doering, J., Backhaus, H. & Stroh A.

11. Curriculum vitae

